UNIVERSITÀ
DEGLI STUDI
DI BRESCIA

DOTTORATO DI RICERCA IN INGEGNERIA CIVILE, AMBIENTALE, DELLA COOPERAZIONE INTERNAZIONALE E DI MATEMATICA

Curriculum: Analisi e gestione dei rischi naturali

Settore Scientifico Disciplinare: ICAR/01 Idraulica

CICLO

XXXVI

AN ENHANCED MODELLING APPROACH FOR DEBRIS FLOW INCEPTION AND PROPAGATION

Tesi di dottorato di:

BONOMELLI RICCARDO

Relatore:

Chiar.mo Prof. MARCO PILOTTI

Abstract

Debris flows are a fundamental component of hydraulic hazard in mountain areas and are often triggered by the failure of the saturated bed along the channel network. Accordingly, the identification of unstable areas during a rainfall event inside a catchment and the debris flow propagation are crucial to the correct computation of hydraulic hazard in mountain areas. Focusing the attention on the collapse of lateral slopes, in literature many contributions deal with the first task by using physically based distributed models. In most applications the geotechnical component of these models provides the Factor of Safety (FS) using the Infinite Slope (IS) assumption coupled with suitable hydrological hypothesis. However, there is evidence in literature, that the IS assumption, that considers single cells stability, becomes increasingly inadequate with the growing space resolution of the elevation model, contributing to the overprediction of unstable areas that affect these models. As a first contribution, in this thesis an original improvement to the stability calculation is proposed for physically based distributed models. The improvement is obtained by presenting a modification of the Janbu's method of slices suitable to basin scale applications. It is shown that the proposed method is systematically better than the local IS prediction for a set of elementary test cases in which a rigorous stability analysis is available, confirming the predictive capabilities of the proposed approach. Finally, the applicability of the method at the watershed scale is showed by considering its application to a well-known test case in Oregon, i.e. the Mettman Ridge. As a second contribution, once the source areas have been detected, in order to model the propagation of triggered debris flows, a numerical solver has been implemented. The proposed software, called DEBRA (Debris-flow Evolution and Behaviour for Risk Assessment), is a shock capturing finite volume numerical scheme which solves the monophasic 2D Steep Slope Shallow Water Equations on an unstructured grid. DEBRA can use multiple rheological laws (Manning's for newtonian fluids, Voellmy's and O'Brien's for non-newtonian fluids) used in most commercial software allowing the user to choose the best formulation according to experience or field characteristics. Firstly, the numerical scheme is validated against dam break analytical solutions which are obtained specifically for each rheology. Finally, DEBRA and a commercially available software (RAMMS) are compared on a recent event happened in Niardo (Italy) where information about deposition maps and inundation extent are available.

Keywords: Debris flow, Numerical modelling, Slope stability, Shallow Water Equations.

Abstract

Le colate detritiche sono una componente fondamentale della pericolosità idraulica nelle aree montane e sono spesso innescate dal cedimento del fondo alveo saturo lungo il reticolo canalizzato. Di conseguenza, l'identificazione delle aree instabili durante un evento meteorico intenso a scala di bacino è cruciale per la mappatura delle aree potenzialmente impattate. Relativamente ai collassi di versante, in letteratura molti contributi utilizzano dei modelli fisicamente basati a scala di bacino per modellare il fenomeno. Nella maggior parte delle applicazioni la componente geotecnica di questi modelli fornisce il Fattore di Sicurezza (FS) utilizzando il modello di versante infinito (IS) accoppiato con opportune ipotesi idrologiche. Tuttavia, è possibile riscontrare in letteratura che il modello IS, il quale considera ogni cella del bacino in modo isolato, diviene via via meno adeguato all'aumentare della risoluzione del modello di elevazione del bacino, contribuendo a sovrastimare le aree instabili. In questo lavoro verrà presentato un originale miglioramento del calcolo della stabilità dei versanti, modificando il metodo di stabilità di Janbu per poter essere applicato a scala di bacino. Il metodo proposto è un miglioramento rispetto all'IS su casi test semplificati in cui un'analisi di stabilità rigorosa consente di validare le risposte dei modelli. Infine, è stato applicato il modello introdotto ad un caso test ben documentato in letteratura: il Mettman Ridge in Oregon. Nell'ottica di modellare la propagazione delle colate detritiche dopo l'innesco è stato implementato un codice numerico ai volumi finiti chiamato DEBRA (Debris-flow Evolution and Behaviour for Risk Assessment) in grado di simulare la propagazione degli shock grazie alla risoluzione delle equazioni delle acque basse bidimensionali a forte pendenza su grigliati non-strutturati. DEBRA è dotato di svariati modelli reologici (Manning per fluidi newtoniani, Voellmy e O'Brien per fluidi non newtoniani) utilizzati in letteratura e in altri software commerciali, consentendo all'utente di poter selezionare la formulazione migliore considerando le peculiarità del caso in esame. In primo luogo, lo schema numerico è stato validato utilizzando soluzioni analitiche di rottura di diga o presenti in letteratura o derivate appositamente per la reologia considerata. In secondo luogo, sono stati confrontati i risultati di DEBRA e di un software commerciale (RAMMS) relativamente alla propagazione di una colata accaduta recentemente a Niardo (Italia) dove sono disponibili informazioni di riferimento relative alla deposizione e all'estensione delle aree impattate.

A Monica,

il tuo sorriso…

il miglior caffè che esista.

Acknowledgements

A PhD thesis is truly never the work of a single mind. It is the summary of the three years of studying, attending congresses, making progresses, making mistakes and finally achieving some results, all of which cannot be done alone. I must thank first of all my supervisor, Prof. Marco Pilotti, for his passion and dedication to the topic, which guided me especially in the early stages of this work. A special thanks goes to my colleague Gabriele Farina for the constant exchange of ideas and for sharing the experience of being a PhD student with me. A sincere thank you to the whole hydraulics group of the University of Brescia for the opportunity to engage in different activities which enlarged my view on topics not strictly related to my research but equally interesting. Finally a warm thank you to my family and friends for encouraging and sustaining my choices and my studies over all these years. This work is also for you.

Contents

Introduction

In recent years, the escalating frequency of extreme rainfall events has underlined the urgent need for effective disaster mitigation strategies. In mountain areas, debris flows triggered by prolonged or intense rainfall events pose a significant threat to inhabited and vulnerable regions, stressing the need for development of Early Warning Systems (EWS) to safeguard lives and infrastructure. In general terms, as reported by Piciullo et al. (2018), an Early Warning System is an important dynamic and non-structural mitigation alternative, upgradable over time to reduce the risk for human life associated to the occurrence of hazardous events. EWSs can be defined as the set of capacities needed to generate and disseminate timely and meaningful warning information to enable individuals, communities and organizations threatened by a hazard to prepare and to act appropriately and in sufficient time to reduce the possibility of harm or loss (UNISDR, 2009). People-oriented EWSs are made by a few interconnected assets (UNISDR, 2006): 1) identification of risks; 2) monitoring, analysis and forecasting of hazards; 3) communication of warnings and 4) local responses to warnings. The identification of risk follows the study of hazards in a given area. Considering an inhabited area near a mountain catchment, the recognition of risk means to quantify the possible consequences of a debris flow that could occur in an area where valuable assets are present. The occurrence of a debris flow can be suggested either from the characteristics of the catchment or from historical events. Accordingly, although the analysis of historical events is the first step to an adequate knowledge of the risk, it is often not sufficient, either due to lack of documentation or due to climate change which is responsible for a higher frequency and intensity of rainfalls, thus endangering previously unaffected or inhabited areas. On the other hand monitoring requires gauging stations which can record some physical quantity of interest, i.e. rainfall or overall debris discharge, a fundamental data set for calibration purposes of any analysis and forecasting of hazards. However, a simple gauging station can provide information about the history of a particular catchment but provide little information for forecasting purposes. This is true especially if the data collected is not analysed by some kind of model which can extrapolate what is going to happen based on past recordings. Considering debris flows, the forecasting aspect requires special attention, due to their high velocity, long runout and high impact forces (Berti et at., 2020). Intense or prolonged rainfall events are the main cause of debris flow triggering so most regional warning systems rely on the use of rainfall thresholds to predict their occurrence (Berti et al., 2020). However, these intensity duration curves are usually empirically derived from past observations in which a certain rainfall triggered a debris flow (Cannon et al., 2008). Accordingly, they provide a useful but very approximate indication of something that can happen somewhere and sometime in the catchment, without any indication of its magnitude or of the actually impacted areas. Furthermore, these thresholds, being purely regressive, do not consider the sediment availability in a catchment which may or may not be present to trigger a debris flow independently from the rainfall. A similar flaw can affect also more recent Machine Learning (ML) based models (Piciullo et al., 2022), which despite their applicability and their exponential growth in usage in new fields, require a large amount of diverse data to calibrate and to be considered useful. Most ML algorithms significantly “draw” from past experience, therefore struggle to predict new susceptible patterns (Tehrani et al., 2022). Following the contribution of Varnes (1984) most of ML literature contributions (Tehrani et al., 2022) use a pixel-based computational approach to evaluate susceptibility analysis, neglecting more complex failure mechanisms that may involve entire slopes. Furthermore, the low number of landslide cells in relation to non-landslide cells (Tehrani et al.,

2022) may significantly affect the quality of results. On the other hand, the reliability of an early warning system is fundamental to ensure its effectiveness and, in this direction, more reliable systems can be tension cables located in sensible portions of the catchment and equipped with a sensor which is triggered if the cable is suddenly put in tension. Despite their effectiveness, the time to issue a warning with this information is very limited, because it is proportional to the propagation time of the debris flow from the point where the cable is placed as far as the sensible areas. Depending on the characteristics of the catchment, this warning time can be as little as 10-20 minutes which can be effectively used to stop circulation along roads by triggering traffic lights but, on the other hand, is very short for more comprehensive civil protection measures if they need to be deployed. Therefore, there is an urgent need to identify methods which can be used to extend the warning time while keeping their reliability. This research is based on the idea that there is a positive answer to this problem and it must be searched in the physics behind the phenomena that triggers debris flows. In the author's opinion, by coupling these methods to the enhanced predictive capabilities of meteorological models and to suitable distributed hydrologic modeling of the rainfall-runoff transformation at the watershed scale, the warning time can be made significantly longer to the point that evacuation measures can be implemented. Examples of integrated modelling, i.e. models that combine triggering with propagation of debris flows, can be found in the literature. Stancanelli et al. (2017) coupled a well-known soil stability model, i.e. TRIGRS (Baum et al., 2008), to model soil stability and the hydrological response of a catchment to an incoming rainfall, while using the commercial software FLO-2D (FLO-2D software) to propagate the debris flow that originates from each unstable cell. However, the limited knowledge of the catchment soil properties required an iterative calibration procedure, which still required the introduction of a threshold to limit the number of potentially unstable areas computed by TRIGRS. Liu & He (2020) suggested a complex integrated modelling which showed promising results by successfully coupling the Richard's equation for soil saturation due to rainfall, Shallow Water Equations (SWE) for runoff along the drainage network and ultimately a biphasic approach capable of propagating the debris flow once the flow becomes hyperconcentrated. The focus of such modelling chain, as stated by the authors, are runoff generated debris flows which occur under heavy rainfall and loose deposits (Liu & He, 2020), which is not always the case in alpine areas, more prone to debris flows originated from shallow landslides. Being an exceedingly complex problem, in the following this research has been confined to the analysis of the stability of the slopes that are present in a catchment, proposing an innovative approach to study their response to growing water saturation during rainfall events. The idea of coupling a distributed hydrologic model to a local stability model is not new and has been practiced many times in the literature over the last 30 years. However, this has been done either by numerically solving the flow and stability conditions inside simplified and limited slopes by using the Finite Element methods, with strong limitations arising from the computational burden on the extension of the studied area, or by using the simple Infinite Slope (IS) approximation on a raster digital elevation model of the watershed, a method that totally neglects the collaborative role of surrounding blocks on the local stability. Although some critical papers have cast doubts on the scope of validity of this approach, it is still widely used and so far, in the author's knowledge, no reasonably simple method has been presented in the literature to overcome the mentioned limitations. Here it is proposed a modification of the well-known Janbu's method of slices (1973), widely used in geotechnical applications, in order to make it suitable to basin scale applications. It is showed that the proposed method is systematically better than the local

IS prediction for a set of elementary test cases in which a rigorous stability analysis is available, confirming the predictive capabilities of the proposed approach. Finally, it is showed the applicability of the method at the watershed scale by considering its application to a well-known test case in literature, i.e. the Mettman Ridge watershed in Oregon. Thanks to the introduced methodology, able to enhance the prediction of the areas more susceptible to failure during a rainfall event at catchment scale, it is possible to obtain a reasonable estimate about the volumes and the locations at which the saturated soil can start to propagate downstream. Using the assumption of a monophasic fluid, a SWE solver has been proposed and implemented to study the propagation phase. Even though the monophasic assumption does not incorporate the state of the art physics on the debris flow propagation, according to which the phenomena can be studied considering the solid and liquid phases separately, at this stage of research the potential of an enhanced 2D SWE solver was investigated. State of the art physics include multiphase flow (Trujillo-Vela et al., 2022), able to describe the solid and the liquid phase separately, which allows the simulation of flows in which the solids concentration, i.e. sediments, may vary in time, thus enabling a more accurate representation of the phenomena. Physics complexity scales accordingly with mathematical complexity which often lead either to multiple parameters to calibrate before the simulation or additional numerical challenges like the loss of hyperbolicity of the system of equations being solved, tied to the appearance of Kelvin-Helmholtz instabilities (Pelanti et al., 2008) which arise when the two phases tend to separate. Having in mind the need of a practical and operative tool to properly account for all the uncertainties of the phenomena, the following important improvements are introduced: 1) the use of an unstructured grid that allows a better reproduction of the local bathymetry; 2) the adoption of a state-of-the-art steep formulation of the solving equations, that seems important considering the nature of the problem; 3) the use of two constitutive equations (in addition to the plain newtonian rheology) currently implemented in two separate solvers (FLO-2D and RAMMS) that are the most internationally widely used for the practical mapping of debris flow hazard. Finally, the implementation of transparent and physically based conditions for the input sedimentograph, that unfortunately are not clearly implemented in the mentioned software. Eventually, a shock capturing finite volume numerical scheme with the mentioned features has been implemented, called DEBRA (Debris-flow Evolution and Behaviour for Risk Assessment). In the following, the numerical scheme is validated against dam break analytical solutions which are obtained specifically for each rheology considered. A brief discussion on each modelled rheology is reported, highlighting how the parameters affect the flow being modelled. Finally, DEBRA and a commercially available software (RAMMS) are compared on a real event happened in Niardo (Italy) where information about deposition maps and inundation extent occurred in a recent event are available.

References

Baum, R. L., Savage W. Z., Godt. J. W. (2008). TRIGRS – a Fortran program for transient rainfall infiltration and grid-based regional slope-stability analysis, version 2.0, USGS.

Berti, M., Gregoretti, C. Simoni, A. (2020). Physical interpretation of rainfall thresholds for runoff-generated debris flows. Journal of Geophysical Research: Earth Surface, 125, 10.1029/2019JF005513.

Cannon, S. H., Gartner, J. E., Wilson, R. C., Bowers, J. C., Laberd, J. L. (2008). Storm rainfall conditions for floods and debris flows from recently burned areas in southwestern Colorado and southern California. Geomorphology, 96, 250-269.

FLO-2D Software: Hydrologic and Hydraulic Modeling Software. FLO2D Software. http://www.flo-2d.com/

Janbu, N. (1973). Slope stability computations, Embankment Dam Engineering, Casagrande Volume, R.C. Hirschfeld and S.J. Poulos, eds., John Wiley and Sons, New York, pp 47-86.

Liu, W., He, S. (2020). Comprehensive modelling of runoff-generated debris flow from formation to propagation in a catchment. Landslides, 17: 1529-1544, 10.1007/s10346-020-01383-w

Piciullo, L., Calvello, M., Cepeda, J. M. (2018). Territorial early warning systems for rainfall-induced landslides. Earth-Science Reviews, 179, 228-247, 10.1016/j.earscirev.2018.02.013.

Pelanti, M., Bouchut, F., Mangeney, A. (2008). A Roe-type scheme for two phase shallow granular flows over variables topography. ESAIM Mathematical Modelling and Numerical Analysis, 42, 851-885, 10.1051/m2an:2008029.

Piciullo, L., Capobianco, V., Heyerdahl, H. (2022). A first step towards a IoT-based local early warning system for an unsaturated slope in Norway. Natural Hazards, 114:3377-3407, 10.1007/s11069-022-05524-3.

Stancanelli, L. M., Peres, D. J., Cancelliere, A., Foti, E. (2017). A combined triggering-propagation modeling approach for the assessment of rainfall induced debris flow susceptibility. Journal of Hydrology, 550, j.jhydrol.2017.04.038.

Tehrani, F. S., Calvello, M., Liu, Z., Zhang, L., Lacasse, S. (2022). Machine learning and landslide studies: recent advances and applications. Natural Hazards, 114:1197-1245, 10.1007/s11069-022-05423-7.

Trujillo-Vela, M. G., Ramos-Cañon, A. M., Escobar-Vargas, A. E., Galindo-Torres, S. A. (2022). An overview of debris-flow mathematical modelling, Earth-Science Reviews, 232, 104135, 10.1016/j.earscirev.2022.104135.

United Nations Inter-Agency Secretariat of the International Strategy for Disaster Reduction (UNISDR). (2006). Global survey of early warning systems: an assessment of capacities, gaps and opportunities towards building a comprehensive global early warning system for all natural hazards.

United Nations International Strategy for Disaster Risk Reduction (UNISDR). (2009). Terminology on disaster risk reduction. Geneva Switzerland.

Varnes, D. J. (1984). Landslide Hazard zonation: a review of principles and practice, IAEG Commission on Landslides and other Mass-Movements, The UNESCO Press, Paris,p. 63.

Chapter 1

A novel approach for the computation of soil slope stability in distributed hydrologic applications

1.1 Introduction

Debris flows are a major component of hydraulic hazard in mountainous environment and are often triggered by the collapse of steep slopes along the drainage network of a watershed. Soil slope failures are usually triggered by a build-up of pore water pressure during heavy or prolonged rainfalls undermining the equilibrium between resistance and gravitational forces (Iverson, 2000). Accordingly, the accurate prediction of the locations of the areas which are most susceptible to failure, as well as of the amount of material that is destabilized have great importance for zonation purposes and for designing early-warning systems (e.g. Piciullo et al., 2018; Guzzetti et al., 2020). The interplay between groundwater, water runoff and geotechnical soil properties determines where a soil slope failure will occur: accordingly, hillslope hydrology plays a crucial role in the overall process. To this purpose distributed physically based hydrological models, operating either in steady state or in dynamic conditions (e.g. Dietrich et al., 1992; Dietrich et al., 1993; Dietrich et al., 1995; Baum et al., 2008; Casadei et al., 2003; Iida, 2004), coupled with a soil stability model triggered either by shallow subsurface flow (e.g. Montgomery & Dietrich, 1994; Dietrich et al., 2001) or by a wetting front during rainfall event (e.g. Rosso et al., 2006), have been used to map landslide sources in a watershed. The overall idea is important and attractive: a distributed hydrologic model that provides the surface and shallow subsurface flow paths, derived by the terrain gradient, showing the locations where pore water pressure builds up and where runoff is stronger. The first element governs instability whereas the second is a key variable in the potential evolution of a soil slip into fast slope movements, e.g. debris flow. As a consequence, several physically based models at the basin scale have been proposed, based either on actual rainfall-runoff models (e.g. Baum et al., 2008) or on more simplified GIS coupling between land topography and rainfall potential (e.g. Dolojan, 2021). It is interesting to observe that since the very first distributed hydrological attempt to model soil stability in a watershed (e.g. Haefeli, 1948), the Infinite Slope approach (IS in the following) has been mainly used (Rossi et al., 2013; Medina et al., 2021; Murgia et al., 2022). In their seminal contribution Montgomery & Dietrich (1994) developed a distributed model able to combine digital elevation data with near surface throughflow under steady rainfall and IS stability models. Following a similar idea the Transient Rainfall Infiltration Grid-Based Regional Slope Stability (TRIGRS) model (Baum et al., 2008) computes slope stability considering the transient pore-pressure due to rainfall infiltration. The TRIGRS model is based on an extension of the linearized solution of the Richards' equation (Iverson, 2000), while the IS hypothesis is adopted for slope stability computation. The Shallow Landslides Instability Prediction (SLIP) model (Montrasio et al., 2011) considers the stability conditions of a slope, the soil characteristics, and the incoming rainfall, by neglecting the surface run-off and transient infiltration, since the entire amount of rain at a certain time instantaneously infiltrates into the soil. Cho & Lee (2002) and Cho (2017) proposed a similar model which uses the Green & Ampt equations (1911) for rainfall infiltration and the IS hypothesis for slope stability. Multidimensional stability models at the watershed scale are an active topic of research (e.g. Hovland, 1977; Burroughs, 1985; Dietrich et al., 2008). Such models usually apply a limit-equilibrium approach to an assumed failure surface, modelling the soil as a collection of rigid

blocks. Even though these models require the same input parameters as IS models, they avoid the a-priori definition of a failure surface. Accordingly, their application is hindered by the need of an efficient search algorithm to test multiple failure shapes. Actually, the number of possible failure surfaces grows exponentially with the number of grid cells used, so this approach may soon become intractable as the number of cells becomes significant (Dietrich et al., 2008). For these reasons, some constraints must be introduced in order to reduce the computational complexity of the problem (Bellugi et al., 2015). Montgomery et al. (2000) used a predefined rectangular landslide shape with a fixed size, Gabet & Dunne (2002) and Casadei et al. (2003) assumed that the areas of instability have a fixed length to width ratio. Okimura (1994) assumed landslides to be rectangular but characterized by a single length to width ratio: the size of the landslide is determined by computing a least stable cell using an IS model then exploring a fixed number of potential rectangular slide masses that included the least stable cell. Qiu et al. (2017) and Oguz et al. (2022) instead, explored the three-dimensional stability of ellipsoidal surfaces, using the procedure described in the work of Hovland (1977), neglecting the resisting contribution provided by the roots on the margin of the unstable block. In order to reduce the computational complexity, Lehmann & Or (2012) proposed a different approach in which the shape of the landslide can be general but requires the landslides to originate at a single cell. In their contribution the hillslope is modelled as different soil columns interconnected by frictional and tensional mechanical bonds represented as fiber bundles. If a certain failure criterion measured on the forces acting at the base of the soil column is met, then its load gets redistributed to its neighbours via the beforementioned fibers, which can fail as well, allowing an accurate description of the failure mechanism. Despite the possibility to predict rather general failure shapes, this approach is computationally very intensive and tends to overpredict the number and volume of the observed landslides.

1.2 Evolution and limitations of physically based models

Over the last decades, in the coupled modeling of soil stability and transient hydrology at the watershed scale, one can observe considerable advances on the hydrological side and a tendency to use the IS model for the computation of stability. According to this approach, the stability is computed at a local scale, neglecting the interaction with the surrounding blocks. However, there is evidence that the confining role of the surrounding blocks can be dominant when the typical vertical scale of the soil depth, h, is comparable to the typical horizontal scale of the block, Δx. According to Griffiths et al. (2011), when the $\Delta x/h$ ratio is smaller than 16, the adequacy of the infinite slope assumption is questionable due to the boundary stresses that arise when the slope has a finite length compared to its depth. The practical relevance of this issue was negligible until a few decades ago, when the space resolution of the raster digital elevation models used in the hydrologic applications was relatively rough and a typical cell dimension was in the order of 10-20 m. At this scale, considering a reference soil depth typically less than 1 m (e.g. Lehmann & Or, 2016), the $\Delta x/h$ ratio was sufficiently large to make the infinite slope approach acceptable. On the other hand, after the widespread advent of LIDAR, it is now customary to have distributed hydrologic models with Δx in the order of a few meters. This is an important advancement (e.g. Claessens et al., 2005) because a better topographic resolution provides a careful reproduction of the flow paths, which is fundamental for the correct detection of flow accumulation zones and for the physical meaningfulness of the local parameters derived from the pre-processing of the drainage network (e.g. Pilotti et al., 1996) or from local soil properties. In these situations, the scope of validity of the IS assumption is narrowing, because collaborative actions between blocks can become dominant: an unstable block could be sustained by the surrounding ones, or a stable block can be destabilized due to the instability of the upper blocks along the hillslope. These situations are considered by

traditional geotechnical stability analysis that study the stability of the whole slope with methods of increasing complexity (e.g. by means of a Finite Element analysis or applying Morgenstern & Price procedure) that, however, are difficult to implement in dynamic hydrologic simulations. Another flaw of the IS model in catchment scale applications is a marked tendency to overprediction of unstable areas and, accordingly, of the potential landslide hazard (Bellugi et al., 2015). In this thesis it is proposed to overcome some limitations of the widespread IS method by implementing a modification of the well-known Janbu method (Janbu, 1973; US Army Corps of Engineers, 2003) as a reasonable compromise between the simplicity of the IS model and the complete limit equilibrium methods. As it will be showed, the Janbu method considers the collaborative action between consecutive cells along a hillslope and satisfies all equilibrium equations for the whole slope in its complete formulation (e.g. Spencer, 1967; Morgenstern & Price, 1965). The modified method is sufficiently simple and computationally unexpensive to be implemented within a distributed hydrological model. In the following, considering that watershed test cases are inevitably affected by large uncertainties on the actual distribution of governing soil parameters, the method was first applied to some idealized test cases where everything is known, using SLOPE/W module of the GeoStudio software (Stability modelling with GeoStudio, 2021) as a validation tool. Next, the performance of the proposed methodology with the predictions provided by the IS model was compared, showing a systematic improvement. Finally, the proposed methodology was validated in terms of landslide susceptibility at basin scale using a dataset provided by Bellugi et al. (2015) consisting of measured soil properties and of an inventory of unstable areas observed during a 10-year period in a catchment located in Oregon.

1.2.1 Infinite slope model

The most used criterion to assess the stability of a slope is the factor of safety (*FS* in the following), i.e. the ratio between stabilizing and destabilizing forces:

$$FS = \frac{F_{stable}}{F_{unstable}} \tag{1.1}$$

A slope characterised by $FS \geq 1$ is stable, indicating that it is able to withstand the stresses necessary to maintain equilibrium, while if $FS < 1$ the slope is unstable, and failure may occur if the stressing conditions persist. A standard method to compute the FS is the introduction of the infinite slope (IS) model. The IS model (Haefeli, 1948; Taylor, 1948; Skempton & DeLory, 1957) is based on the following assumptions:

- The slope is infinitely long
- Sliding failure occurs along a plane parallel to the surface of the slope

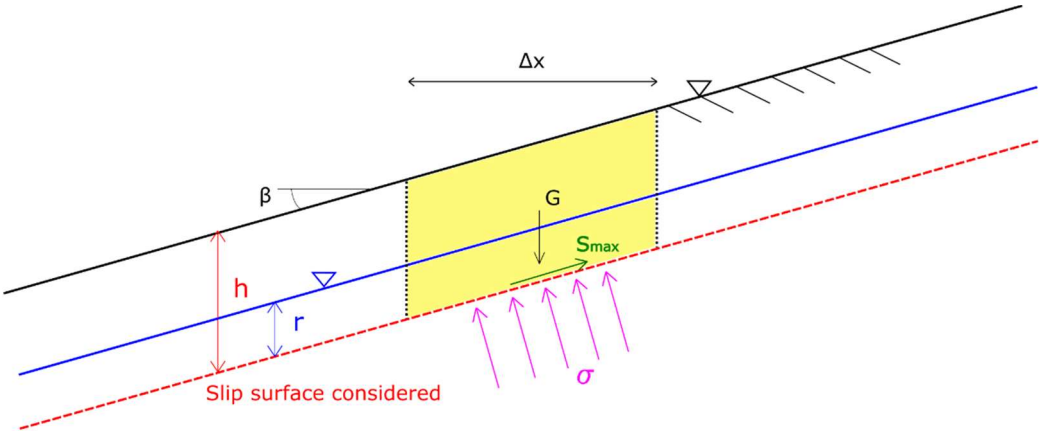

Figure 1.1 Side view of an infinitely wide and long slope inclined of an angle β.

In the IS simple equilibrium equations are derived considering a block (see the yellow-shaded area in Figure 1.1) where the slip surface is represented by the dashed line at depth h. The stabilizing force is given by S_{max} $[N]$, which is the maximum friction exerted along the slip surface at failure, provided by the Mohr-Coulomb relationship:

$$S_{max} = c'a + (\sigma - u)\, a \tan \phi' \tag{1.2}$$

where c' $[N/m^2]$ is the basal effective soil cohesion, $\phi'[°]$ is the effective friction angle, σ $[N/m^2]$ is the total stress perpendicular to the failure plane, u $[N/m^2]$ is the pore water pressure, a is the inclined bottom area of the element of soil considered given by $a = A/\cos\beta$, where A is the planimetric area of the element and β [°] is the inclination angle of the slope. In dry conditions, the vertically averaged specific weight of the soil γ_s $[N/m^3]$ is a function of the specific weight of the solid matrix, γ_m $[N/m^3]$, and of the block porosity, φ $[-]$ as $\gamma_d = (1-\varphi)\gamma_m$. When moisture is present inside the soil, the specific weight depends also on the degree of saturation. If the block is totally saturated, its specific weight is $\gamma_{sat} = (1-\varphi)\,\gamma_m + \varphi\,\gamma_w$ with γ_w $[N/m^3]$ being the water specific weight. If the water table is located at distance r above the potential failure surface (see blue solid line in Figure 1.1), the vertically averaged specific weight is defined as $\gamma_s = (1-m)\gamma_d + m\gamma_{sat}$, where m $[-]$ is the normalized free surface height given by $m = r/h$ where h $[m]$ is the soil depth. In this case a steady seepage parallel to the slope occurs and the normal stress is reduced as effective stress σ' due to the hydrostatic pore pressure u:

$$\sigma' = \sigma - u = h[(1-m)\,\gamma_d + m(1-\varphi)(\gamma_m - \gamma_w)]\cos^2\beta = (\gamma_s h - \gamma_w r)\cos^2\beta \tag{1.3}$$

Lastly, the driving force is given by the saturated weight of the element:

$$F_{unstable} = h\,a\,[(1-m)\,\gamma_d + m\,\gamma_{sat}]\sin\beta\cos\beta = h\,a\,\gamma_s \sin\beta\cos\beta \tag{1.4}$$

Accordingly, the factor of safety (1.1) can be written as:

$$FS = \frac{c' + (\gamma_s h - \gamma_w r)\cos^2\beta\tan\phi'}{h\,\gamma_s \sin\beta\cos\beta} \tag{1.5}$$

It is important to observe that only the equilibrium in the direction orthogonal to the sliding plane is satisfied in the IS model whereas the equilibrium along the sliding plane is simplified, neglecting the forces that can be transmitted along the boundaries between the considered block and the upper and lower ones. Accordingly, in the IS approximation the values of FS in situations of incipient instability does not exactly reflect the stability of the block. Actually, even neglecting the soil resistance to traction, a single block A in incipient collapse is constrained by a stabilizing force F exerted by the block downslope, B. In this case, the value of FS would be underestimated. However, when computing the FS of the downslope block B, one is neglecting the reaction to F exerted by A, that has now a destabilizing role. In this case, FS could be overestimated. However, due to its simplicity the IS hypothesis has been extensively applied in literature, often coupled to hydrological models (e.g. Montgomery & Dietrich, 1994; Rosso et al., 2006) that provide the space and time distribution of the free surface height r or to more simplified GIS based analysis in catchment-scale applications (Dolojan et al., 2021; Xie et al., 2004). More recently, the actual scope of the IS applicability has been questioned. Griffiths et al. (2011) performed stability analysis on slopes with different lengths using the Finite Element Method (FEM in the following), and found that the IS model is accurate only for slopes characterised by a length over depth ratio $\Delta x/h > 16$. As the ratio diminishes the IS predictions deviate significantly from the values provided by the FEM method: e.g. for $\Delta x/h \approx 2$ the IS model returns a slope which is half as stable with respect to the predictions of the FEM under the same conditions (Griffith et al. 2011). This deviation is enhanced if one considers also the role of cohesion. Milledge et al. (2012) performed similar analysis and found that the FS values computed by the FEM always converge to the value provided by the IS method within 5%, when the $\Delta x/h$ ratio exceeds 25 although this limit ratio is affected by the geometry and by material properties of the slope. However, despite its limitations and due to its simplicity, the IS model is still widely used in catchment scale applications, even in presence of $\Delta x/h$ ratio below the reported threshold (e.g. Xie et al., 2004; Chae et al., 2015).

1.2.2 Janbu's method

A well-known method for computing slope stability is the one proposed by Janbu (1973). Due to its hypothesis, the method is categorised as a Force Equilibrium Method (US Army Corps of Engineers, 2003). For our purposes, the main advantage of the Janbu's approach is its applicability to general non-circular shear surfaces, a limitation that characterizes other methods available in literature (e.g. the Ordinary Method of Slices, US Army Corps of Engineers, 2003; the Bishop method, Bishop, 1955) and that limits their applicability in the context of shallow landslides or soil slip problems. Another advantage of the Janbu method is that it is simpler than other complete methods (so defined because they satisfy all equilibrium equations for the whole slope, e.g. Spencer, 1967; Morgenstern & Price, 1965), which are computationally too expensive to be applied in a distributed approach at basin scale. Let's consider a rather general soil slope, as shown in Figure 1.2, in which the shear surface between AB (solid red line), is assumed to be known *a priori*.

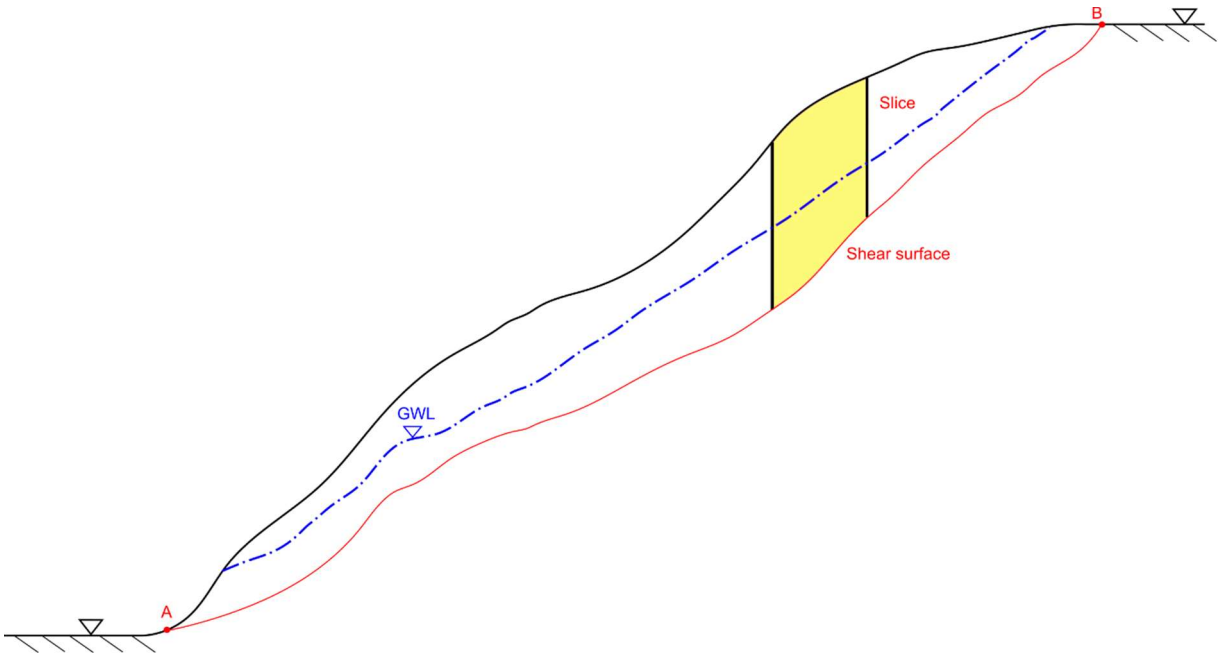

Figure 1.2 Visualisation of the Janbu method applied to a soil slope of general shape.

The depicted shear surface is only one among the infinite possible slip surfaces. The shear surface that gives the minimum FS value is defined as the critical shear surface and if $FS \leq 1$ then it is called a potential slip surface or failure surface (Janbu, 1973). Let us subdivide the slope into an appropriate number of slices by vertical lines, so that the local gradient can be well represented by the angle β. The forces acting on the boundaries of each slice are shown in Figure 1.3.

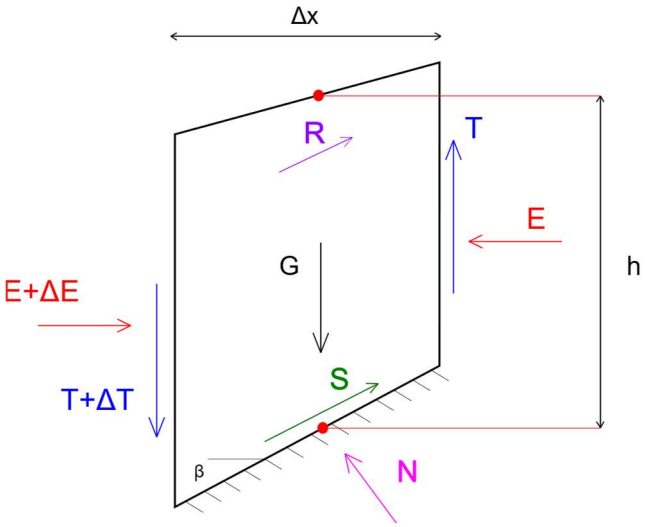

Figure 1.3 Forces acting on a single slice.

The total interslice forces acting in the horizontal and vertical direction are E and T respectively; N and S are the integrals of the normal and shear stress distribution acting along the shear surface. G is the weight of the slice. Although not present in the original formulation of Janbu (1973), in the following the lateral contribution represented by the term R is provided both by root cohesion and lateral earth pressure on both sides of the element (Dietrich et al., 2008). According to the so called *simplified Janbu's method* (Janbu, 1973) it is assumed that the interslice forces are very similar inside each block, i.e. $\Delta T_i \approx 0$, and that all the blocks in the slope have the same FS value. Accordingly, eq. (1.1) can now be written:

$$FS = \frac{S_{max} + R_{max}}{G \sin\beta - \Delta E \cos\beta} \tag{1.6}$$

where ΔE could be positive or negative and R_{max} is the maximum resisting contribution provided by two lateral boundaries exerted both by the roots present in the soil and by the confinement action of lateral earth pressure that can be written as the depth-averaged lateral earth pressure multiplied by the tangent of the effective soil friction angle (e.g. Dietrich, 2008; Chugh, 2003; Arellano & Stark, 2000; Burroughs, 1985):

$$R_{max} = 2c'_r \, \Delta x \, h + k_0(\gamma_s h - \gamma_w r) \cos^2\beta \, \Delta x \, h \tan\phi' \tag{1.7}$$

with c'_r $[N/m^2]$ being the lateral effective soil cohesion and $k_0 = (1 - \sin\phi')$ is the earth pressure coefficient at rest. Under the assumption of plane strain conditions, it is possible to write the vertical equilibrium of the i-th slice along the slope:

$$-G_i + N_i \cos\beta_i + S_i \sin\beta_i + R_i \sin\beta_i - \Delta T_i = 0 \tag{1.8}$$

By writing the block equilibrium in the direction of the sliding plane and considering eq. (1.6) one can easily see that:

$$S_i + R_i = \frac{S_{max,i} + R_{max,i}}{FS} \tag{1.9}$$

which is verified under the reasonable hypothesis that:

$$S_i = \frac{S_{max,i}}{FS}; \qquad R_i = \frac{R_{max,i}}{FS} \tag{1.10}$$

that can be written as:

$$S_i = \frac{c' a_i + (N_i - u_i \, a_i) \tan\phi'}{FS}$$
$$R_i = \frac{2c'_r \, h_i \, \Delta x + k_0(\gamma_s h_i - \gamma_w r_i) \cos^2\beta_i \, h_i \, \Delta x \tan\phi'}{FS} \tag{1.11}$$

Combining eq. (1.8) and eq. (1.11) one obtains N_i for the i-th slice:

$$N_i = \frac{G_i - \frac{\sin\beta_i}{FS}[c' a_i - u_i \, a_i \tan\phi' + 2c'_r h_i \, \Delta x + k_0(\gamma_s h_i - \gamma_w r_i)\cos^2\beta_i \, h_i \, \Delta x \tan\phi'] + \Delta T_i}{\cos\beta_i + \frac{\tan\phi' \sin\beta_i}{FS}} \tag{1.12}$$

Moreover, an independent equation can be obtained by writing the horizontal equilibrium for the whole slope:

$$\sum_{i=1}^{n}(N_i \sin\beta_i - S_i \cos\beta_i - R_i \cos\beta_i) = E_A - E_B \tag{1.13}$$

where E_A and E_B are the horizontal forces acting on the shear boundary at lower and upper end of the slope respectively. Using rigorous FEM analysis, Griffiths et al. (2011) showed that for long and steep slopes the failure mechanism is likely to be located at the top of the slope where tensile forces are dominant (location B). On the other hand, considering short slopes, the dominant failure is likely to occur at the toe, where compressive forces are dominant (location A). Considering a long slope, it is a conservative assumption to consider the difference $E_A - E_B$ negligible. Inserting eq. (1.11) into eq. (1.13) one can write:

$$\sum_{i=1}^{n} N_i \sin\beta_i = \frac{1}{FS}\sum_{i=1}^{n}[c'\ a_i + (N_i - u_i\ a_i)\tan\phi' + 2c'_r h_i\ \Delta x + k_0(\gamma_s h_i - \gamma_w r_i)\cos^2\beta_i\ h_i\ \Delta x \tan\phi']\cos\beta_i \tag{1.14}$$

and, by rearranging the last equation the safety factor FS can be obtained:

$$FS = \frac{\sum_{i=1}^{n}\{c'\ a_i + [N_i(FS) - u_i\ a_i + k_0(\gamma_s h_i - \gamma_w r_i)h_i\ \Delta x \cos^2\beta_i]\tan\phi' + 2c'_r h_i \Delta x\}\cos\beta_i}{\sum_{i=1}^{n} N_i(FS)\sin\beta_i} \tag{1.15}$$

Eq. (1.15), along with the definition of N_i given by eq. (1.12), becomes a polynomial equation of degree n that can be solved numerically for the unknown overall safety factor FS. It can be shown that the hypothesis $\Delta T_i \approx 0$ of the simplified Janbu's method, provides a stress distribution inside the slope which satisfies both horizontal and vertical equilibrium but not moment equilibrium. Janbu (1973) also proposed a further refinement to consider the interslice shear forces $\Delta T_i \neq 0$ in the so-called *rigorous* Janbu's method, according to which an additional moment balance for each slice is written, obtaining a more complex double iteration process in which all equilibrium equations are satisfied. In the following will be used only the *simplified* Janbu's method, omitting therefore the term *simplified*. To this purpose, it is important to observe that according to the Janbu's method it is possible that one or more slices, that would be locally unstable (stable) are kept in position (put in motion) by the surrounding slices. Accordingly, the method considers the cooperative role of the slope as a whole, improving the purely local equilibrium of the IS approach.

1.3 Progressive slope method using Janbu's approach

Although the scope of the proposed method is wider, in the following soils covering an impervious bedrock will be considered, concentrating the attention on shallow landslides induced by rain (soil slips). As showed, the Janbu's method considers the cooperative role of the slope as a whole, improving the purely local equilibrium of the IS approach. However, the Janbu's method was devised to test the stability of a single slope, whose length is set in advance. This situation is different from what happens in a distributed hydrologic model, where each slope is typically represented as a collection of consecutive cells along the drainage network (see Figure 1.4, upper inset), computed by connecting the steepest directions (e.g. O' Callaghan & Mark, 1984; Pilotti et al., 1996) of a raster Digital Elevation Model (DEM). Actually, each branch of the drainage network can be regarded as a collection of slopes of different length. To better explain this point, consider the example shown in Figure 1.4, where, in the inset, a drainage network is shown for a basin draining to the outlet O. Let us consider the stability of

the 8 cells of the slope that goes from A to B, where B is the local divide. Whilst the Janbu's method has been devised to test whether the whole AB slope is unstable, here our purpose is computing the length of any subset of AB, starting from A, that might be unstable (e.g., 1-2, 1-2-3, …). To this purpose, the Janbu's method must be suitably modified. In Figure 1.4 the longitudinal section of the slope is shown, discretized in slices according to the cell size of the DEM. Theoretical and practical evidence suggests that in case of shallow landslides, i.e. where the length of the slope is much larger than the soil depth h, failure usually occurs at the discontinuity between the soil and the bedrock (e.g. Pierson, 1977; Sidle & Swanston, 1982) or at the surface of discontinuity determined by the wetting front during rainfall events (Rosso et al., 2006).

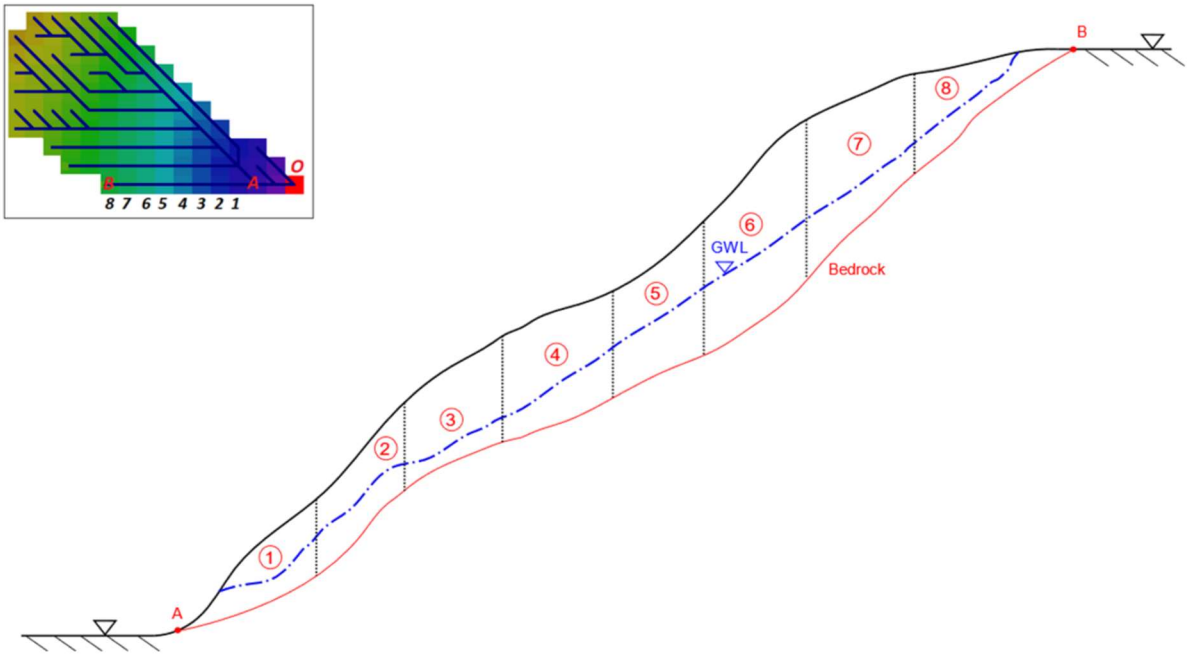

Figure 1.4 Visualisation of a general slope discretized into slices. The top left corner of the picture depicts where the slope is located inside the catchment, with O being the outlet cross section.

In order to find out the length of the subset of AB that is potentially unstable, let us consider cell 1 in Figure 1.4 and let us apply the Janbu's method assuming that the entire slope is made up only by that single cell. Using the following notation as a shorthand:

$$Num_1 = \{c'\, a_1 + [N_1 - u_1\, a_1 + k_0(\gamma_s h_1 - \gamma_w r_1) h_1\, \Delta x \cos^2 \beta_1] \tan \phi' + 2c'_r h_1 \Delta x\} \cos \beta_1$$
$$Den_1 = N_1 \sin \beta_1 \qquad (1.16)$$

in which both Num_1 (Numerator) and Den_1 (Denominator) are functions of the unknown safety factor, which is computed using eq. (1.12) and eq. (1.15) with $n = 1$. One obtains:

$$FS_1 = \frac{Num_1(FS_1)}{Den_1(FS_1)} \qquad (1.17)$$

The solution of eq. (1.17) provides FS_1. Note that at this stage eq. (1.17) is identical to the IS method provided that no lateral contribution is present, i.e. $k_0 = 0$ and $c'_r = 0$. (see Appendix A for details). Considering cells 1 and 2 and compute the functions Num_1, Num_2 and

Den_1, Den_2, to be used into the next equation provides the overall safety factor FS_{1+2},which is now representative of the slope made up by the first two cells:

$$FS_{1+2} = \frac{Num_1(FS_{1+2}) + Num_2(FS_{1+2})}{Den_1(FS_{1+2}) + Den_2(FS_{1+2})} \tag{1.18}$$

Now the solution of eq. (1.18) provides FS_{1+2}, which is the failure surface that spans along the first two slices. In general terms the safety factor for the stretch of the slope that goes from the first cell to the i-th cell can be computed as:

$$FS_{1+\ \dots\ +i} = \frac{\sum_{j=1}^{i} Num_j(FS_{1+\ \dots\ +i})}{\sum_{j=1}^{i} Den_j(FS_{1+\ \dots\ +i})} \tag{1.19}$$

The upper extent of the unstable part of slope AB is given by the largest value of i (if any) for which $FS_{1+\ \dots\ +\ i} < 1$. On the other hand, the FS value computed for the last cell, i.e. the whole slope from A to B, is precisely eq. (1.15), i.e. the classical implementation of Janbu's method to the whole slope. The computation of the stability of the slope, eq. (1.19), requires solving a polynomial equation for each slice present on the slope, which can be effectively done using a Newton Raphson method. However this requirement can be simplified in two directions. First, this computation can be avoided if one is interested only in assessing whether the considered soil slope is stable or not. If this is the case, by inserting $FS = 1$ into eq. (1.19) and carrying all terms on the right side, one obtains a quantity Q given by:

$$Q(1) = \frac{\sum_{j=1}^{i} Num_j(1)}{\sum_{j=1}^{i} Den_j(1)} - 1 \tag{1.20}$$

which is larger than zero if the slope is stable or lower than zero if it is unstable (see Appendix B for a proof of this statement). As a second direction, it can be shown that an approximate solution of eq. (1.19) is provided by the following linearization:

$$FS = \frac{\sum_{i=1}^{n} [G_i \tan\phi' + M_i \cos\beta_i + M_i \sin\beta_i \tan\beta_i]}{\sum_{i=1}^{n} [G_i \tan\beta_i]} \tag{1.21}$$

where M_i is a short-hand notation for $M_i = c'a_i - u_i a_i \tan\phi' + 2c'_r h_i\, \Delta x + k_0(\gamma_s h_i - \gamma_w r_i)\, h_i\, \Delta x \cos^2\beta_i \tan\phi'$ (see appendix C for derivation and further evidence on the topic). By applying this procedure one can check every potential failure surface which starts from the toe of the slope (point A) and ends after each slice (e.g. $FS_{1+2+3+4}$ is the factor of safety associated with the failure surface that joins point A and the end of slice 4).

$$[FS_1 \quad FS_{1+2} \quad FS_{1+2+3} \quad FS_{1+2+3+4} \quad \dots \quad FS_{1+2+\ \dots\ +n}] \tag{1.22}$$

This is only a subset of the possible failure surfaces that may arise in the general slope depicted in Figure 1.4. As an example, the procedure described so far has no way to check the stability of the failure surface located between slices 3 and 5 (e.g. FS_{3+4+5}). To address this issue it is proposed to check every consecutive partition of the slope AB, in order to explore every location which may become unstable inside the slope. So, after computing every FS starting

from A, one can repeat the procedure described excluding the first slice and computing every FS up the slope crest. Therefore, adding a row to the matrix reported in (1.22):

$$\begin{bmatrix} FS_1 & FS_{1+2} & FS_{1+2+3} & FS_{1+2+3+4} & \dots & FS_{1+2+\dots+n} \\ & FS_2 & FS_{2+3} & FS_{2+3+4} & \dots & FS_{2+3+\dots+n} \end{bmatrix} \tag{1.23}$$

Repeating the previous procedure until only the last slice remains leads to the following matrix:

$$\begin{bmatrix} FS_1 & FS_{1+2} & FS_{1+2+3} & FS_{1+2+3+4} & \dots & FS_{1+2+\dots+n} \\ & FS_2 & FS_{2+3} & FS_{2+3+4} & \dots & FS_{2+3+\dots+n} \\ & & FS_3 & FS_{3+4} & \dots & FS_{3+4+\dots+n} \\ & & & FS_4 & \dots & FS_{4+5+\dots+n} \\ & & & & \ddots & \vdots \\ & & & & & FS_n \end{bmatrix} \tag{1.24}$$

Upper triangular matrix (1.24) contains all possible FS of the partitioned slope and, for a slope made of n slices, the number of consecutive partitions to be checked is a triangular number, given by:

$$N° \; of \; checks = \frac{n(n+1)}{2} \tag{1.25}$$

As an example the number of consecutive partitions to be explored in a slope made up of 4 slices is 10, i.e. (1), (1-2), (1-2-3), (1-2-3-4), (2), (2-3), (2-3-4), (3), (3-4) and (4). Within each i-th row, the value of the (i, j) cell indicates the overall FS for the failure surface which spans from the i-th slice to the j-th slice. On the other hand, the FS for the i-th slice can be obtained considering the minimum FS of all the slopes or sub-slopes (some collection of slices) that contain the i-th slice, that can be achieved using the following procedure:

1. Apply the proposed Janbu's method to the slope under study and compute each entry of the row matrix reported in (1.22), starting from the first slice.
2. If at any point along the slope (slice k, for instance) a $FS_{1+2+\dots+k} < FS_{1+2+\dots+k-1}$ is computed, meaning a lower factor of safety is encountered along the slope, then all FS values before it, i.e. $FS_1, FS_{1+2}, FS_{1+2+\dots+k}$ are set equal to the newly computed value $FS_{1+2+\dots+k}$. This condition states that a newly discovered shear surface has a lower factor of safety with respect to the previously analysed ones, therefore it is in a less stable configuration. The simple condition described works regardless of whether $FS > 1$ or $FS < 1$, therefore is general to both stable and unstable slices or collection of slices. After this step, by looking at the output, it is possible to notice that along each collection of slices, i.e. along each row of matrix (1.24), the FS values can never decrease, otherwise the condition $FS_{1+2+\dots+k} < FS_{1+2+\dots+k-1}$ is violated.
3. Repeat step 2 for every partition of the slope.
4. Finally, after each entry of the upper triangular matrix (1.24) is computed, a summary of the actual FS values along the slope can be obtained by taking the minimum value along each column of matrix (1.24).

It is interesting to note that the diagonal terms of matrix (1.24) are the FS values considering just a single slice, which, when the lateral contribution is neglected, are identical to the FS computed using the IS model. Accordingly, to avoid the overprediction bias of unstable areas, that besets the IS method, the extraction of the minimum in the submatrices of matrix (1.24) can be done excluding the main diagonal: in this way, only the failure surfaces with at least two slices are considered when flagging the unstable areas.

1.4 Controlled test cases

The application of a stability model to a real watershed case is affected by many uncertainties, largely related to the amount of geotechnical and hydrologic data that this type of evaluation would demand. Accordingly, before proceeding with the application of the proposed progressive procedure to a real watershed, its performance must be tested against the results of more rigorous methods (e.g. the Morgenstern & Price procedure, whose stability analyses satisfies all equilibrium equations) applied to some elementary test cases, where all the data are known. In the following, the unstable areas are computed for two simple test slopes with different methodologies: using the proposed progressive Janbu's method, the IS method and the Morgenstern & Price procedure. The output of Morgenstern & Price procedure is considered as the reference solution, since both the factor of safety and the position of the critical failure surface area provided by this method are very close to the output provided by a FEM analysis performed with the same conditions (Cheng & Lau, 2014). For simplicity's sake in the following test cases $k_0 = 0$ and $c'_r = 0$. In all test cases the software GeoStudio (SLOPE/W module) has been used to dynamically test all admissible failure surfaces that can arise in a given slope and display only the ones that are characterized by a factor of safety that is smaller than unity. The software has been used to compute the reference solution, choosing the half-sine function as an interslice shear force function, as customary for stability analysis (Cheng & Lau, 2014). All the considered slopes are analysed in fully saturated conditions with a static water table located at the soil surface.

1.4.1 Slope change test case

The first test case consists of the idealized slope shown in Figure 1.5. The slope is equally divided into two portions: the first 50 m stretch has a constant gradient of 11°, while the remaining portion is characterized by a uniform steeper gradient of 27°. The geotechnical characteristics of the soil are reported in Figure 1.5.

Slices	1 – 10	11 – 20
$h - [m]$	1	1
$\beta - [°]$	11	27
$\Delta x - [m]$	5	5
$m - [-]$	1	1
$\gamma_{sat} - [N/m^2]$	19 743	19 743
$c' - [N/m^2]$	2 500	2 500
$\phi' - [°]$	30	30

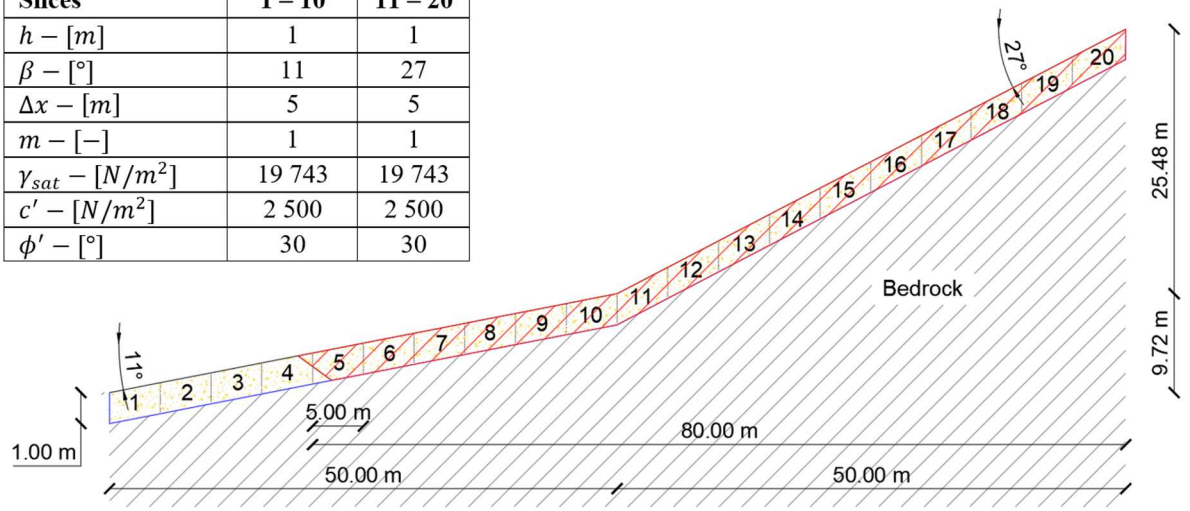

Figure 1.5 Visualization of the analysed slope. The depth of soil along the slope has been enlarged for graphical reasons. The inset on the left shows the geotechnical properties of the soil. h is the soil depth, β is the inclination of the slice, Δx is the slice length, m is the normalized free surface height (the slope is completely saturated), γ_{sat} is the saturated unit weight of the soil, c' is the effective cohesion of the soil and ϕ' is the effective friction angle. The parameters are constant throughout the slope, except the gradient which changes between slices 10 and 11. The red shaded area is the amount of soil that is unstable ($FS < 1$) in the current configuration using SLOPE/W (GeoStudio).

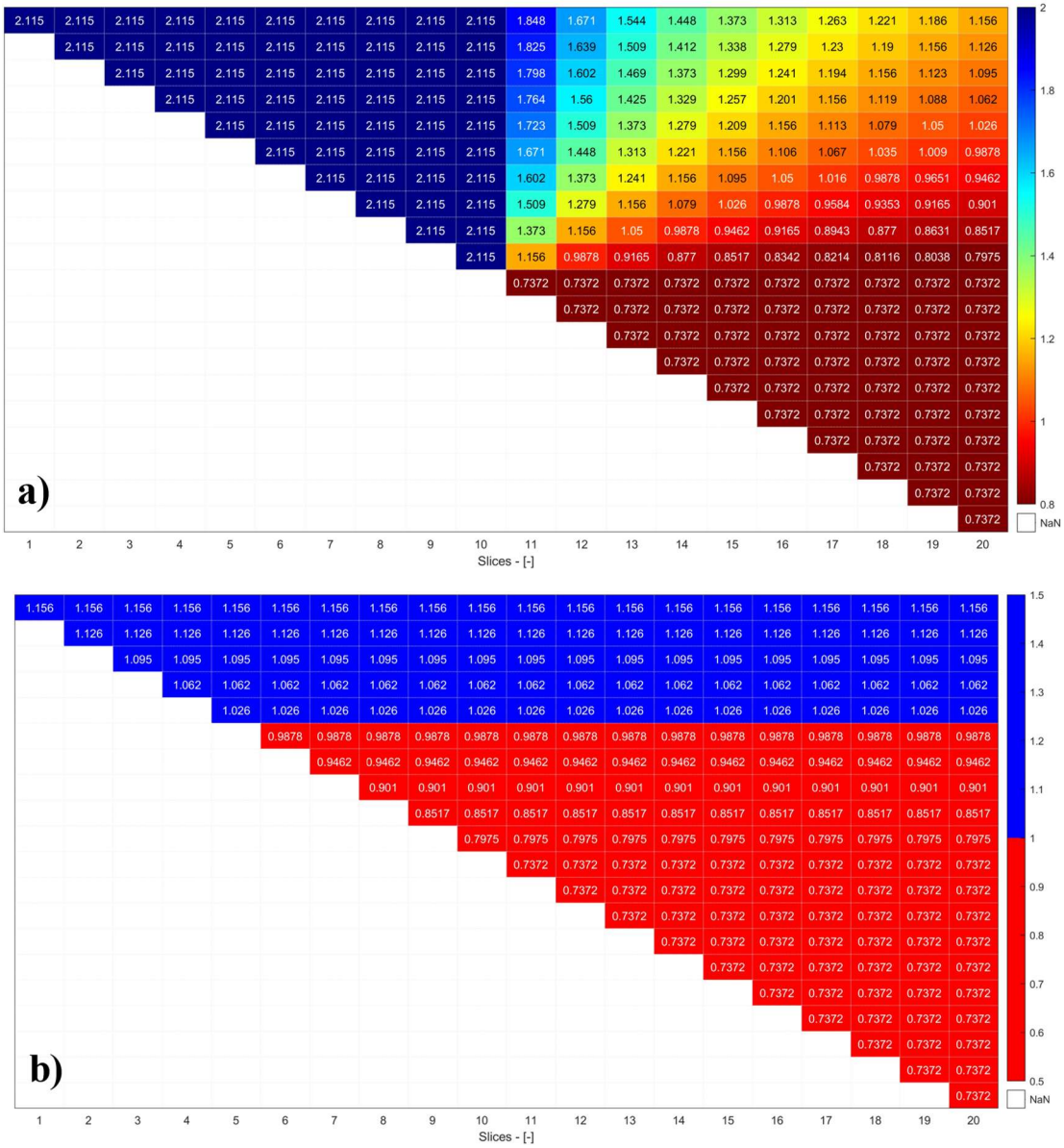

Figure 1.6 Steps for the application of the progressive Janbu's method. a) Matrix presented in (1.24) for the slope reported in Figure 1.5, so far the FS values displayed are those computed using the progressive Janbu's method without applying the procedure discussed previously (Step 1). b) Matrix presented in (1.24) after the application of the second step of the described procedure (Step 2), as one can notice, along the rows and spanning the columns from left to right, all values are either constant or increasing.

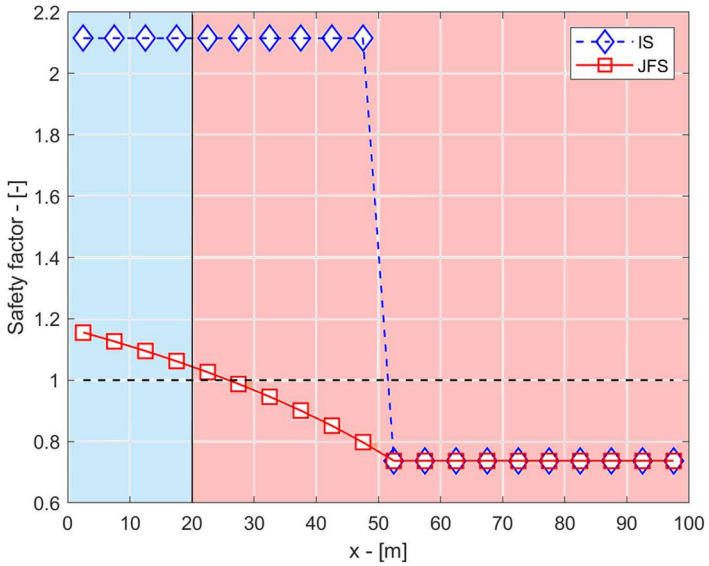

Figure 1.7 Computed safety factor using the proposed Janbu's method (JFS) and Infinite Slope method (IS). The values of JFS are obtained from the matrix shown in Figure 1.6 by taking the minimum FS value along each column, as explained in the text. The light blue and red shadings represent the stable and unstable areas computed using SLOPE/W.

In Figures 1.5 and 1.7 the output of SLOPE/W for the proposed slope is reported. The red-shaded area spanning from the 20 m station up to the top of the slope is computed as unstable. As can be seen, the instability of the steeper region also affects the upper part of the less steep region. Figure 1.6b shows the matrix (1.24) for the slope under investigation: as one can observe, several slices that would be wrongly considered stable based on a purely local analysis turn out to be unstable due to the destabilizing contribution of the upper slices. For instance, notice how in row 6, which corresponds to the shear surface which starts from the 25 m mark going upstream, the slope would be stable up to the second-last slice, as highlighted by the values of the factor of safety. Then, if the contribution of the last slice is considered, the overall slope is no longer stable since the factor of safety reported in the last column of row 6 is less than 1 (i.e. $FS_{6+7+\ldots+20} < 1$). This newly computed factor of safety is then assigned to all slices already encountered, flagging them as unstable, according to the procedure discussed in the previous section. To summarize the entries of matrix depicted in Figure 1.6b in a single line plot, for each column the minimum FS value that has occurred has been reported in Figure 1.7, which displays the final output of the progressive Janbu's method, together with the IS method and SLOPE/W. As explained above, to avoid overpredicting unstable areas, as done by the IS method, the extraction of the minimum along the columns of matrix (1.24) is done excluding the main diagonal. Actually, a factor of safety less than one of the i-th element of the main diagonal means that the i-th slice of the slope is unstable on its own: however, this situation may change when also the surrounding slices are considered, in contrast to the results provided by the IS method. Figure 1.7 shows that, as expected, the IS model is unable to predict unstable slices in the milder stretch since it considers only local contributions, whereas the proposed Janbu's method is able to correctly predict a failure even in the less steep region. Overall, the proposed Janbu's method predicts failure for the last 75 m, while the IS method only for the last 50 m. Using the output shown in Figure 1.5 as a reference solution, we can say that in this case the proposed Janbu method detects 93.75% of the overall unstable area while the IS

method only 62.50%. This case provides a clear example of the limits of the IS approach in a simple situation which however may arise inside any stability analysis at the basin scale. Although in this example we used a small $\Delta x/h$ ratio $5/1 = 5$, the computation of the stability along the less steep part of the slope does not improve when a larger dimension of the cells, up to $50/1 = 50$, is used.

1.4.2 Parabolic slope

In this second example (see Figure 1.8), the profile of the slope is given by the equation $z = 2\sqrt{x}$, where x is the space coordinate, spanning 20 m. As the equation implies, the slope is initially steep and becomes progressively mild towards the top.

Slices	**1 – 20**
$h - [m]$	0.8
$z - [m]$	$2\sqrt{x}$
$\beta - [°]$	$\tan^{-1}(x^{1/2})$
$\Delta x - [m]$	1
$m - [-]$	1
$\gamma_{sat} - [N/m^2]$	19 743
$c' - [N/m^2]$	3 000
$\phi' - [°]$	30

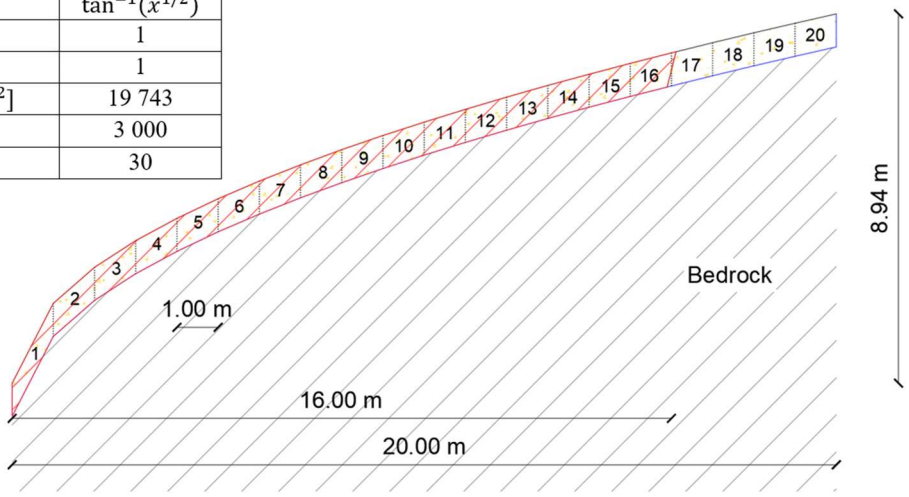

Figure 1.8 Visualization of the parabolic slope. In the top left corner the geotechnical characteristics of the soil are reported. The elevation data and base angles are given as a function of the space coordinate x, which starts at the beginning of slice 1. The red shaded area is the amount of soil that is unstable ($FS < 1$) in the current configuration using SLOPE/W (GeoStudio).

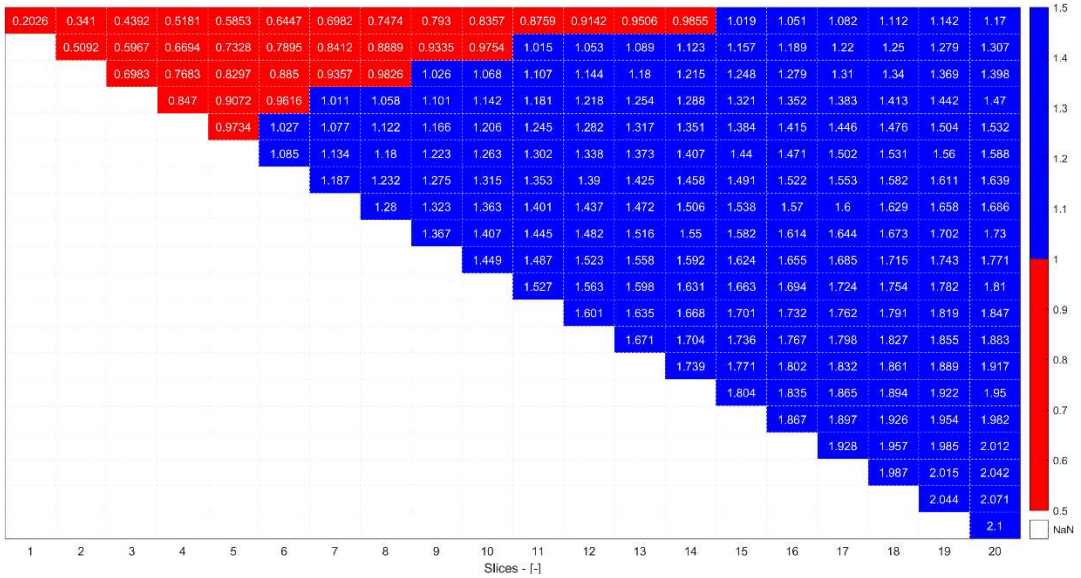

Figure 1.9. Final output of the progressive Janbu's method, the red shaded entries are characterized by a $FS < 1$ (unstable), while for the blue shaded entries $FS > 1$ (stable).

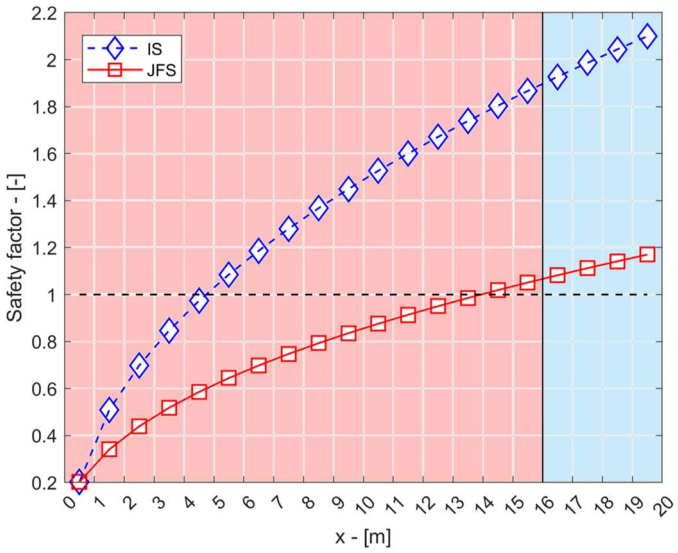

Figure 1.10 Computed safety factor using the proposed Janbu's method (JFS), obtained by taking the minimum along each column of the matrix reported in Figure 1.9 and the Infinite Slope method (IS). The light red shaded area of the figure, spanning from 0 to around 16 m displays the unstable portion computed by SLOPE/W, contrary to the light blue shaded area which is the stable portion.

The slope is discretized with $\Delta x = 1\ m$, an ordinary resolution in current DEM that are usually obtained by high resolution LIDAR survey. Accordingly, the $\Delta x/h$ ratio (slice by slice) is $1/0.8 = 1.25$, well below the validity thresholds of the IS model. In Figure 1.8 and 1.10 the output of SLOPE/W for the presented slope is shown. The red-shaded area along the first 16 m of the slope is flagged as unstable. Figure 1.10 shows that, according to the IS model, only the first 4.5 m of the slope would be unstable, while the proposed Janbu's method computes the first 13.5 m of the slope as being unstable. Accordingly, the proposed implementation of the Janbu's method detects 84.38% of the unstable area while the IS method just 28.12%.

1.5 Extension to the watershed scale

The analysis of the synthetical test cases showed the superiority of the proposed method over the IS method. On the other hand, the method is relatively more complex with respect to the IS, that is based on a pure local analysis and it is important to show its actual applicability at the watershed scale. To this purpose in the following it is presented the application of the proposed methodology to a study area which has been widely discussed in the literature: the Mettman Ridge case, Oregon (e.g. Bellugi et al., 2015; Rosso et al., 2006; Dietrich et al., 2001; Montgomery & Dietrich, 1994). Although the high level of uncertainty in the soil description is the real stumbling block when dealing with real watersheds, in this case, the data required to run the model are obtained from the online repository provided by Bellugi et al. (2015, 2021). Accordingly, the use of a reference test case and of the corresponding dataset as input avoids the parametric uncertainty of the problem, allowing a direct comparison with previous results. In order to identify the areas which are potentially unstable at the watershed scale during a rainfall event, a distributed hydrologic model must be implemented which incorporates a stability model. The hydrologic model should provide the transient soil saturation at each site in the watershed, to be used in the stability model, as well as the shallow subsurface flow and

surface runoff. In the following a proprietary distributed hydrologic model whose structure is an evolution of Pilotti and Rosso (1990) will be used. Using a DEM of the watershed, the model first computes the watershed Space Filling Drainage Network (SFDN, e.g. Pilotti et al., 1996) and then, by using suitable filtering algorithms, the channel network (see Figure 1.11). These two networks are codified as topologic non-binary tree-like structures, where each node corresponds to a cell of the original DEM. All the watershed cells are connected in the SFDN and water is transferred along the SDFN non-binary tree using suitable recursive algorithms for tree traversal described in Pilotti et al. (2019). Each node has direct access to the geomorphological and topologic information of the locally drained watershed and is connected downstream to a single node in the steepest direction.

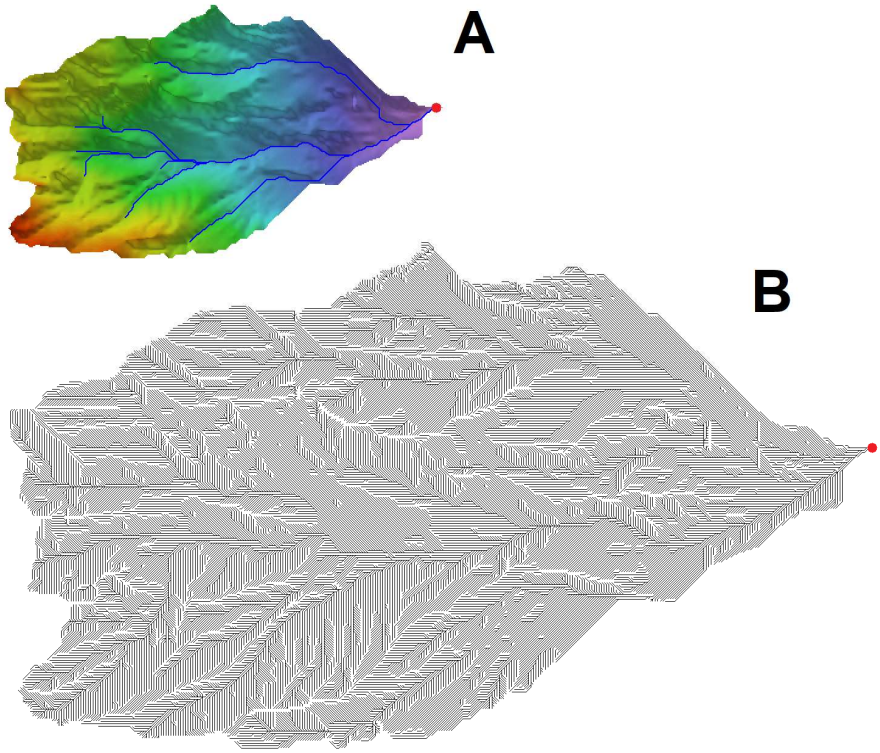

Figure 1.11 Space filling drainage network, SFDN, (B) derived from the DEM of the basin (A). The red dot is the basin outlet. From the SFDN it is possible to extract different channel networks, e.g., the one shown on the DEM (A) surface, computed according to a slope dependent contributing area ($C = 0.1\ km^2$, $\alpha = 1.7$, where C and α are two parameters controlling the channel extraction).

Figure 1.12 shows the hydrological processes that are computed within each cell of the SFDN. The hydrologic model is parametrized as a function of suction, porosity, saturated permeability, and soil depth (used by the Green-Ampt method and Darcy's equation) and local Manning's coefficient (for surface runoff computation). These quantities can be provided either as a single uniform value in the basin or as distributed maps when more detailed data are available. Each cell has a two-storage structure, where the effective depth of the subsurface storage is controlled by the soil depth and porosity. Runoff and subsurface flows are modelled according to a kinematic wave approach, that makes use of a modified Manning's equation for runoff and of Darcy's equation for subsurface flow. As proposed by D'Odorico et al. (2005), the model takes into account both the topography-driven groundwater table and the moisture content related to the wetting front computed by the Green-Ampt method (Rosso et al., 2006) during a rainfall event; typically, the two processes have different time scales, as shown by Iverson

(2000), and both cause a build-up of pore water pressure that can trigger soil failure. Accordingly, the stability model assumes that failure occurs either within the soil column at the local wetting front, or at the soil bedrocks boundary (e.g. Megahan et al., 1983).

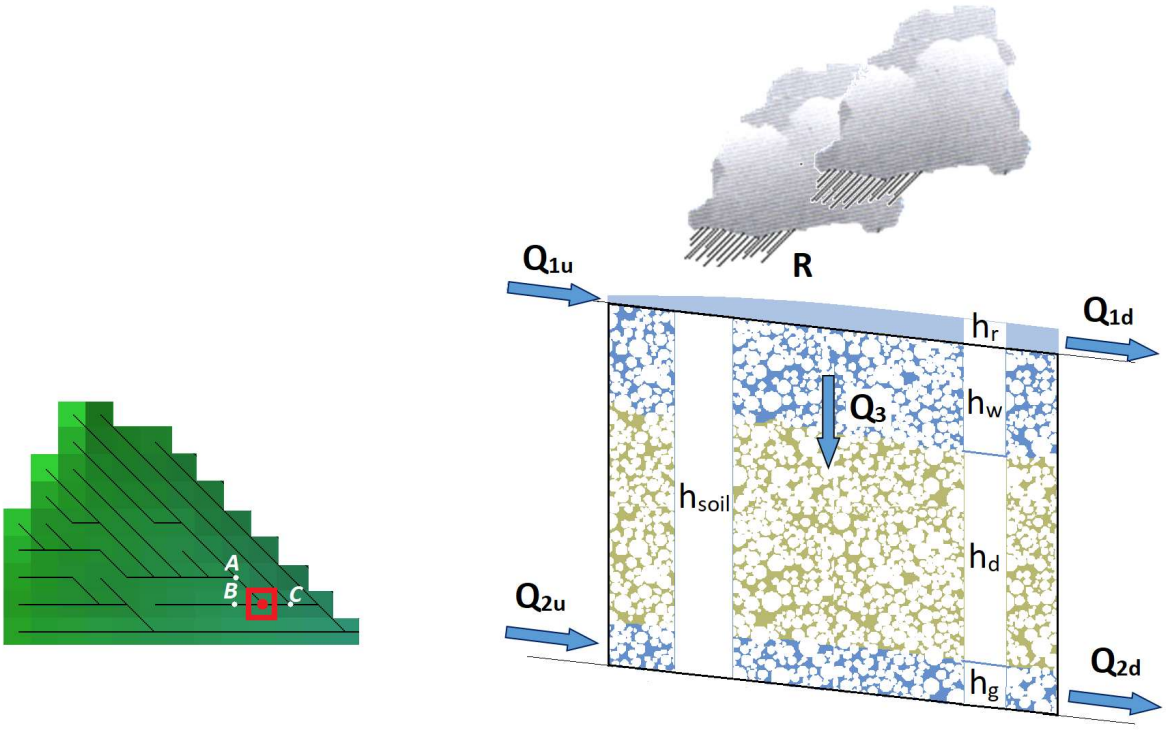

Figure 1.12 Hydrological processes computed within each cell of the Space Filling Drainage Network. The block on the right is a vertical-section of the cell framed in red on the left, that receives inflow from cells A and B and feeds cells C. Net rainfall is computed from local rainfall R using the Green-Ampt method. Net rainfall contributes to the water depth h_r of the upper storage, whose balance provides local runoff Q_{1d} on the basis of incoming runoff Q_{1u}, from upstream cells A and B and of Manning's equation. h_w is the thickness of the saturated layer from above, i.e. the position of the wetting front of the infiltrating rainfall. When $h_w = h_{soil}$, the wetting front is on the bedrock and a shallow aquifer parallel to the soil surface is considered for the giving block. The local aquifer balance uses Q_{2u} (different from zero only if an aquifer is present at cells A or B) and Q_{2d}, that is computed according to Darcy's equation. The balance provides h_g, the thickness of the saturated layer on the bedrock. Considering that an aquifer can be originated also by Q_{2u}, it can be present in a cell even if $h_w < h_{soil}$. In this case two saturated layers are locally present, separated by a conceptually dry layer $h_d = h_{soil} - (h_w + h_g)$.

By simulating the rainfall-runoff transformation along the SFDN, the model effectively takes into account the morphology of the channel network. A simple example that shows the influence of the slope topography on the dynamics of soil saturation is shown in Figure 1.13 for an elemental hillslope made with a sequence of 28 cells, each with a side of 10 m. Three different elevation profiles have been considered: linear (case A), convex (B) and concave (C). The slope is initially dry with a uniform distribution of soil depth $h_{soil} = 0.4\ m$, porosity $\Phi = 0.3$ and suction $\Psi = 0.19\ m$ and saturated permeability $K = 8.3 \cdot 10^{-5}\ m/s$. A steady rainfall of $0.05\ m/h$, lasting three hours, has been assumed. The coloured maps on the right of Figure 1.13 show the time and space evolution of slope saturation during 20 days after the end of the event, in the three cases of linear, convex and concave slope. Red colour indicates complete saturation that is also the initial condition of the three slopes. In contrast, the violet colour indicates the minimum level of saturation, which is followed by desaturation (white). Whilst in the case of the linear slope A, desaturation proceeds at the same rate from upstream to

downstream, in the case of the convex slope B this is not the case. The steepest cells are desaturated more rapidly, and a perching aquifer remains whose slow desaturation feeds the downstream cells. Finally, in the concave slope the faster desaturation of the upper part of the basin keeps a prolonged high saturation level at the foothill.

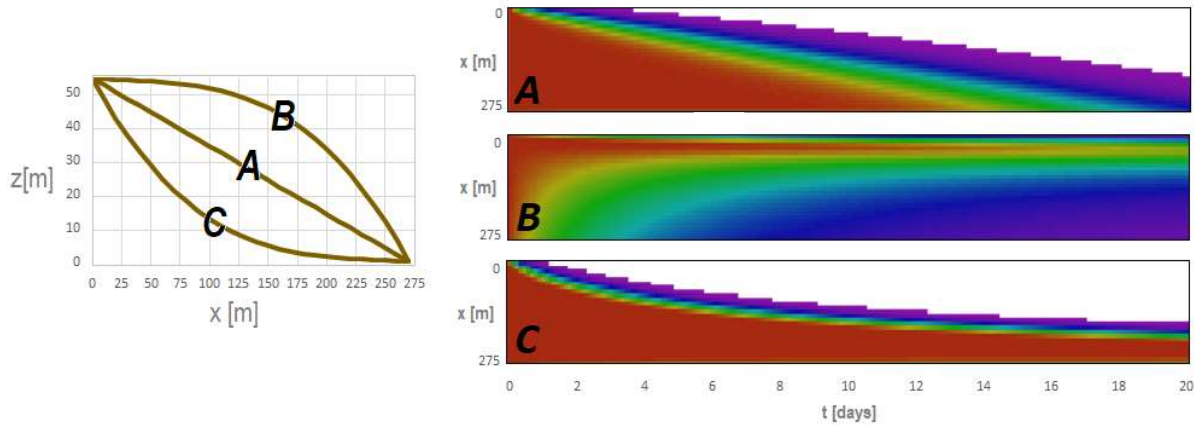

Figure 1.13 Space-time evolution of average soil saturation along three 1D slopes with the curvatures shown on the left. Along a 20 days long period the saturation decreases from 1 (red) to 0 (white) with different patterns that reflect drainage and accumulation governed by the local slope.

After each time step of the simulation of the rainfall-runoff transformation, the SFDN is visited to compute stability according to equation (1.19), using local values of friction angle and cohesion. In this way, the time varying map of FS throughout the watershed can be computed.

1.6 Mettman Ridge application

The Mettman Ridge study site (see Figure 1.14) has an area of 0.5 km^2 and consists of steep, highly dissected soil-mantled hillslopes with narrow ridges and steep channels (Bellugi et al., 2015). As a crucial information to validate a model that must predict susceptibility to areas which may become unstable in a catchment, an inventory of landslides occurred over a 10 year period is available for this area (Montgomery et al., 2000). Despite using a real test case to effectively validate the modelling chain it is proposed to consider a well-studied basin in Oregon which has been extensively studied with all parameters fixed allowing to focus only on the performance of the stability model.

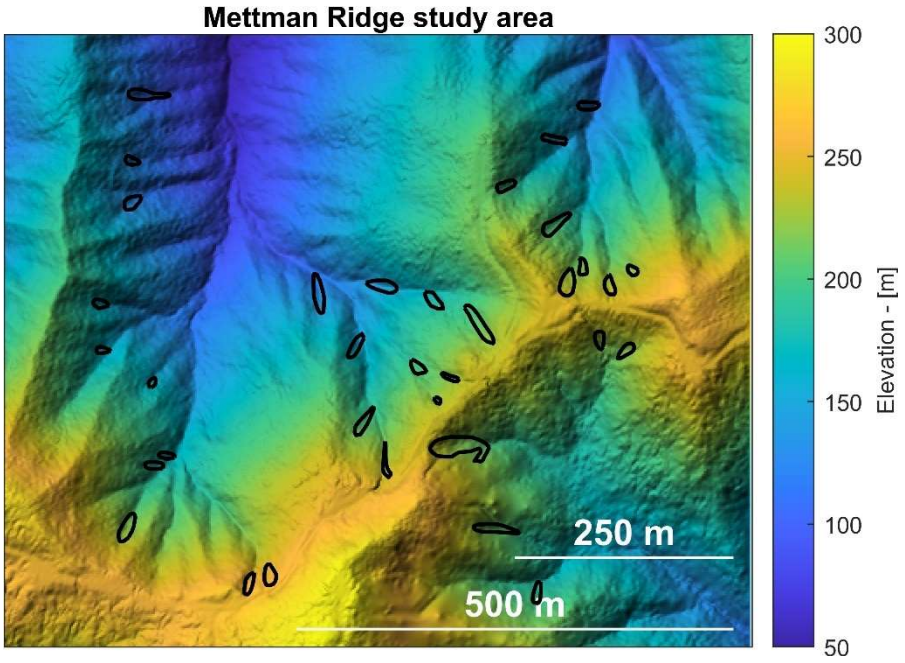

Figure 1.14 Elevation data of the Coos Bay, OR, study site. The solid black polygons represent the mapped landslides that occurred over a 10 year period (Montgomery et al. 2000).

The following data from the online repository by Bellugi et al. (2015, 2021) were used:

- DEM data: available from the online repository, 2 m resolution.
- Soil depth map: available from the online repository, 2 m resolution. The map has been estimated coupling an exponential soil production term (Heimsath et al., 2001) with a nonlinear diffusive term (Roering et al., 1999), following the framework reported in Dietrich et al. (1995): see Bellugi et al. (2015) for a more detailed description.
- Root cohesion map: available from the online repository, 2 m resolution. Data is taken from the work of Montgomery et al. (2009) who measured the spatial distribution of root type, root diameter, root/area ratio and root depth in a portion of the study area. Experimental data suggested that the relationship between root cohesion and depth at the site is represented by a negative exponential function (Bellugi et al., 2015) which has been used to compute the basal cohesion in every point of the catchment.
- Lateral cohesion map: available from the online repository, 2 m resolution. The average lateral root cohesion per unit perimeter area has been computed as the integral of the root cohesion over the soil thickness (Bellugi et al., 2015).
- Soil saturation map: available from the online repository, 2 m resolution. Saturation data reported is obtained using the transient hydrologic model proposed and applied by Rosso et al. (2006) to this test case considering high intensity typical storms that occur across the catchment.
- Soil friction angle: constant value of $40°$ across the whole catchment.
- Saturated soil unit density: constant value of $1600\ kg/m^3$ across the whole catchment.

In Figure 1.15 the results provided by the IS model and the proposed model based on the Janbu's method are compared. Figure 1.15 shows that the IS model correctly predicts all the unstable areas: however it shows a significant tendency to overpredict unstable areas. On the other hand, the proposed Janbu's method fails to predict all the unstable areas but the overprediction is significantly reduced. To give a numerical score between these different

classifiers of unstable areas, it is customary to use the receiver operating curves (ROC) (Metz, 1978) which are computed on the basis of the surveyed landslides shown in Figure 1.14. If an unstable cell ($FS < 1$) falls inside an area which has been mapped as unstable then it is counted as true positive (TP), if not then it is flagged as false positive (FP). Similarly, if a stable cell ($FS > 1$) falls inside an area which has been mapped as unstable then it is flagged as false negative (FN), if not then it is counted as true negative (TN). These well-known quantities allow to define the true positive rate (TPR) and true negative rate (TNR), as done by Montrasio et al. (2022):

$$TPR = \frac{TP}{TP + FN}$$
$$TNR = \frac{TN}{TN + FP} \tag{1.26}$$

In Figure 1.16 the ROC curve is represented on the TPR-FPR plane as a function of the factor of safety used to distinguish between stable and unstable areas, with FS varying between 0.6 and 6 with 0.1 steps. By integrating the areas below a ROC curve one is able to obtain a numerical information about the quality of the binary classifier (stable, unstable) being tested. The higher the area under the ROC curve (AUC) the higher the quality of the classifier.

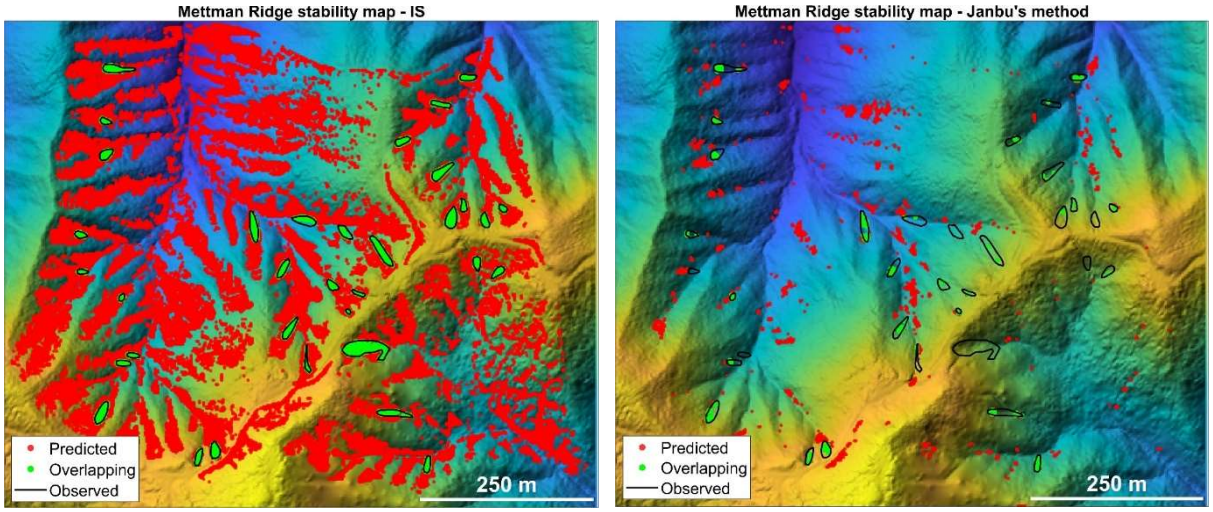

Figure 1.15 (Left) Stability map output of the IS model. (Right) Stability map output of the Janbu's method. The red dots indicate the areas which are computed as unstable even if they are not inside the observed unstable areas (black polygons). The overlapping between observed and computed unstable areas is displayed in green.

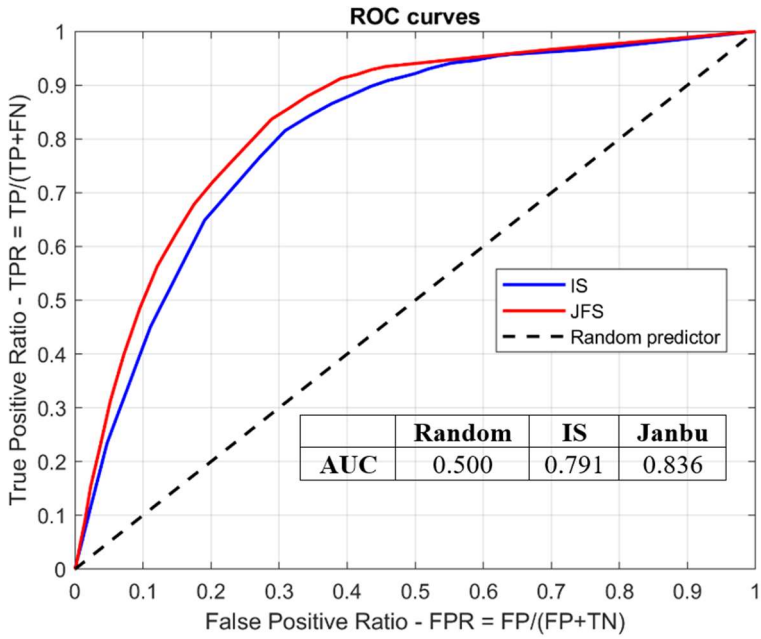

Figure 1.16 Receiver operating curves (ROC), for the IS (showed in solid red) and the proposed Janbu's method (showed in solid blue). The table shows the values of the area under the curve (AUC) for each model. AUC = 1 would correspond to a perfect classification with no mistakes.

Figure 1.16 confirms that the IS model (AUC = 0.791) performs better with respect to the random classifier (AUC = 0.500), i.e. just assuming a 50% chance that each cell is unstable. On the other hand the Janbu's method proves itself to be a robust classifier, performing slightly better with respect to the other models (AUC = 0.836).

1.7 Discussion

Debris flows triggered by soil slips are a relevant hazard in many mountainous regions worldwide, causing destruction of properties and claiming a significative death toll each year. Accordingly, in several nations real-time monitoring and forecast systems are being developed for managing measures of civil protection in case of emergency. Very often these systems rely on estimated rainfall thresholds for landslides triggering (e.g. Baum & Godt, 2010). However this approach is purely regressive at best, not capable of differentiating the peculiarities of the mountain territory and of the saturation history at the time of landslide occurrence. Finally, it provides a vague information about something that could happen somewhere within a wide territory. To be effective, a forecast system needs something more precise. On a line of principle, physically based models, working on accurate weather forecast, will be the appropriate solution. Within the limits of the approximations made in reproducing the complex processes involved in soil hydrology, these models will provide exact position of potential landslides within a watershed, in response to a specific rainfall event and considering the past saturation history of the watershed. In this direction, the use of DEM with increasing space resolution, provided by widely used LIDAR technologies, allows a better reproduction of local slope, flow propagation and soil saturation build-up during rainfall events at the watershed scale. On the other hand, when a DEM is coupled to a hydrologic model to identify potential soil slips, growing the resolution implies that the stability of a cell cannot be analysed independently from the stability of the surrounding cells. According to Milledge et al. (2012), when the $\Delta x/h$ ratio is smaller than 16, the adequacy of the IS assumption, the most widely

used approach for this purpose, is questionable. In the author's opinion, although this problem is intrinsically affected by a disproportion between the necessary data and the typically available data, this does not exempt one from trying to reduce the margins of uncertainty by identifying better methods for the calculation. The method proposed in this contribution is an adaptation of the well-known Janbu's method to space-distributed application. It is a computationally viable compromise in the path between a FEM computation of soil stability and the IS method. The method has been analysed with three different tests. The synthetic test cases have shown the superiority of this methods in situations where everything is known and the actual soil stability is provided by the FEM method. In both cases the IS underestimates the extent of the unstable soil because it neglects the destabilising role of the surrounding blocks. The modified Janbu's method matches 94% and 84% of the unstable soil. On the other hand, the Mettman Ridge case shows that the IS has a dramatic tendency to overpredict unstable areas, a flaw well documented in the literature (Bellugi et al., 2015). Figure 1.15 shows that most of the cells are classified as unstable by the IS, strongly limiting the usefulness of the results of this model in practical situations. Considering the discretization of the DTM used in the last application (2 m), and the average soil depth in the basin (0.67 m), then it is evident the reason behind the poor performance of the IS model, i.e. the relatively low $\Delta x/h$ ratio being roughly around 3, well below the threshold of 16 highlighted by Milledge et al. (2012). Aside from the performances of the proposed methodology on fixed datasets, as the one of the Mettman Ridge, every modelling chain which aims to predict soil instability due to rainfall events in ungauged basins is bound to struggle with the estimation of all the soil parameters involved. In the proposed methodology, the soil depth input, which is very difficult to obtain at basin scale, is the most influencing parameter in terms of stability since the slope stability method assumes that the failure surface occurs precisely at the interface between the soil and the bedrock, which is given precisely by the input data. To address this issue which may impair the use of the model it is possible either to use empirical methods that try to correlate the soil depth with elevation or local slope (Catani et al. 2010), which still require calibration, or to use the thickness of the dynamic saturated layer provided by the hydrological model as the soil depth as reported in Rosso et al. (2006). At each time step of the simulation the stability of the slopes is verified assuming that the most critical shear surface occurs at the interface between the saturated and unsaturated zone, that is a key information provided by the hydrological model implemented. Lastly, to account for the spatial variability of the soil parameters, a Monte Carlo analysis can be done to understand the role of each individual parameter and to assess its importance on the resulting stability maps.

1.8 References

Arellano, D., Stark, T. D. (2000). Importance of three-dimensional slope stability in practice. Geotechnical Special Publication, 18-32, 10.1061/40512(289)2.

Baum, R. L. & Godt, J. W. (2010). Early warning of rainfall-induces shallow landslides and debris flows in the USA, Landslides, 7, 259-272, 10.1007/s10346-009-0177-0.

Baum, R. L., Savage W. Z., Godt. J. W. (2008). TRIGRS – a Fortran program for transient rainfall infiltration and grid-based regional slope-stability analysis, version 2.0, USGS.

Bellugi, D., Milledge, D. G., Dietrich, W. E., McKean, J. A., Perron, J. T., Sudderth, E. B., Kazian, B. (2015). A spectral clustering search algorithm for predicting shallow landslide size and location. Journal of Geophysical Research: Earth Surface, 120, 300-324.

Bellugi, D., Milledge, D., G., Cuffey, K., M., Dietrich, W. E., Larsen, L. G. (2021). Controls on the size distributions of shallow landslides. Proceedings of the National Academy of Sciences, 118, 9, 10.1073/pnas.2021855118.

Bishop, A. W. (1955). The use of the slip circle in the stability analysis of slopes, Geotechnique, Vol 5, No. 1, pp 7-17.

Burroughs, E. R. Jr. (1985). Landslide hazard rating for portions of the Oregon Coast range, Symposium on Effects of Forest Land Use on Erosion and Slope Stability, 265-274.

O'Callaghan, J. F., Mark, D., M. (1984). The extraction of drainage networks from digital elevation data, Computer Vision, Graphics and Image Processing, 28, 3, 323-344, 10.1016/S0734-189X(84)80011-0.

Casadei, M., Dietrich, W. E., Miller, N. L. (2003). Testing a model for predicting the timing and location of shallow landslide initiation in soil mantled landscapes. Earth Surface Processes and Landforms, 28 (9): 925-950.

Catani, F., Segoni, S., Falorni, G. (2010). An empirical geomorphology-based approach to the spatial prediction of soil thickness at catchment scale. Water Resources Research. 46. 10.1029/2008WR007450.

Chae, B., Lee, J. H., Park, H. J., Choi, J. (2015). A method for predicting the factor of safety of an infinite slope based on the depth ratio of the wetting front. Natural Hazards and Earth System Sciences Discussions. 3. 791-836. 10.5194/nhessd-3-791-2015.

Cho, S. E. (2017). Prediction of shallow landslide by superficial stability analysis considering rainfall infiltration, Engineering Geology, 231:126-138.

Cho, S. E., Lee, S. R. (2002). Evaluation of surficial stability for homogeneous slopes considering rainfall characteristics. Journal of Geotechnical and Geoenvironmental Engineering, 128 (9):756-763.

Chugh, A. K. (2003). On the boundary conditions in slope stability analysis. International Journal for Numerical and Analytical Methods in Geomechanics 27:905-926.

Cheng, Y. M., Lau, C. K. (2014). Slope stability analysis and stabilization, 2nd edition CRC press, 9780429166457.

Claessens, L., Heuvelink, G. B. M., Schoorl, J. M., Veldkamp, A. (2005). DEM resolution effects on shallow landslide hazard and soil redistribution modeling, Earth Surface Processes and Landforms, 30: 461-477.

D'Odorico, P., Fagherazzi, S., Rigon, R. (2005), Potential for landsliding: dependence on hyetograph characteristics, Journal of Geophysical Research, 110, F01007, doi:10.1029/2004JF000127.

Dietrich, W. E., Wilson, C. J., Montgomery, D. R., McKean, J., Bauer, R. (1992). Channelization thresholds and land surface morphology, Geology, v. 20, p. 675-679.

Dietrich, W. E., Wilson, C. J., Montgomery, D. R., McKean, J. (1993). Analysis of erosion thresholds, channel networks and landscape morphology using a digital terrain model, Journal of Geology, v. 101, p. 259-278.

Dietrich, W. E., Reiss, R., Hsu, M. L., Montgomery, D. R. (1995). A process-based model for colluvial soil depth and shallow landsliding using digital elevation data, Hydrological Processes, v. 9, p. 383-400.

Dietrich, W., McKean, J., Bellugi, D., Perron, T. (2008). The prediction of shallow landslide location and size using a multidimensional landslide analysis in a digital terrain model. Proceedings of International Conference on Debris-Flow Hazards Mitigation: Mechanics, Prediction, and Assessment.

Dietrich, W. E., Bellugi, D., Real de Asua, R. (2001). Validation of the shallow landslide model, SHALSTAB, for forest management. Land Use and Watersheds: Human Influence on Hydrology and Geomorphology in Urban and Forest Areas. 2. 195-227. 10.1029/WS002p0195.

Dolojan, N., Moriguchi, S., Hashimoto, M., Terada, K. (2021). Mapping method of rainfall-induced landslide hazards by infiltration and slope stability analysis, Landslides , 2039-2057, https://doi.org/10.1007/s10346-020-01617-x

Gabet, E. J., Dunne, T. (2002). Landslides on coastal sage-scrub and grassland hillslopes in a severe El Nino winter: the effects of vegetation conversion on sediment delivery. Geological Society of America Bulletin 114(8), 983-990.

GeoStudio (2021). Stability modeling with GeoStudio, reference manual by GEO-SLOPE.

Green, W. H., Ampt, G. A. (1911). Studies on soil physics, Journal of Agricultural Science, 4(1) 1-24.

Griffiths, D., V., Huang, J., deWolfe, G. F. (2011). Numerical and analytical observations on long and infinite slopes, International Journal for Numerical and Analytical Methods in Geomechanics 35: 569–585.

Guzzetti, F., Gariano, S. L., Peruccacci, S., Brunetti, M. T., Marchesini, I., Rossi, M., Melillo, M. (2020). Geographical landslide early warning systems, Earth-Science Reviews Vol. 200.

Haefeli, R. (1948). The stability of slopes acted upon by parallel seepage, International Conference on Soil Mechanics and Foundation Engineering, 57-62.

Heimsath, M. A., Dietrich, W. E., Nishiizumi, K., Finkel, R. C. (2001). Stochastic processes of soil production and transport: erosion rates, topographic variation and cosmogenic nuclides in the Oregon Coast Range, Earth Surface Processes and Landforms, 26, 5, 531-552, 10.1002/esp.209.

Hovland, H. J. (1977). Three-dimensional slope stability analysis method, ASCE Journal of the Geotechnical Engineering Division,103(GT9), 971-986.

Iida, T. (2004). Theoretical research on the relationship between return period of rainfall and shallow landslides, Hydrological Processes, 739–756.

Iverson, R. M. (2000). Landslide triggering by rain infiltration, Water Resources Research 36 (7) 1897-1910.

Janbu, N. (1973). Slope stability computations, Embankment Dam Engineering, Casagrande Volume, R.C. Hirschfeld and S.J. Poulos, eds., John Wiley and Sons, New York, pp 47-86.

Lehmann, P., Or, D. (2012). Hydromechanical triggering of landslides: from progressive local failures to mass release, Water Resources Research, 48, W03535.

Medina, V., Hürlimann, M., Guo, Z., Lloret, A., Vaunat, J. (2021). Fast physically-based model for rainfall-induced landslide susceptibility assessment at region scale. Catena, https://doi.org/10.1016/j.catena.2021.105213.

Megahan, W. F. (1983). Hydrologic effects of clearcutting and wildfire on steep granitic slopes of Idaho, Water Resources Research, 19, 811 – 819.

Metz, C. E. (1978). Basic principles of ROC analysis, Seminars in Nuclear Medicine, 8, 4, 10.1016/S0001-2998(78)80014-2.

Milledge, D. G., Griffiths, D., Lane, S. N., Warburton, J. (2012). Limits on the validity of infinite length assumptions for modelling shallow landslides. Earth surface processes and landforms, 37 (11). pp. 1158-1166.

Montgomery, D. R., Dietrich, W. E. (1994). A physically based model for the topographic control on shallow landsliding, Water Resources Research, 30, 1153-1171.

Montgomery, D. R., Schmidt, K. M., Dietrich, W. E., Greenberg, H. M. (2000). Forest clearing and regional landsliding in the Pacific Northwest, Geology, 28, 311-314.

Montgomery, D. R., Schmidt, K. M., Dietrich, W. E., McKean, J. (2009). Instrumental record of debris flow initiation during natural rainfall: Implications for modeling slope stability, Journal of Geophysical Research, 114, F01031, doi:10.1029/2008JF001078.

Montrasio, L., Valentino, R., Losi, G. L. (2011). Towards a real-time assessment of rainfall induced shallow landslides on a regional scale, Natural Hazards and Earth System Science, 11(7), 1927-1947.

Montrasio, L., Gatto, M. P. A., Miodini, C. (2023). The role of plants in the prevention of soil-slip: the G-SLIP model and its application on territorial scale through G-XSLIP platform, Landslides, 20, 1149-1165, 10.1007/s10346-023-02031-9.

Morgenstern, N. R., Price, V. E. (1965). The analysis of the stability of general slip surfaces, Geotechnique, Vol 15, No. 1, pp 79-93.

Murgia, I., Giadrossich, F., Mao, Z., Cohen, D., Capra, G. F., Schwarz, M. (2022). Modelling shallow landslides and root reinforcement: a review, Ecological Engineering, 181, https://doi.org/10.1016/j.ecoleng.2022.106671.

Oguz, E. A., Depina, I., Thakur, V. (2022). Effects of soil heterogeneity on susceptibility of shallow landslides, Landslides, 19, 67-83. 10.1007/s10346-021-01738-x

Okimura, T. (1994). Prediction of the shape of a shallow failure on a mountain slope: the three-dimensional multi-planar sliding surface method, Geomorphology, 9, 223-233.

Piciullo, L., Calvello, M., Cepeda, J. (2018). Territorial early warning systems for rainfall-induced landslides, Earth-Science Reviews, 228-247, doi:10.1016/j.earscirev.2018.02.013.

Pierson, T. C. (1977). Factors controlling debris flow initiation on forested hillslopes in the Oregon Coast Range, Ph.D. thesis, Univ. of Wash., Seattle.

Pilotti, M., Rosso, R. (1990). Shell: a general framework for modeling the distributed response of a drainage basin. Computational Methods in Surface Hydrology, Springer Verlag, 517-522.

Pilotti, M., Gandolfi, C., Bischetti G. B. (1996). Identification and analysis of natural channel networks from digital elevation models, Earth Surface Processes and Landforms, 21, 1007-1020.

Pilotti, M. Chapra S. C., Valerio, G. (2019). Steady-state distributed modeling of dissolved oxygen in data-poor, sewage dominated river systems using drainage networks, Environmental Modeling and Software, 111, 153-169.

Qiu, C. T., Esaki, T., Kie, M., Mitani, Y., Wang, C. (2007). Spatio-temporal estimation of shallow landslide hazard triggered by rainfall using a three-dimensional model, Environmental Geology 52(8), 1569-1579.

Roering, J. J., Kirchner, J. W., Dietrich, W. E. (1990). Evidence for nonlinear, diffusive sediment transport on hillslopes and implications for landscape morphology, Water Resources Research, 35, 3, 10.1029/1998WR900090.

Rosso, R., Rulli, M. C., Vannucchi, G. (2006). A physically based model for the hydrologic control on shallow landsliding, Water Resources Reseach, 42. 10.1029/2005WR004369.

Rossi, G., Catani, F., Leoni, L., Segoni, S., Tofani, V. (2013). HIRESSS: a physically based slope stability simulator for HPC applications. Natural Hazards and Earth System Sciences. 13, 151-166, 10.5194/nhess-13-151-2013.

Sidle, R., C., Swanston, D., N. (1982). Analysis of a small debris slide in costal Alaska, Canadian Geotechnical Journal, 19, 167–174.

Skempton, A. W., DeLory, F. A. (1957). Stability of natural slopes in London clay, 4th International Conference on Soil Mechanics and Foundation Engineering, 378-381.

Spencer, E. (1967). A method of analysis of the stability of embankments assuming parallel interslice forces, Geotechnique, Vol 17, No. 1, pp 11-26.

Taylor, D. W. (1948). Fundamentals of soil mechanics, Wiley, New York.

US Army Corps of Engineers (2003). Engineering and design slope stability, Washington DC.

Xie, M., Esaki, T., Cai, M. (2004). A time-space based approach for mapping rainfall-induced shallow landslide hazard, Environmental Geology. 46. 840-850. 10.1007/s00254-004-1069-1.

Chapter 2

A multi-rheological finite volume scheme on unstructured grid for debris flow propagation

2.1 Introduction

In steep mountain areas rapid mass movements such as avalanches and debris flows are surface processes which are characterized by large masses of granular material flowing at high speed (Takahashi, 2014). These processes may pose a serious threat whenever their path crosses populated areas, or damage key infrastructures like streets or railways. Accordingly, they deserve the highest attention. While multiple mitigation strategies are possible, their choice must be based on suitable physically based models and can't be done only using historical data, which inevitably are often missing or incomplete. Numerical methods describing the motion of granular material coupled with remote sensing are a viable alternative to properly assess run-off distance, velocity, flow and depositional height (Hergarten & Robl, 2015). Despite the work of many authors on the subject (e.g. Takahashi, 1978; Iverson 1997) a complete understanding about the main processes behind the propagation of debris flows is still missing. Debris flows are a flow of sediment and water mixture driven by gravity, and they attain large mobility from the enlarged void space saturated with water or slurry (Takahashi, 2014). From a mathematical point of view, mass and momentum balance are the physical laws used to model the dynamics of a debris flow (Trujillo-Vela et al., 2022) and in some cases it is important to consider the interaction with the flow boundary, where significative erosion and deposition can occur. Starting from one of the first attempts to model snow avalanches made by Voellmy (1955), which used a simplified momentum equation coupled with a custom rheological relationship, model complexity has been increasing proportionally to the understanding of the underlying governing processes. Latest contributions are three-dimensional and multiphase description of the phenomena as found in Leonardi et al. (2015), Pudasaini & Mergili (2019) and Rosatti & Begnudelli (2012). Despite the technical advancement provided by these implementations, which tends towards a complete model, in which both solid and liquid phases are considered, complexity, computational burdens and calibrating parameters scale accordingly. In principle the accurate description of the momentum of every single phase during the flow may lead to accurate results, assuming that adequate information about the initiation of the motion is available. This may require the knowledge, to the very least, of the volume of the event that may occur, an already difficult estimate to make considering that most debris flow occur unexpectedly and often in ungauged areas. Techniques to estimate the amount of material that may trigger a debris flow are described in the previous chapter, from which it is clear that a reliable estimate depends on a variety of parameters which need to be known (in theory) in every point of the catchment. An additional complexity of debris flows dynamics is the possibility to entrain or deposit sediments during the propagation of the flow which may alter momentum, mass, rheology and flow behaviour. The intricacies described, that may substantially affect the results if not properly considered, usually are solved by performing multiple simulations exploring a range of parameters and initial conditions with equal probability and then analysing the results to determine which areas are endangered by a certain

event. Such approach works reasonably well for hazard mapping but inevitably requires a mathematical model for the simulation with a relatively low computational time. In this framework, a shock-capturing, finite volume scheme which solves a modified formulation of the Shallow Water Equations (SWE) on unstructured grids has been developed and implemented. The model (in the following called DEBRA) will be described and validated in the following sections.

2.2 Governing equations

Debris flows are typically triggered either by the failure of saturated steep slopes or of mountain stream beds and can stop on slopes ranging from 5° to 10° or more. Accordingly, it is fundamental to properly account for the role of slope in the formulating equations, so the numerical model proposed in this thesis is based on a new formulation of the Shallow Water Equations (SWE), named Steep Slope Shallow Water Equations (SSSWE), following Maranzoni & Tomirotti (2022). The formulation is reported below for clarity.

$$\mathbf{U}_t + \mathbf{F}(\mathbf{U})_x + \mathbf{G}(\mathbf{U})_y = \mathbf{S}(\mathbf{U})$$

$$\mathbf{U} = \begin{bmatrix} h \\ hU \\ hV \end{bmatrix} \quad \mathbf{F}(\mathbf{U}) = \begin{bmatrix} hu\cos\vartheta_x \\ \left(uUh + \frac{1}{2}kgh^2\right)\cos\vartheta_x \\ huV\cos\vartheta_x \end{bmatrix} \quad \mathbf{G}(\mathbf{U}) = \begin{bmatrix} hv\cos\vartheta_y \\ hUv\cos\vartheta_y \\ \left(vVh + \frac{1}{2}kgh^2\right)\cos\vartheta_y \end{bmatrix} \qquad (2.1)$$

$$\mathbf{S}(\mathbf{U}) = \begin{bmatrix} 0 \\ -gh(S_{b\xi} + S_{f\xi}) \\ -gh(S_{b\eta} + S_{f\eta}) \end{bmatrix}$$

in which $\mathbf{U}$ is the vector of conserved variables (i.e. the vertical depth, h, measured along the direction of gravity, and the Uh and Vh unit discharges in the direction parallel to the bottom bed respectively), $\mathbf{F}$ and $\mathbf{G}$ are the vectors of physical fluxes, $\mathbf{S}$ is the source term, g is the gravity acceleration and k (≤ 1) is a pressure correction factor. The bottom slopes in the directions parallel to the bottom bed, i.e. ξ and η (see Figure 2.1) are given by

$$S_{b\xi} = \sin\vartheta_x \qquad S_{b\eta} = \sin\vartheta_y \qquad (2.2)$$

where ϑ_x and ϑ_y are the bottom slopes in the cartesian frame of reference (see again Figure 2.1) and finally in eq. (2.1) k is given by

$$k = \begin{cases} 1 & still\ water \\ \cos^2\psi = \frac{1}{1+\tan^2\vartheta_x+\tan^2\vartheta_y} & else \end{cases} \qquad (2.3)$$

which describes the effect of the bottom slope on vertical pressure distribution (Maranzoni & Tomirotti, 2022). In eq. (2.1) dependent unit discharges hU and hV are defined in terms of vertically averaged velocity components U and V but can also be expressed in terms of the velocity components u and v in the bottom oriented frame of reference (see Table 2.1 for a schematic view of the notation used).

$$u = \frac{U - V \sin\vartheta_x \sin\vartheta_y}{1 - \sin^2\vartheta_x \sin^2\vartheta_y} = \frac{U - V\cos\varphi}{\sin^2\varphi} \qquad v = \frac{V - U \sin\vartheta_x \sin\vartheta_y}{1 - \sin^2\vartheta_x \sin^2\vartheta_y} = \frac{V - U\cos\varphi}{\sin^2\varphi}$$
$$U = u + v \sin\vartheta_x \sin\vartheta_y = u + v\cos\varphi \qquad V = v + u \sin\vartheta_x \sin\vartheta_y = v + u\cos\varphi \tag{2.4}$$

where φ is the angle between local directions ξ and η, which are orthogonal only when $\vartheta_x = 0,\ \vartheta_y = 0$ or both.

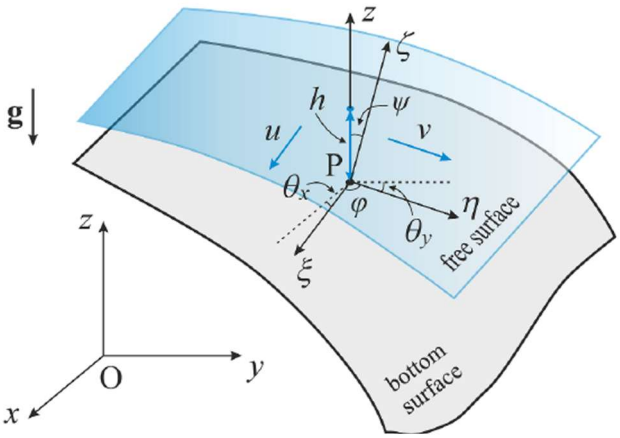

Figure 2.1 Definition sketch of the 3D free surface flow on steep bottom surface.

Variable	**Cartesian frame of reference (xyz)**	**Bottom oriented frame of reference ($\xi\eta z$)**
Velocity normal component	U	u
Velocity tangential component	V	v

Table 2.1 Schematic view of the notation for the fluid variables used in this thesis.

Although system (2.1) is closely related to the classical system of SWE, its properties and wave structure are an extension of the original system, as showed in the following. Following Toro (2001), consider the two dimensional x-split of the SSSWE

$$\begin{cases} \dfrac{\partial \mathbf{U}}{\partial t} + \dfrac{\partial \mathbf{F}(\mathbf{U})}{\partial x} = \mathbf{0} \\ \mathbf{U}(x,0) = \begin{cases} \mathbf{U}_L & x < 0 \\ \mathbf{U}_R & x > 0 \end{cases} \end{cases} \tag{2.5}$$
$$\mathbf{U}_L = \begin{bmatrix} h_L \\ h_L U_L \\ h_L V_L \end{bmatrix} \qquad \mathbf{U}_R = \begin{bmatrix} h_R \\ h_R U_R \\ h_R V_R \end{bmatrix}$$

where $\mathbf{U}_L, \mathbf{U}_R$ are the constant states of the problem and represent conditions at time $t = 0$ to the left and right of $x = 0$. As reported by Maranzoni & Tomirotti (2022) system (2.1) is strictly hyperbolic for $h \neq 0$ and the eigenvalues of (2.5) are given by

$$\lambda_1 = \left(U - V\cos\varphi - \sqrt{gkh}\sin\varphi\right)\frac{\cos\vartheta_x}{\sin^2\varphi}$$

$$\lambda_2 = (U - V\cos\varphi)\frac{\cos\vartheta_x}{\sin^2\varphi} \tag{2.6}$$

$$\lambda_3 = \left(U - V\cos\varphi + \sqrt{gkh}\sin\varphi\right)\frac{\cos\vartheta_x}{\sin^2\varphi}$$

Therefore, in the general case, three waves are originated in the Riemann problem described in (2.5). Considering classical SWE, characteristic fields associated with eigenvalues $\lambda_1(\mathbf{U})$ and $\lambda_3(\mathbf{U})$ are genuinely nonlinear, i.e. they generate either shocks or rarefactions, while the characteristic field associated with eigenvalue λ_2 is linearly degenerate, i.e. it generates a contact or a shear wave (Toro, 2001). In the following it will be shown that also the SSSWE preserve the same structure, behaving identically to the classical SWE. Recall that a characteristic field λ_i is said to be linearly degenerate if $\nabla\lambda_i \cdot \mathbf{R}^{(i)}(\mathbf{U}) = 0$ for any $\mathbf{U}$ and genuinely nonlinear if $\nabla\lambda_i \cdot \mathbf{R}^{(i)}(\mathbf{U}) \neq 0$, where $\nabla\lambda_i$ is the gradient of an eigenvalue $\lambda_i(\mathbf{U})$ given by

$$\nabla\lambda_i(\mathbf{U}) = \left[\frac{\partial}{\partial q_1}\lambda_i,\ \frac{\partial}{\partial q_2}\lambda_i,\ \frac{\partial}{\partial q_3}\lambda_i\right] \tag{2.7}$$

where q_1, q_2 and q_3 are the conserved variables of system (2.5) and $\mathbf{R}^{(i)}(\mathbf{U})$ is the corresponding eigenvector associated to the i-field. To show this, express system (2.1), where the source term has been neglected, in non-conservative formulation, by introducing the primitive variables h, U and V

$$\mathbf{W}_t + \mathbf{A}(\mathbf{W})\mathbf{W}_x + \mathbf{B}(\mathbf{W})\mathbf{W}_y = \mathbf{0}$$

$$\mathbf{W} = \begin{bmatrix} h \\ U \\ V \end{bmatrix} \quad \mathbf{A}(\mathbf{W}) = \begin{bmatrix} U - V\cos\varphi & h & -h\cos\varphi \\ gk\sin^2\varphi & U - V\cos\varphi & 0 \\ 0 & 0 & U - V\cos\varphi \end{bmatrix}\frac{\cos\vartheta_x}{\sin^2\varphi} \tag{2.8}$$

$$\mathbf{B}(\mathbf{W}) = \begin{bmatrix} V - U\cos\varphi & -h\cos\varphi & h \\ 0 & V - U\cos\varphi & 0 \\ gk\sin^2\varphi & 0 & V - U\cos\varphi \end{bmatrix}\frac{\cos\vartheta_y}{\sin^2\varphi}$$

Considering the matrix of right eigenvectors of $\mathbf{A}(\mathbf{W})$ leads to the following result

$$\mathbf{R} = \begin{bmatrix} h & 0 & h \\ -\sqrt{gkh}\sin\varphi & \cos\varphi & \sqrt{gkh}\sin\varphi \\ 0 & 1 & 0 \end{bmatrix} \tag{2.9}$$

Now express the eigenvalues reported in (2.6) in terms of the conserved variables $q_1 = h, q_2 = hU$ and $q_3 = hV$

$$\lambda_1 = \left(\frac{q_2}{q_1} - \frac{q_3}{q_1}\cos\varphi - \sqrt{gkq_1}\sin\varphi\right)\frac{\cos\vartheta_x}{\sin^2\varphi}$$
$$\lambda_2 = \left(\frac{q_2}{q_1} - \frac{q_3}{q_1}\cos\varphi\right)\frac{\cos\vartheta_x}{\sin^2\varphi} \tag{2.10}$$
$$\lambda_3 = \left(\frac{q_2}{q_1} - \frac{q_3}{q_1}\cos\varphi + \sqrt{gkq_1}\sin\varphi\right)\frac{\cos\vartheta_x}{\sin^2\varphi}$$

Simple calculations for the 1-wave (the wave associated with the first eigenvalue) and 3-wave (the wave associated with the third eigenvalue) show that

$$\nabla\lambda_1(\mathbf{U})\cdot\mathbf{R}^{(1)}(\mathbf{U}) =$$
$$\left[\left(-\frac{q_2}{q_1^2} + \frac{q_3}{q_1^2}\cos\varphi - \frac{\sqrt{gk}}{2\sqrt{q_1}}\sin\varphi\right)\frac{\cos\vartheta_x}{\sin^2\varphi},\ \frac{\cos\vartheta_x}{q_1\sin^2\varphi}, -\frac{\cos\varphi\cos\vartheta_x}{q_1\sin^2\varphi}\right]\cdot\begin{bmatrix} q_1 \\ -\sqrt{gkq_1}\sin\varphi \\ 0 \end{bmatrix} \neq 0 \tag{2.11}$$

$$\nabla\lambda_3(\mathbf{U})\cdot\mathbf{R}^{(3)}(\mathbf{U}) =$$
$$\left[\left(-\frac{q_2}{q_1^2} + \frac{q_3}{q_1^2}\cos\varphi + \frac{\sqrt{gk}}{2\sqrt{q_1}}\sin\varphi\right)\frac{\cos\vartheta_x}{\sin^2\varphi},\ \frac{\cos\vartheta_x}{q_1\sin^2\varphi}, -\frac{\cos\varphi\cos\vartheta_x}{q_1\sin^2\varphi}\right]\cdot\begin{bmatrix} q_1 \\ \sqrt{gkq_1}\sin\varphi \\ 0 \end{bmatrix} \neq 0$$

While for the 2-wave (the wave associated with the second eigenvalue)

$$\nabla\lambda_2(\mathbf{U})\cdot\mathbf{R}^{(2)}(\mathbf{U}) =$$
$$\left[\left(-\frac{q_2}{q_1^2} + \frac{q_3}{q_1^2}\cos\varphi\right)\frac{\cos\vartheta_x}{\sin^2\varphi},\ \frac{\cos\vartheta_x}{q_1\sin^2\varphi}, -\frac{\cos\varphi\cos\vartheta_x}{q_1\sin^2\varphi}\right]\cdot\begin{bmatrix} 0 \\ \cos\varphi \\ 1 \end{bmatrix} = 0 \tag{2.12}$$

Thus confirming that both the 1-wave and 3-wave are genuinely nonlinear while the 2-wave is linearly degenerate. From the solution of the Riemann problem (2.5) with constant initial data four possible wave patterns can emerge, as reported in Figure 2.2.

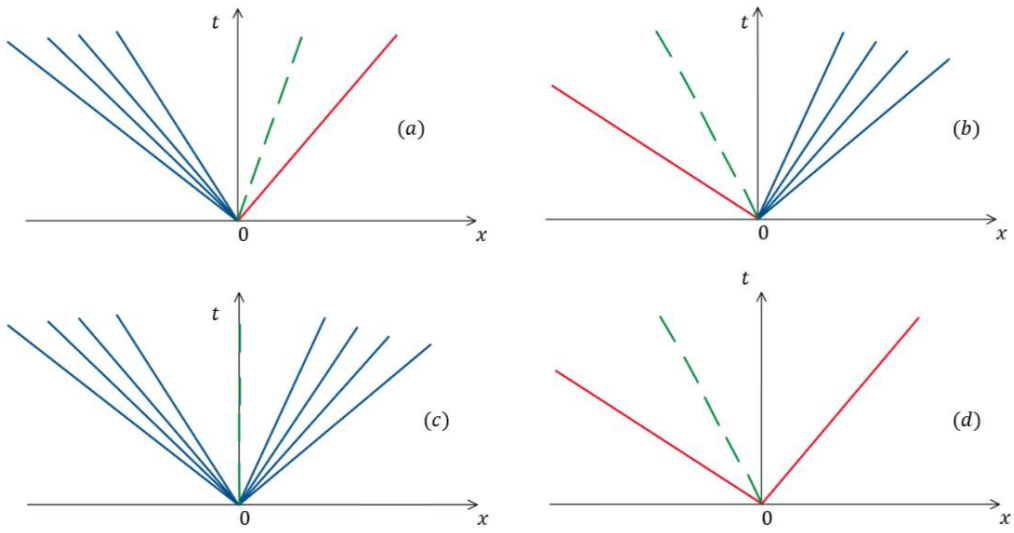

Figure 2.2 Possible wave patterns in the solution of the Riemann problem (2.5). Case a) left wave is a rarefaction while the right one is a shock. Case b) left wave is a shock and right one is a rarefaction. Case c) both waves are rarefactions. Case d) both waves are shocks. In each case three waves arise, the 1-wave and 3-wave are genuinely

non-linear and are either rarefaction or shock waves while the 2-wave is linearly degenerate and corresponds always to a shear wave.

In the following sections simple solutions of the Riemann problem (2.5) are investigated that originate from a particular choice of the initial data which create just a single wave. Any other possible wave is assumed to possess zero strength, i.e. it is absent from the wave structure. The bottom slopes ϑ_x and ϑ_y are assumed to be defined at the cell center of the left and right of the cell center, which are denoted with $\vartheta_{x,L}$ and $\vartheta_{x,R}$ considering the x direction only (similarly for the y direction).

2.2.1 Rarefaction waves

A rarefaction wave arises in the situation in which two data states are connected through a smooth transition in a genuinely non-linear wave (Toro, 2001). Figure 2.3 depicts the fan-like structure, centred at the origin. Rarefactions are associated with the genuinely non-linear waves and satisfy: the constancy of generalized Riemann invariants and the divergence of characteristics (Toro, 2001).

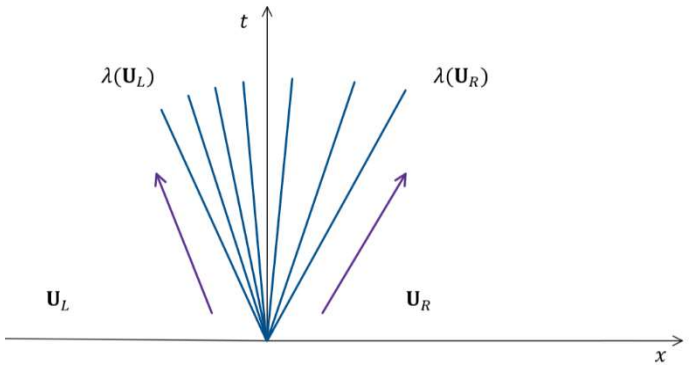

Figure 2.3 Single wave solution of the Riemann problem is a rarefaction wave. $\lambda(\mathbf{U}_L)$ and $\lambda(\mathbf{U}_R)$ are the eigenvalues corresponding to the states $\mathbf{U}_L$ and $\mathbf{U}_R$.

The divergence of characteristics states that $\lambda_i(\mathbf{U}_L) < \lambda_i(\mathbf{U}_R)$, meaning that the corresponding eigenvalue increases monotonically as the wave is crossed from left to right, this follows from the hyperbolicity of system (2.1). On the other hand generalized Riemann invariants are relations that hold true across rarefactions and lead to the following $m - 1$ differential equations of the form

$$\frac{dW_1}{r_1^{(i)}} = \frac{dW_2}{r_2^{(i)}} = \cdots = \frac{dW_m}{r_m^{(i)}} \tag{2.13}$$

that relate ratios of changes dW_s of a quantity W_s to the respective component $r_s^{(i)}$ of the right eigenvector $\mathbf{R}^{(i)}$, as reported by Toro (2001). System (2.1) possesses Riemann invariants that can be seen as an extension of the Riemann invariants of the classical SWE. Applying eq. (2.13) to the third column of matrix $\mathbf{R}$ reported in eq. (2.9), thus considering a right rarefaction, leads to

$$\frac{dh}{h} = \frac{dU}{\sqrt{gkh}\sin\varphi} = \frac{dV}{0} \tag{2.14}$$

The third ratio implies $dV = 0$ and thus V is constant across the wave, while the first equality implies

$$\frac{dU}{\sqrt{gk}\sin\varphi} - h^{-1/2}dh = 0 \tag{2.15}$$

which can be integrated in the phase space obtaining that the quantity $U - 2\sqrt{gkh}\sin\varphi$ is constant across the rarefaction. As it can be noticed, the quantity $U - 2\sqrt{gkh}\sin\varphi$ reduces to $U - 2\sqrt{gh}$ in presence of negligible slopes ($\sin\varphi \approx 1, k = 1$). The first column of matrix **R** leads to a similar result, i.e. $U + 2\sqrt{gkh}\sin\varphi$ is constant across the wave if one considers a left rarefaction.

2.2.2 Shear waves

Shear waves are discontinuous solutions associated with a linearly degenerate field, i.e. the 2-wave. Interestingly, application of the Riemann invariants equations (2.13) across the 2-wave leads to

$$\frac{dh}{0} = \frac{dU}{\cos\varphi} = \frac{dV}{1} \tag{2.16}$$

The first ratio simply tells that h is constant across the shear wave, as expected, while the last equality tells that

$$dU - dV\cos\varphi = 0 \tag{2.17}$$

By integrating eq. (2.17) one obtains that the quantity $U - V\cos\varphi$ is constant across the middle wave, meaning that both velocity components in the cartesian frame of reference exhibit a jump across the shear wave, contrary to the classical SWE in which just the tangential velocity component changes abruptly.

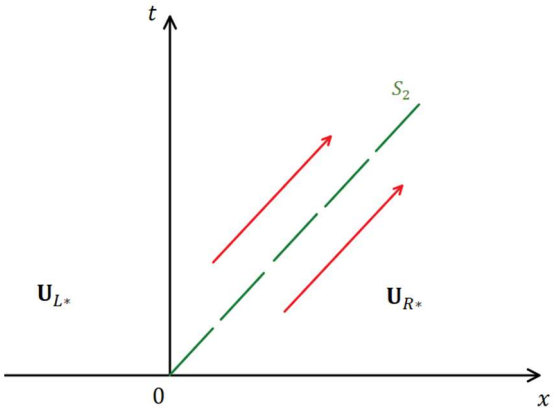

Figure 2.4 Single wave solution of the Riemann problem is a shear wave. Characteristics are parallel on both sides of the discontinuity.

2.2.3 Shock waves

The solution of the Riemann problem (2.5) made by two constant data states $\mathbf{U}_L$ and $\mathbf{U}_R$ is made up by a single shock wave of speed S_i, as showed in Figure 2.5. As reported by Toro (2001) the two data states are connected through a single jump discontinuity in a genuinely nonlinear field. Across the shock Riemann invariants equations are no longer valid but the Rankine-Hugoniot jump conditions apply (Leveque, 2002)

$$\mathbf{F}(\mathbf{U}_R) - \mathbf{F}(\mathbf{U}_L) = S_i(\mathbf{U}_R - \mathbf{U}_L) \tag{2.18}$$

Furthermore, the compressive character of the shock reflects the physical solution to be selected among the several weak solutions which are possible in case of a discontinuity in the solution. In particular the entropy condition (Leveque, 2002) stating that

$$\lambda_i(\mathbf{U}_L) > S_i > \lambda_i(\mathbf{U}_R) \tag{2.19}$$

holds for the shock wave assumed for the problem.

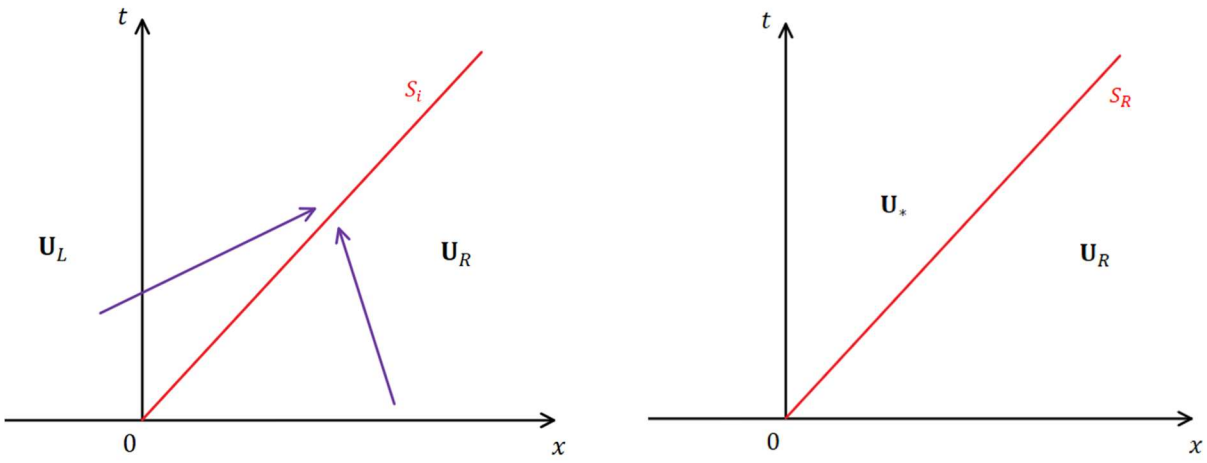

Figure 2.5 (Left) Single wave solution of the Riemann problem is a shock wave, characteristics ahead and behind the shock wave merge into the shock path in agreement with the entropy condition (2.19). (Right) Solution of the Riemann problem is an isolated right shock wave.

To study shock waves it is crucial to enforce the conservative formulation of the equations to apply the Rankine-Hugoniot conditions (2.18). However, it is possible to express the initial states in terms of the primitive variables, the left and right states are given by

$$\mathbf{W}_* = \begin{bmatrix} h_* \\ U_* \\ V_* \end{bmatrix} \qquad \mathbf{W}_R = \begin{bmatrix} h_R \\ U_R \\ V_R \end{bmatrix} \tag{2.20}$$

where a right shock is assumed to occur, i.e. $S_i = S_R$. As proposed by Toro (2001), to simplify computations, the variables are transformed in a frame of reference moving with the shock speed S_R.

$$\begin{aligned} \widehat{U}_* &= U_* - S_R \quad \widehat{U}_R = U_R - S_R \\ \widehat{V}_* &= V_* - S_R \quad \widehat{V}_R = V_R - S_R \end{aligned} \tag{2.21}$$

Therefore the Rankine-Hugoniot jump conditions (2.18) states

$$\begin{gathered} \left(\widehat{U}_R h_R - \widehat{V}_R h_R \cos\varphi_R\right)\frac{\cos\vartheta_{x,R}}{\sin^2\varphi_R} - \left(\widehat{U}_* h_* - \widehat{V}_* h_* \cos\varphi_R\right)\frac{\cos\vartheta_{x,R}}{\sin^2\varphi_R} = 0 \\ \left(\widehat{U}_R^2 h_R - \widehat{U}_R\widehat{V}_R h_R \cos\varphi_R + \frac{1}{2}g k_R h_R^2 \sin^2\varphi_R\right)\frac{\cos\vartheta_{x,R}}{\sin^2\varphi_R} - \left(\widehat{U}_*^2 h_* - \widehat{U}_*\widehat{V}_* h_* \cos\varphi_* + \frac{1}{2}g k_* h_*^2 \sin^2\varphi_*\right)\frac{\cos\vartheta_{x,*}}{\sin^2\varphi_*} = 0 \\ \left(\widehat{U}_R\widehat{V}_R h_R - \widehat{V}_R^2 h_R \cos\varphi_R\right)\frac{\cos\vartheta_{x,R}}{\sin^2\varphi_R} - \left(\widehat{U}_*\widehat{V}_* h_* - \widehat{V}_*^2 h_* \cos\varphi_*\right)\frac{\cos\vartheta_{x,*}}{\sin^2\varphi_*} = 0 \end{gathered} \tag{2.22}$$

In principle, the system made by (2.21) and (2.22) has 8 unknowns, i.e. $\widehat{U}_*, U_*, \widehat{U}_R, \widehat{V}_*, V_*, \widehat{V}_R, S_R, h_*$ (assuming $\vartheta_{x,*}$and $\vartheta_{y,*}$ known using some simple criteria, see the next sections) and 7 equations, meaning that it is possible to write the unknown shock speed S_R in terms of one other unknowns, i.e. h_* (see the next section to understand the reason behind this choice). Despite being possible, the resulting expression is highly complicated and tedious to write in compact form due to the presence of different trigonometric functions inside eq. (2.22). Having in mind straightforwardness, it has been set $\varphi_R = \varphi_* = \varphi$ and $\cos\vartheta_{x,R} = \cos\vartheta_{x,*} = \cos\vartheta_x$, which physically corresponds to a constant bottom slope present between the states, which is not always the case. Therefore the following shock speed will be an estimate where the states are separated by a slope which is not constant, or the true shock speed if they are. Rewriting eq. (2.22)

$$\begin{gathered} \left(\widehat{U}_R h_R - \widehat{V}_R h_R \cos\varphi\right)\frac{\cos\vartheta_x}{\sin^2\varphi} - \left(\widehat{U}_* h_* - \widehat{V}_* h_* \cos\varphi\right)\frac{\cos\vartheta_x}{\sin^2\varphi} = 0 \\ \left(\widehat{U}_R^2 h_R - \widehat{U}_R\widehat{V}_R h_R \cos\varphi + \frac{1}{2}g k h_R^2 \sin^2\varphi\right)\frac{\cos\vartheta_x}{\sin^2\varphi} - \left(\widehat{U}_*^2 h_* - \widehat{U}_*\widehat{V}_* h_* \cos\varphi + \frac{1}{2}g k h_*^2 \sin^2\varphi\right)\frac{\cos\vartheta_x}{\sin^2\varphi} = 0 \\ \left(\widehat{U}_R\widehat{V}_R h_R - \widehat{V}_R^2 h_R \cos\varphi\right)\frac{\cos\vartheta_x}{\sin^2\varphi} - \left(\widehat{U}_*\widehat{V}_* h_* - \widehat{V}_*^2 h_* \cos\varphi\right)\frac{\cos\vartheta_x}{\sin^2\varphi} = 0 \end{gathered} \tag{2.23}$$

From the first and last equation of (2.23) follows that $\widehat{V}_R = \widehat{V}_*$, meaning that the tangential velocity component remains constant across the right shock wave. It is useful to define a parameter M_R in terms also of the projected velocities given by eq. (2.4)

$$M_R = -\left(\widehat{U}_R h_R - \widehat{V}_R h_R \cos\varphi\right)\frac{\cos\vartheta_x}{\sin^2\varphi} = -h_R \hat{u}_R \cos\vartheta_x = -h_* \hat{u}_* \cos\vartheta_x \tag{2.24}$$

Combining the second equation reported in (2.23) with (2.24) leads to

$$M_R\left(\widehat{U}_R - \widehat{U}_*\right) = \frac{1}{2}g k (h_*^2 - h_R^2)\cos\vartheta_x \tag{2.25}$$

On the other hand using eq. (2.23)

$$\hat{u}_* = -\frac{M_R}{h_* \cos\vartheta_x} \qquad \hat{u}_R = -\frac{M_R}{h_R \cos\vartheta_x} \tag{2.26}$$

and considering that

$$\widehat{U}_R - \widehat{U}_* = (\hat{u}_R - \hat{u}_*)(1 + \cos^2 \varphi) \tag{2.27}$$

where the relation $\widehat{V}_R = \widehat{V}_*$ has been used to obtain (2.27). Then by substituting (2.26) and (2.27) into (2.25) it is possible to write

$$M_R = \sqrt{\frac{gk(h_* + h_R)h_* h_R}{2(1 + \cos^2 \varphi)}} \cos \vartheta_x \tag{2.28}$$

Lastly, by suitably manipulating eq. (2.21) one obtains

$$S_R = (u_R - \hat{u}_R)(1 + \cos \varphi) \tag{2.29}$$

which can be used, together with eq. (2.25) and eq. (2.29), to compute the unknown shock speed

$$S_R = \left(\frac{U_R - V_R \cos \varphi}{\sin^2 \varphi} + \sqrt{\frac{gk(h_* + h_R)h_*}{2(1 + \cos^2 \varphi)h_R}} \right)(1 + \cos \varphi) \tag{2.30}$$

Similar computations can be performed to obtain the relation for S_L, the left facing shock.

2.3 Numerical scheme

The following numerical scheme is an adaptation of the works of Bonomelli et al. (2023) to the new SWE formulation. The entire computational domain Ω is divided into N triangular shaped control volumes K_i. The vector of conserved variables $\mathbf{U}$ is computed at the centre of gravity of each element, thus defining a cell-centred discretization. Using an explicit Euler scheme and denoting the current time step as $t^n = n\,\Delta t$, system (2.1) can be approximated as

$$\begin{aligned} \mathbf{U}_i^{n+1} &= \mathbf{U}_i^n - \frac{\Delta t}{A_i} \sum_{j=1}^{m} \mathbf{H}(\mathbf{U}) \cdot \boldsymbol{n}_{ij} L_{ij} + \Delta t\, \mathbf{S}_i \\ \mathbf{U}_i &= \frac{1}{A_i} \int_{K_i} \mathbf{U}(\boldsymbol{x}, t^n)\, d\boldsymbol{x} \\ \mathbf{S}_i^n &= \frac{1}{A_i \Delta t} \int_{t^n}^{t^n + \Delta t} \int_{K_i} \mathbf{S}(\mathbf{U}_i(\boldsymbol{x}, t)) d\boldsymbol{x}\, dt \end{aligned} \tag{2.31}$$

where L_{ij} is the j side of the i cell, which is characterized by a normal vector $\boldsymbol{n}_{ij}$, while A_i is the area along the bottom bed of the cell considered. Eq. (2.31) is obtained by the integration of system (2.1) in the $(\boldsymbol{x} - t)$ space, i.e. $V = K_i \times [t^n, t^{n+1}]$. Furthermore $\mathbf{U}_i^n$ is the averaged spatial integral of the solution at time t^n and $\mathbf{S}_i$ is the volume integral average in V of the source term vector. To compute the intercell fluxes $\mathbf{H}(\mathbf{U}) = [\mathbf{F}(\mathbf{U})\ \mathbf{G}(\mathbf{U})]$ needed to update the

conserved variables on the triangular grid one can exploit the rotational invariance property of the system, still valid in this formulation of the SSSWE (Maranzoni & Tomirotti, 2022), between $\mathbf{F}$ and $\mathbf{G}$ over each side, which states

$$\mathbf{H}(\mathbf{U}) \cdot \boldsymbol{n}_{ij} = \mathbf{T}_{n_{ij}}^{-1} \mathbf{F}\left(\mathbf{T}_{n_{ij}} \mathbf{U}\right)$$
$$\mathbf{T}_{n_{ij}} = \begin{bmatrix} 1 & 0 & 0 \\ 0 & n_{ij}(1) & n_{ij}(2) \\ 0 & -n_{ij}(2) & n_{ij}(1) \end{bmatrix} \tag{2.32}$$

Meaning that the computation of the fluxes reduces to a local 1D problem over each side

$$\mathbf{U}_i^{n+1} = \mathbf{U}_i^n - \frac{\Delta t}{A_i} \sum_{j=1}^{m} \mathbf{T}_{n_{ij}}^{-1} \tilde{\mathbf{F}}\left(\mathbf{T}_{n_{ij}} \mathbf{U}_i, \mathbf{T}_{n_{ij}} \mathbf{U}_j\right) L_{ij} + \Delta t \, \mathbf{S}_i \tag{2.33}$$

with $\tilde{\mathbf{F}}\left(\mathbf{T}_{n_{ij}} \mathbf{U}_i, \mathbf{T}_{n_{ij}} \mathbf{U}_j\right) = \tilde{\mathbf{F}}(\mathbf{U}_L, \mathbf{U}_R)$ being a discrete flux resolved using an exact or approximate solver of the Riemann problem having $\mathbf{U}_L$ and $\mathbf{U}_R$ as left and right initial states

$$\begin{cases} \dfrac{\partial \mathbf{U}}{\partial t} + \dfrac{\partial \mathbf{F}(\mathbf{U})}{\partial x_n} = \mathbf{0} \\ \mathbf{U}(x, 0) = \begin{cases} \mathbf{U}_L & x_n < 0 \\ \mathbf{U}_R & x_n > 0 \end{cases} \end{cases} \tag{2.34}$$

The application of the finite volume method requires a way to determine the numerical flux $\mathbf{F}(\mathbf{U})$ and the numerical source term $\mathbf{S}_i$. In this approach the numerical flux is computed using the Weighted Averaged Flux (WAF) approximation applied to a HLLC-type flux (Toro, 2001). The WAF method was first proposed by Toro (2001), it ensures a second order of accuracy in time and space, without data reconstruction as customary for other well-known methods like the MUSCL method (Leer, 1979). Although several versions of the WAF method are available (Ata et al., 2013), the original formulation is chosen for this implementation, which is a weighted sum of the fluxes in all the regions arising in the solution of the piecewise constant data Riemann problem (see Figure 2.6), namely

$$\mathbf{F}_{i+1/2} = \frac{1}{\Delta x} \int_{-\frac{\Delta x}{2}}^{\frac{\Delta x}{2}} \mathbf{F}\left(\mathbf{U}_{i+1/2}\left(x, \frac{\Delta t}{2}\right)\right) dx \tag{2.35}$$

where $\mathbf{U}_{i+1/2}(x, t)$ is the solution of the Riemann problem reported in (2.34) with $\mathbf{U}_L = \mathbf{U}_i^n$ and $\mathbf{U}_R = \mathbf{U}_{i+1}^n$. The state $\mathbf{U}_{i+1/2}$ can be computed by using either an exact or approximate Riemann solver. Exact Riemann solvers may be used to obtain Godunov-like methods (Leveque, 2002) which are first order of accuracy (Toro, 2001) and computationally expensive due to the requirement of a root searching algorithm, i.e. Newton's method, to compute the states required to evaluate the fluxes. Approximate Riemann solvers on the other hand are proved to be efficient (Leveque, 2002), and, if they are complete, i.e. they consider all regions in the Riemann diagram (see Figure 2.6), may provide an interesting alternative to exact Riemann solvers in numerical

applications. Here it is considered the HLLC Riemann solver (Toro, 2009), widely used in the literature for its simplicity and numerical robustness.

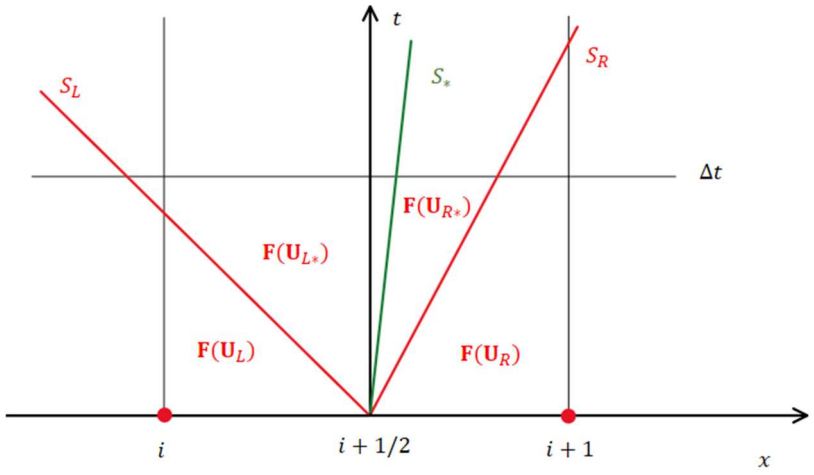

Figure 2.6 WAF diagram corresponding to the one dimensional Riemann problem between cell i (also referred as state L) and $i+1$ (state R). The region between S_L and S_R is called the star region.

With reference to Figure 2.6, there are two distinct fluxes in the region which arise from the interface, namely $\mathbf{U}_{L*}$ and $\mathbf{U}_{R*}$. The HLLC flux (Toro, 2019) can be written as

$$\mathbf{F}_{i+1/2}^{\mathrm{HLLC}}(\mathbf{U}_L,\mathbf{U}_R)=\begin{cases}\mathbf{F}_L=\mathbf{F}(\mathbf{U}_L) & 0\le S_L\\ \mathbf{F}_{L*}=\mathbf{F}_L+S_L(\mathbf{U}_{L*}-\mathbf{U}_L) & S_L\le 0\le S_*\\ \mathbf{F}_{R*}=\mathbf{F}_R+S_R(\mathbf{U}_{R*}-\mathbf{U}_R) & S_*\le 0\le S_R\\ \mathbf{F}_R=\mathbf{F}(\mathbf{U}_R) & 0\ge S_R\end{cases} \tag{2.36}$$

where S_* is the speed of the middle wave, still to be computed. A possible way to accomplish this task is to apply the Rankine Hugoniot jump conditions across the 1-wave and the 3-wave, and remembering that $h_{L*}=h_{R*}=h_*$, $u_{L*}=u_{R*}=u_*$, $V_L=V_{L*}$ and $V_R=V_{R*}$ due to the Riemann invariants equations reported in (2.13) together with the reasonable assumption that $\varphi_{L*}=\varphi_{R*}$

$$\begin{aligned}h_*u_*\cos\vartheta_{x,*}&=h_Lu_L\cos\vartheta_{x,L}+S_L(h_*-h_L)\\ h_*u_*\cos\vartheta_{x,*}&=h_Ru_R\cos\vartheta_{x,R}+S_R(h_*-h_R)\end{aligned} \tag{2.37}$$

Combining the equations above allows the following relation for the speed of the middle wave in terms of the assumed outer wave speed estimates S_L and S_R

$$S_*=u_*\cos\vartheta_x=\frac{S_Lh_R\left(u_R\cos\vartheta_{x,R}-S_R\right)-S_Rh_L(u_L\cos\vartheta_{x,L}-S_L)}{h_R\left(u_R\cos\vartheta_{x,R}-S_R\right)-h_L\left(u_L\cos\vartheta_{x,L}-S_L\right)} \tag{2.38}$$

Lastly, from the condition $u_{L*}=u_{R*}$ it is possible to write

$$U_{L*} = u_* \sin^2 \varphi_* + V_L \cos \varphi_*$$
$$U_{R*} = u_* \sin^2 \varphi_* + V_R \cos \varphi_* \tag{2.39}$$

To facilitate the implementation of the HLLC solver to the SSSWE the following summary is presented.

1. Given the states $\mathbf{U}_L$ and $\mathbf{U}_R$ one can compute an estimate of the water depth in the star region using the two rarefaction solution suggested by Toro (2019) adapted to the SSSWE which follows from the application of the Riemann invariants reported in eq. (2.15) assuming that both waves are rarefactions

$$\bar{h}_* = \frac{1}{g k_*} \left\{ \frac{1}{4} \left[U_L - U_R + \cos \varphi_* \, (V_R - V_L) + 2\sqrt{g k_L h_L} \sin \varphi_L + 2\sqrt{g k_R h_R} \sin \varphi_R \right] \right\}^2 \tag{2.40}$$

2. Compute the wave estimates S_L and S_R

$$S_L = \begin{cases} \left(\dfrac{U_L - V_L \cos \varphi_L}{\sin^2 \varphi_L} - \sqrt{\dfrac{g k_L (h_* + h_L) h_*}{2(1 + \cos^2 \varphi_L) h_L}} \right) (1 + \cos \varphi_L), & \bar{h}_* > h_L \\ \left(U_L - V_L \cos \varphi_L - \sqrt{g k_L h_L} \sin \varphi_L \right) \dfrac{\cos \vartheta_{x,L}}{\sin^2 \varphi_L}, & \bar{h}_* < h_L \end{cases} \tag{2.41}$$

$$S_R = \begin{cases} \left(\dfrac{U_R - V_R \cos \varphi_R}{\sin^2 \varphi_R} + \sqrt{\dfrac{g k_R (h_* + h_R) h_*}{2(1 + \cos^2 \varphi_R) h_R}} \right) (1 + \cos \varphi_R), & \bar{h}_* > h_R \\ \left(U_R - V_R \cos \varphi_R + \sqrt{g k_R h_R} \sin \varphi_R \right) \dfrac{\cos \vartheta_{x,R}}{\sin^2 \varphi_R}, & \bar{h}_* < h_R \end{cases}$$

3. Compute the middle wave speed using (2.38)
4. Compute the states in the star region using eq. (2.39) as

$$\mathbf{U}_{L*} = \begin{bmatrix} h_* \\ h_* U_{L*} \\ h_* V_L \end{bmatrix} \qquad \mathbf{U}_{R*} = \begin{bmatrix} h_* \\ h_* U_{R*} \\ h_* V_R \end{bmatrix} \tag{2.42}$$

5. Compute the HLLC flux according to eq. (2.36)

System (2.1) is strictly hyperbolic for a wet bed (Maranzoni & Tomirotti, 2022), but dry bed situations may arise and the wave speeds need to be adapted accordingly. Shock waves cannot be adjacent to a region of dry bed (Toro, 2001), therefore wet/dry discontinuities are characterized by a contact discontinuity, which continues to hold also for the SSSWE. This can be proven easily considering a Riemann problem (2.5) with data

$$\mathbf{W}_L = \begin{bmatrix} h_L \\ U_L \\ 0 \end{bmatrix} \qquad \mathbf{W}_R = \mathbf{W}_0 = \begin{bmatrix} h_0 \\ U_0 \\ 0 \end{bmatrix} \tag{2.43}$$

such that $\mathbf{W}_L$ is the data for a wet bed portion ($h_L > 0$) and $\mathbf{W}_0$ is the data for the dry bed portion, i.e. $h_0 = 0$ and U_0 is arbitrary. Suppose that $\mathbf{W}_L$ and $\mathbf{W}_0$ are connected by a shock wave of speed S. Using Rankine-Hugoniot conditions with $h_0 = 0$ gives

$$\begin{aligned} h_L u_L \cos\vartheta_{x,L} &= S\, h_L \\ \left(h_L u_L U_L + \frac{1}{2} g k_L h_L^2\right) \cos\vartheta_{x,L} &= S\, h_L U_L \end{aligned} \tag{2.44}$$

The first equation in (2.44) just states that $S = h_L u_L \cos\vartheta_{x,L}$ which, if substituted into the second equation in (2.44) gives $h_L = 0$. This last result is in contradiction with the original assumption of a wet left bed, i.e. $h_L > 0$, thus proving that shocks cannot be adjacent to a region of dry bed. To find the wave speed S in presence of a dry bed one can simply apply the Riemann Invariant across the correct wave, following Toro (2001). Considering a case in which the dry bed is on the right leads

$$U_0 + 2\sqrt{g k_0 h_0}\sin\varphi_0 = U_L + 2\sqrt{g k_L h_L}\sin\varphi \tag{2.45}$$

Therefore the speed of the contact discontinuity is

$$S_{dry} = U_0 = U_L + 2\sqrt{g k_L h_L}\sin\varphi_L \tag{2.46}$$

A brief summary on the conditions enforced in case of left or right dry bed are reported below for clarity

$$\begin{aligned} h_L = 0{:}\;\; S_L &= U_L - 2\sqrt{g k_L h_L}\sin\varphi_L\,; \quad S_* = S_L \\ h_R = 0{:}\;\; S_R &= U_R + 2\sqrt{g k_R h_R}\sin\varphi_R\,; \quad S_* = S_R \end{aligned} \tag{2.47}$$

Eq. (2.40) requires a way to assign a value for the slope at the interface between the cells (see Figure 2.7), which in general will be different (along the x direction) from either $\vartheta_{x,L}$ and $\vartheta_{x,R}$. To ensure flux consistency (Maranzoni & Tomirotti, 2023), the following choice has been adopted throughout the thesis

$$\begin{aligned} \vartheta_{x,*} &= \frac{1}{2}\left(\vartheta_{x,L}, +\vartheta_{x,R}\right) \\ \vartheta_{y,*} &= \frac{1}{2}\left(\vartheta_{y,L} + \vartheta_{y,R}\right) \end{aligned} \tag{2.48}$$

which provided good numerical results.

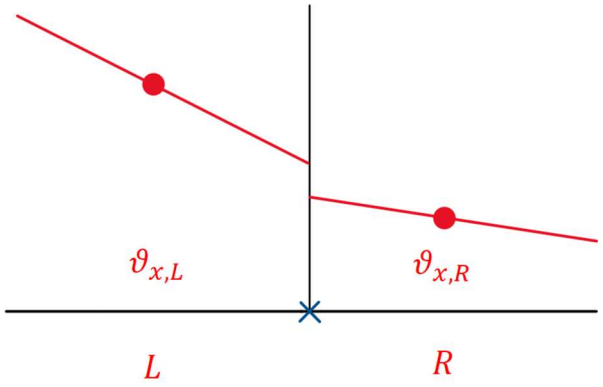

Figure 2.7 Schematics of the slopes for the x-split of the SSSWE.

The WAF scheme, being second-order accurate in space and time, produces spurious oscillations near steep gradients in the conserved variables (Loukili & Soulaimani, 2007). To suppress the unphysical oscillations while preserving the order of accuracy, a Total Variation Diminishing (TVD) nonlinear modification is enforced into the scheme (Toro, 2009). Enforcing this adaptation into the scheme requires a wider spatial numerical stencil, i.e. the numerical flux now depends not only on the states present between the two cells considered ($\mathbf{U}_L$ and $\mathbf{U}_R$) but also on some upwinding cells necessary to suppress oscillations, which will be defined as $\mathbf{U}_{LL}$ and $\mathbf{U}_{RR}$. The approach described by Loukili & Soulaimani (2007) has been implemented in which the upwind state variables are calculated using the neighbouring volumes. Wet and dry fronts are handled by introducing a cutoff threshold of $10^{-5}\ m$ on the water depth to avoid unphysical velocities or instabilities. Boundary conditions are implemented by inserting ad hoc states corresponding to the type of boundary being modelled on the basis of the theory of characteristics (Hou et al., 2013; Yoon et al., 2004). The approach implemented in the current numerical scheme is the one followed by Hou et al. (2013) according to which solid wall or open boundary conditions can be imposed. Lastly a second order accurate Strang splitting decomposition of the friction source term is adopted (Toro, 2001; Maranzoni & Tomirotti, 2023) which is made by three consecutive steps

$$\mathbf{U}_i^* = \mathbf{U}_i^n + \frac{\Delta t}{2}\mathbf{S}_f(\mathbf{U}_i^n)$$

$$\mathbf{U}_i^{**} = \mathbf{U}_i^* - \frac{\Delta t}{A_i}\sum_{j=1}^{m}\mathbf{T}_{n_{ij}}^{-1}\tilde{\mathbf{F}}\left(\mathbf{T}_{n_{ij}}\mathbf{U}_i^*, \mathbf{T}_{n_{ij}}\mathbf{U}_j^*\right)L_{ij} + \Delta t\,\mathbf{S}_b(\mathbf{U}_i^*) \tag{2.49}$$

$$\mathbf{U}_i^{n+1} = \mathbf{U}_i^{**} + \frac{\Delta t}{2}\mathbf{S}_f(\mathbf{U}_i^{**})$$

In the first step of the procedure, the friction source term is computed using the solution at the current time step n and evolved using a half time step to compute the first intermediate step $\mathbf{U}_i^*$. In the second step the solution is updated applying both advection and the bottom slope source term $\mathbf{S}_b$ to the previously computed intermediate state $\mathbf{U}_i^*$. Lastly, the solution is evolved over a half time step following the same procedure reported in step one, using this time the updated state obtained from the second step. Despite higher computational times, this procedure was selected for its simplicity in implementation, stability and its independence from the kind of friction term $\mathbf{S}_f$ used to describe the fluid. Lastly, modelling non-Newtonian fluids requires a

way to distinguish if the flow is in motion or it has stopped. Contrary to water, which stops once it has reached a flat surface only, non-Newtonian fluid can stop once they rest on a slope which is milder than its internal friction angle. However, the motion can start again because of its surrounding activity (Medina et al., 2008), so a simple check on the velocity or on the angle on which the flow is propagating would lead to inaccuracies. RAMMS (Christen et al., 2010) uses two criteria to detect whether a debris flow can be considered still across the domain, one based on the percentage of total momentum and the other one based on the center of mass of the flow. In the first one the momentum of all grid cells is computed at each time step and the maximum value encountered along the simulation is stored and compared with the current summation of the momentum of all grid cells. If the ratio between these two quantities (current momentum sum over maximum momentum sum) is below a certain threshold then the flow can be considered stopped. However, in practise, this approach requires to perform multiple simulations to calibrate this threshold: a threshold too low and the flow exhibits creeping behaviour and diffusion, and a threshold too high may stop prematurely the results. The second one tracks the position of the Center Of Mass (COM) of the debris flow and stops the flow when the velocity of the COM is below a certain threshold defined by the user. However, this approach makes sense only if a single release is considered in the domain. In DEBRA the momentum threshold used in RAMMS has been implemented and its application yielded similar stopping times when compared with RAMMS. Finally DEBRA is coded entirely inside the Matlab environment, which is very convenient for data handling and visualization purposes. However, as all interpreted languages, may be slower than compiled languages like C or Fortran, historically used to implement numerical software. To speed up the execution time of the routines present inside DEBRA, the plugin C Coder present inside Matlab has been used to generate a C-like code called MEX file that can be called inside Matlab during execution. This choice, although not ideal, ensured a computational speed-up of around 40 times with respect to the same code run using plain Matlab. C Coder plugin allows the user to translate numerically intensive user-written functions in C-like compiled language for higher computational efficiency while still retaining the level of abstraction of Matlab.

2.3.1 Friction laws

The monophasic SSSWE can represent any continuous fluid in which the horizontal scale is much larger than the vertical one. The frictional slope $\mathbf{S}_f$ distinguishes the behaviour of the fluid being modelled. In the following all the rheological laws which can selected inside DEBRA will be listed. In flood propagation applications (Bonomelli et al., 2023) it is customary to model the bed friction using Manning's coefficient n, which must be adapted to the current formulation of the SSSWE, as reported in Maranzoni & Tomirotti (2022)

$$
\begin{aligned}
S_{f\xi} &= \frac{n^2 u \|\mathbf{v}\|}{h^{4/3}} \sqrt{1 + \tan^2 \vartheta_x + \tan^2 \vartheta_y} \\
S_{f\eta} &= \frac{n^2 v \|\mathbf{v}\|}{h^{4/3}} \sqrt{1 + \tan^2 \vartheta_x + \tan^2 \vartheta_y} \\
\|\mathbf{v}\| &= \sqrt{u^2 + v^2 + 2uv \sin \vartheta_x \sin \vartheta_y}
\end{aligned}
\tag{2.50}
$$

On the other hand, the Voellmy rheology (Voellmy, 1955) is frequently used to describe debris flows (Frank et al., 2017) and dense snow avalanches (Hergarten & Robl, 2015) and it is implemented in proprietary software like RAMMS (Christen et al., 2010), TRENT2D (Zugliani & Rosatti, 2021) and HEC-RAS (US Army Corps of Engineers, 2008). In the context of this application, the Voellmy's frictional slope can be expressed as

$$S_{f\xi} = \frac{u}{\|\mathbf{v}\|}\left(\frac{\mu}{\alpha} + \frac{\alpha\|\mathbf{v}\|^2}{\xi\, h}\right)$$
$$S_{f\eta} = \frac{v}{\|\mathbf{v}\|}\left(\frac{\mu}{\alpha} + \frac{\alpha\|\mathbf{v}\|^2}{\xi\, h}\right) \tag{2.51}$$
$$\|\mathbf{v}\| = \sqrt{u^2 + v^2 + 2uv\sin\vartheta_x \sin\vartheta_y} \qquad \alpha = \sqrt{1 + \tan^2\vartheta_x + \tan^2\vartheta_y}$$

where $\mu\ [-]$ is a Coulomb friction coefficient and $\xi\ [m/s^2]$ is a turbulent friction coefficient. A commercially available software for two-dimensional flood or mud-flood routing which has been widely applied for the assessment of debris flow hazard (Wu et al., 2013) is FLO-2D (FLO-2D Software, 2006). FLO-2D has been approved as a hydraulic program for flood and debris flow simulation by Federal Emergency Management Agency of the United States (FLO-2D Software, 2006). To model debris flows, FLO-2D uses an ad-hoc rheology first proposed by O'Brien et al. (1993) from measurements of shear stress in fluids at various rates of angular deformation. The O'Brien frictional slope has been modified with respect to its original formulation to be compatible with the SSSWE formulation, and it given by

$$S_{f\xi} = \frac{u}{\|\mathbf{v}\|}\left(\frac{\alpha\,\tau_y}{\gamma_m h} + \frac{K\,\eta|u|\,\alpha^2}{8\,\gamma_m h^2} + \frac{n_t^2 u\|\mathbf{v}\|\alpha}{h^{4/3}}\right)$$
$$S_{f\eta} = \frac{v}{\|\mathbf{v}\|}\left(\frac{\alpha\,\tau_y}{\gamma_m h} + \frac{K\,\eta\,|v|\,\alpha^2}{8\,\gamma_m h^2} + \frac{n_t^2 v\|\mathbf{v}\|\alpha}{h^{4/3}}\right) \tag{2.52}$$
$$\|\mathbf{v}\| = \sqrt{u^2 + v^2 + 2uv\sin\vartheta_x \sin\vartheta_y} \qquad \alpha = \sqrt{1 + \tan^2\vartheta_x + \tan^2\vartheta_y}$$

where $\tau_y\ [N/m^2]$ is the yield stress of the granular material, $\gamma_m\ [N/m^3]$ is the specific weight, $K\ [-]$ is a resistance parameter for laminar flow, $\eta\ \ [Pa\cdot s]$ is the viscosity and $n_t\ [s/m^{1/3}]$ is the turbulent Manning's coefficient. Viscosity, yield stress and turbulent Manning's coefficient are shown to be functions of the volumetric sediment concentration C_v of silts, clays and fine sands according to the relations (O'Brien, 1988)

$$\eta = \alpha_1 e^{\beta_1 C_v} \qquad \tau_y = \alpha_2 e^{\beta_2 C_v} \qquad n_t = 0.0538\, n\, e^{6.0896\, C_v} \tag{2.53}$$

where $\alpha_1, \alpha_2, \beta_1$ and β_2 are empirical coefficients defined by laboratory experiments (O'Brien & Julien, 1988).

2.4 Validation

In the following a selection of test cases are reported to assess the performance of the proposed numerical scheme against either simple analytical solutions or the computed solution of a reference software already used in literature to model debris flow, i.e. RAMMS. Additional test cases concerning the standard implementation of the SWE are reported in Appendix D and also in Bonomelli et al. (2023).

2.4.1 Dam break on a sloping channel with Coulomb friction

This test case is taken from Mangeney et al. (2000) in which the one dimensional flow of an incompressible fluid is described by mass and momentum equations. With reference to Figure 2.8, a fluid of height h is released from rest at the initial instant on a topography given by a uniform slope inclined by ϑ. The initial conditions represent the well-known dam break problem in hydraulics. Interestingly, a Coulomb type friction is present in this formulation, allowing the schematic representation of a debris flow or a dense snow avalanche. Mangeney et al. (2000) gives an analytic solution for this problem with these conditions, employing the method of characteristics, closely following the approach of Stoker (1957).

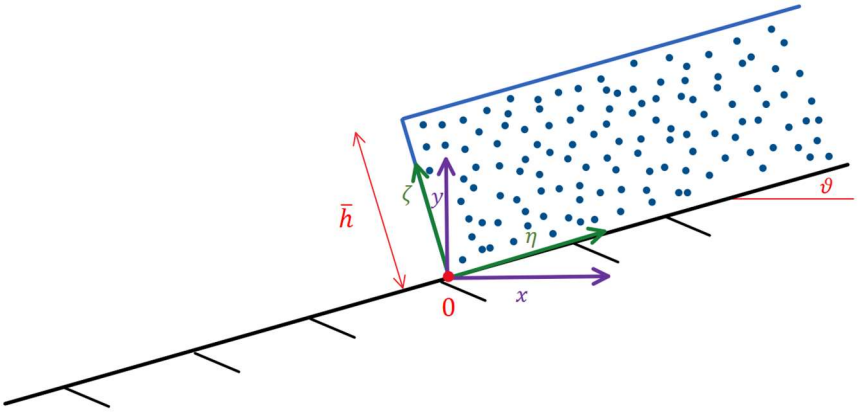

Figure 2.8 Schematics of the dam break problem on a sloping bed with Coulomb friction for a fluid of height h released from rest on a sloping bed inclined by ϑ. Two reference systems are depicted: one bottom oriented $(\eta\ \zeta)$ and one cartesian $(x\ y)$, to better explain the different formulations of the SWE adopted.

The analytical solution to this problem for the fluid depth $\bar{h}$ and the velocity $\bar{u}$, in bottom oriented coordinates is given by

$$\bar{h}(\eta,t)=\begin{cases}0 & \eta\le\eta_L\\ \dfrac{1}{9\,g\cos\vartheta}\left(\dfrac{\eta}{t}+2\,c_0-\dfrac{1}{2}m\,t\right)^2 & \eta_L<\eta<\eta_R\\ \bar{h}_0 & \eta\ge\eta_R\end{cases}$$

$$u(\eta,t)=\begin{cases}0 & \eta\le\eta_L\\ \dfrac{2}{3}\left(\dfrac{\eta}{t}-c_0+m\,t\right) & \eta_L<\eta<\eta_R\\ \dfrac{2}{3}\left(\dfrac{\eta_R}{t}-c_0+m\,t\right) & \eta\ge\eta_R\end{cases} \tag{2.54}$$

$$\eta_L=-2c_0t+\frac{1}{2}m\,t^2 \qquad \eta_R=c_0t+\frac{1}{2}mt^2$$

where $c_0=\sqrt{g\bar{h}_0\cos\vartheta}$ is the speed of propagation of "small disturbances" relative to the moving stream (Stoker, 1957), $m=-g\sin\vartheta+g\cos\vartheta\,\mu$, with μ being the friction coefficient appearing in the Voellmy's rheology, η and t are the space and time coordinates respectively. The following test has been carried out using the 2D formulation of the DEBRA numerical scheme, using a large domain and extracting a cross-section in the middle to plot the flow behaviour. Transmissive boundary conditions are used in this simulation since the flow does not interact with the edges of the domain. A cutoff threshold of $10^{-5}\,m$ on the fluid depth is used to neglect excessively low fluid depths which are unphysical and cause numerical problems. Other parameters required to set up the simulation are reported below

- $\bar{h}=2\,m$
- $\vartheta=30°$
- $\mu=\tan(10°)=0.176$
- $L\,(domain\,length)=2\,000\,m$
- $\Delta x\,(average\,cell\,spacing)=1\,m$
- $h_{cutoff}=10^{-5}\,m$

Overall, see Figure 2.9, DEBRA is able to capture the global behaviour of the flow with reasonable accuracy. Notice how the velocity upstream the rarefaction wave is captured remarkably well by the model. The solution is plotted in the $\xi\,\eta$ frame of reference, therefore, the output of the numerical scheme must be corrected according both to the inclination of the bottom bed and the local slope of water surface, as showed in Maranzoni & Tomirotti (2023)

$$\bar{h}_{DEBRA}=\frac{h}{\cos\vartheta_x}\left(\frac{1}{1+\tan\vartheta_x\,S_{WSE}}\right) \tag{2.55}$$

where S_{WSE} is the slope of fluid surface in the streamwise direction.

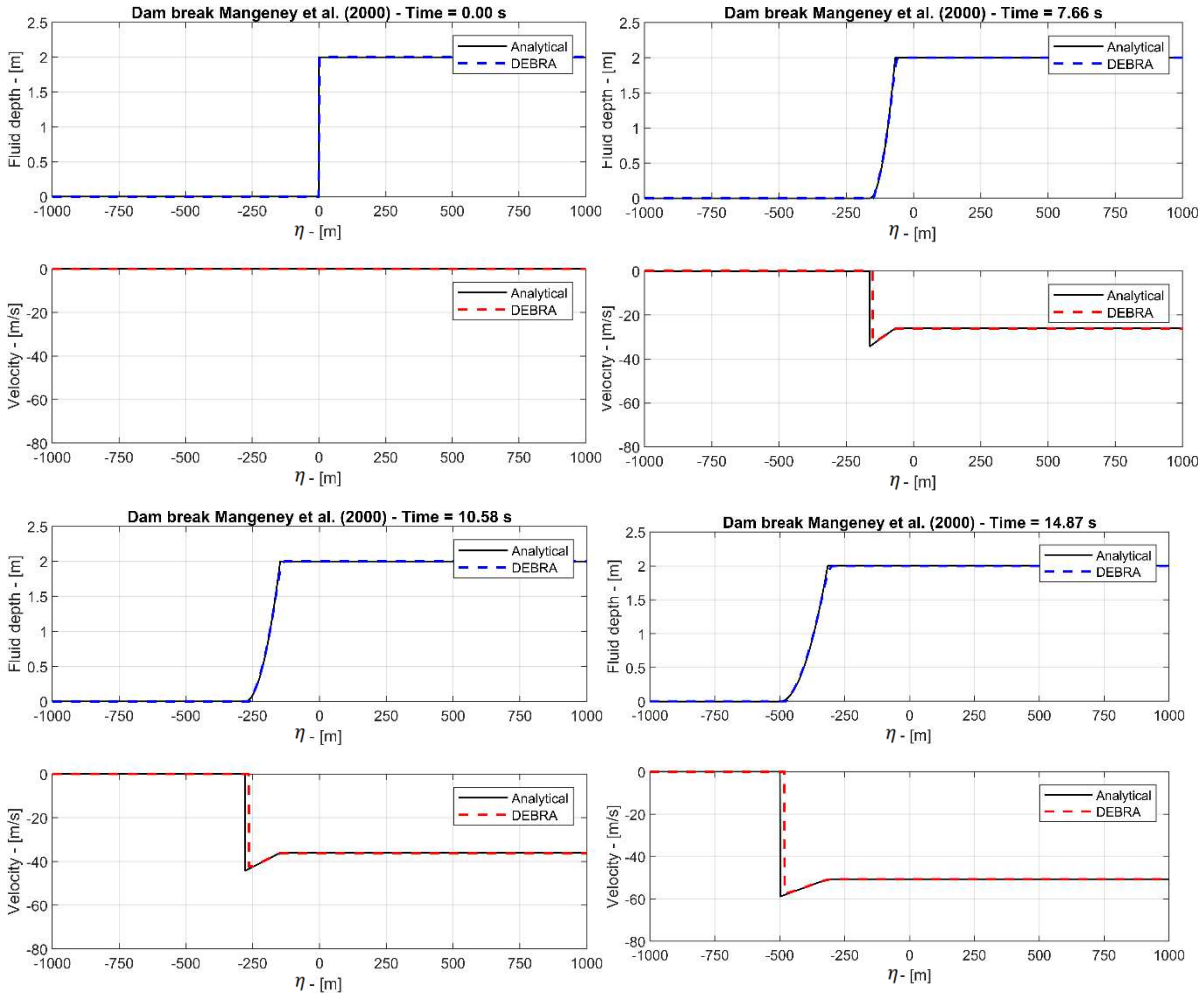

Figure 2.9 Snapshots of the numerical simulation at different time instants. DEBRA (dashed red line) is able to closely follow the evolution of the flow, as confirmed by the analytical solution (solid black line). The slight underestimation of the propagation speed is mostly due to the extremely low fluid depths present at the discontinuity at the wet-dry interface.

2.4.2 Flow over a sloping channel with multiple friction laws

The following test case is taken from the contribution of Hergarten & Robl (2015). A block of material is suddenly released on an inclined plane, similarly to the previous test case. The movement of a granular material with a constant flow depth on a planar slope in one dimension in presence of the Voellmy's friction law admits a simple analytical solution for the velocity as a function of time. If the flow depth is constant then the momentum equation in bottom oriented coordinates from a Lagrangian point of view can be written as

$$\frac{du}{dt} = g\left(S_b - S_f\right) \tag{2.56}$$

which, considering the Voellmy's friction law, becomes

$$\frac{du}{dt} = g\left(\sin\vartheta - \mu\cos\vartheta - \frac{u^2}{\xi\,\bar{h}}\right) \tag{2.57}$$

Eq. (2.57) is a Riccati equation which can be solved analytically to determine the unknown velocity as a function of time, as reported in Hergarten & Robl (2015)

$$u(t) = u_\infty \tanh\left(\frac{t}{T}\right)$$
$$u_\infty = \sqrt{\xi \bar{h}(\sin\vartheta - \mu\cos\vartheta)} \qquad T = \frac{\xi\,\bar{h}}{g\,u_\infty} \tag{2.58}$$

where u_∞ is the uniform velocity, i.e. the steady-state velocity reached by the flow, where the stresses exactly balance the source term given by the slope, and T is a characteristic time, describing how quickly the velocity reaches the asymptotic value u_∞. Actually, when $t = 2T$, the velocity is 96% of the asymptotic value. Eq. (2.58) is a simple and interesting piece of information to evaluate the appropriateness of the uniform flow approximation in real situations. The terminal velocity assumes a real value only when $\tan\vartheta > \mu$, meaning that the slope of the channel must be higher than the coefficient of friction in order for the uniform form to establish. This reflects the simple observation that the friction forces are higher than the energy that the flow acquires through gravity and therefore a balance between the two, i.e. the steady state velocity is impossible. Practically this flow existence property can be used to calibrate the friction parameter μ on the basis of the local slope angle in correspondence of which the debris flow has stopped propagating (assuming that monophasic assumptions are still valid). The implemented solver has been tested using the following data

- $\bar{h} = 1\ m$
- $\vartheta = 30°$
- $\mu = 0.2$
- $\xi = 1000\ m/s^2$
- $L\ (domain\ length) = 2\ 000\ m$
- $\Delta x\ (average\ cell\ spacing) = 1\ m$
- $h_{cutoff} = 10^{-5}\ m$

as initial conditions and parameters of the problem and the obtained results are shown in Figure 2.10.

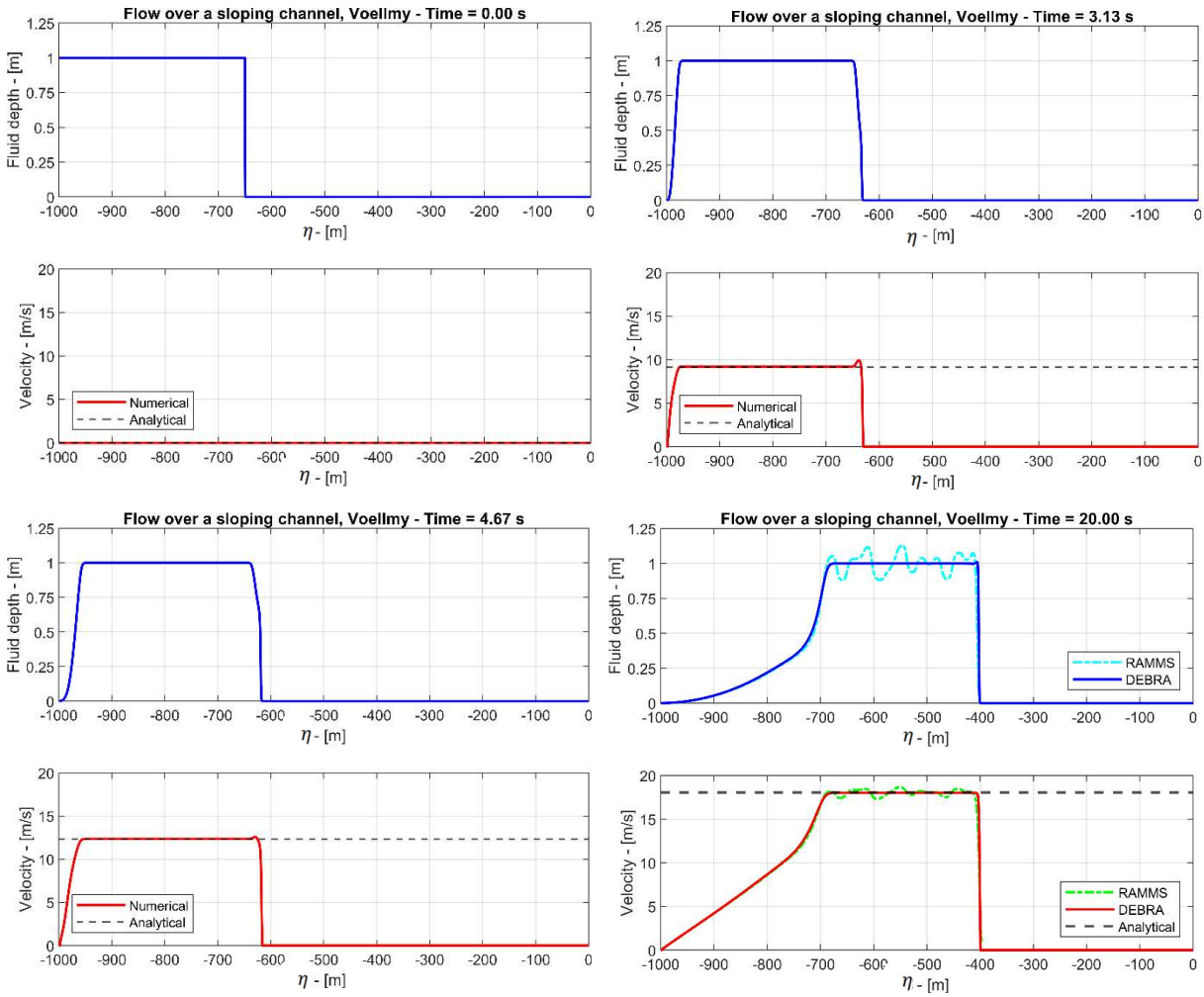

Figure 2.10 Snapshots of the numerical simulation at different time steps. The analytical solution (depicted with a dashed black line) represents the transient velocity which the flow reaches where the fluid depth is constant. Using the data reported in this test case the flow reaches the asymptotic velocity of about $18\ m/s$ in $t = 2T = 11.27\ s$, where $T = 5.63\ s$, as stated by the characteristic time of eq. (59). In the bottom right panel a comparison using RAMMS and DEBRA is displayed. Although both models agree very well on the position of the shock, RAMMS exhibits some oscillatory behaviour both in the fluid depth and in the velocity.

As one can observe, DEBRA is able to closely follow the predicted analytical velocity at every time instant. In Figure 2.10 a comparison with RAMMS software with the same parameters and initial conditions is presented. As it can be noticed, RAMMS exhibits some oscillatory pattern which is difficult to explain giving the simplicity of the test case. Such oscillations appear to grow in time and are dependent both on the mesh resolution and on the channel slope, highlighting a behaviour which is not present in the main equations solved by RAMMS at each time step. Figure 2.11 reports a contour plot of eq. (2.58), which is a representation of the 3D surface of the function $u(\xi, \mu)$ at fixed fluid depth $\bar{h}$ and ϑ. Interestingly, the contour lines depicted in white highlight the path along which the terminal velocity is constant while ξ and μ vary. This behaviour stresses the property that there are multiple choices of (ξ, μ) that are characterized by the same uniform velocity. In other words, the choice of parameters (ξ, μ) that characterize a flow having a fixed terminal velocity is not unique, thus requiring some additional assumption or information about the flow, in order to avoid performing multiple simulations.

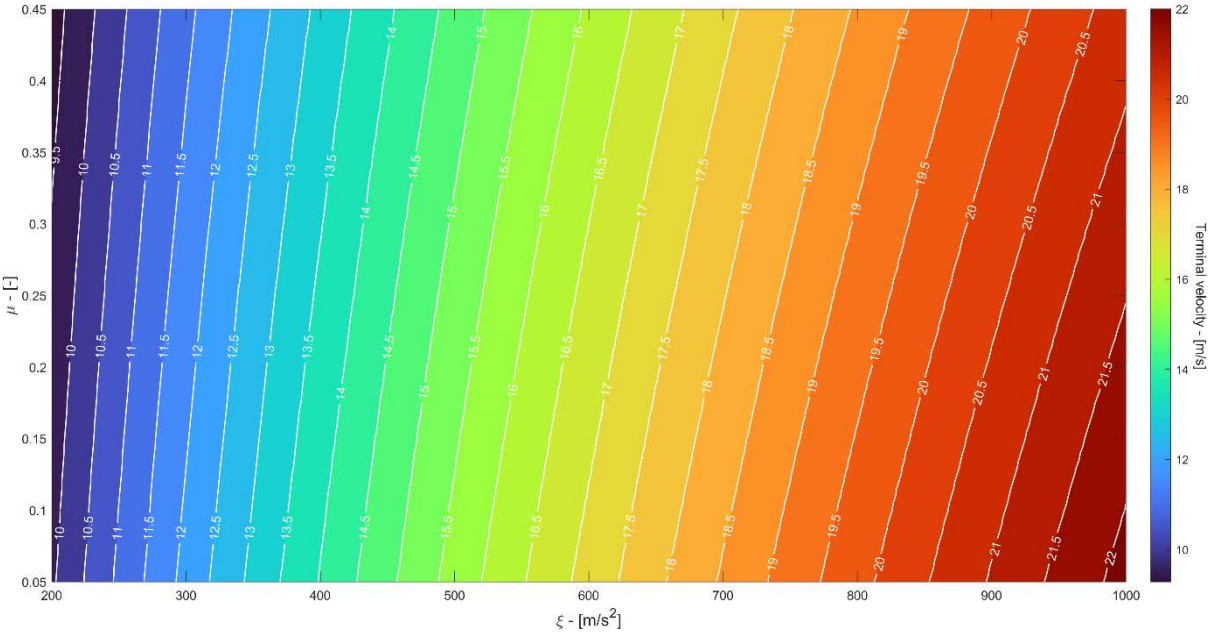

Figure 2.11 Contour plot of the terminal velocity reported in eq. (59) as a function of the Voellmy's rheological parameters ξ and μ, for $\bar{h} = 1$ and $\vartheta = 30°$.

A similar analytical solution can be found also considering the friction law proposed by O'Brien et al. (1993). This solution has not been considered in the literature yet, despite its usefulness in validating numerical schemes and for model calibration on simple test cases. Rewriting eq. (2.56) using the 1D simplification of eq. (2.52) in bottom oriented coordinates leads to

$$\frac{du}{dt} = g\left(\sin\vartheta - \frac{\tau_y}{\gamma_m \bar{h}} - \frac{K\,\eta\,u}{8\,\gamma_m \bar{h}^2} - \frac{n_t^2 u^2}{\bar{h}^{4/3}}\right) \tag{2.59}$$

which can be rewritten, using the following short-hand notation, as

$$u'(t) = A\,u^2(t) + B\,u(t) + C$$
$$A = -\frac{g\,n_t^2}{\bar{h}^{4/3}} \qquad B = -\frac{g\,K\,\eta}{8\,\gamma_m \bar{h}^2} \qquad C = g\sin\vartheta - \frac{g\,\tau_y}{\gamma_m \bar{h}} \tag{2.60}$$

Eq. (2.60) is a complete Riccati equation and can be solved analytically using the method of separation of variables. First note that the steady state solution of the differential equation can be obtained by setting $u'(t) = 0$ and solving eq. (2.60), which is just a second-degree polynomial. Such steady state velocity must exist for the flow to develop, which is equivalent to say that the discriminant of eq. (2.60), i.e. $B^2 - 4AC$ must be positive. As a first step, solve the integral given by

$$\int \frac{du}{A\,u^2 + B\,u + C} = \int dt \tag{2.61}$$

Focusing on the denominator of the left side of eq. (2.61), by completing the square it is possible to write

$$A\,u^2 + B\,u + C = A\left[\left(u + \frac{B}{2A}\right)^2 + \frac{4\,A\,C - B^2}{4\,A^2}\right] \tag{2.62}$$

which, after some algebraic manipulation, can be expressed as

$$\begin{gathered} A\,u^2 + B\,u + C = A\,\varphi\left[\left(\frac{u + B/2A}{\sqrt{\varphi}}\right)^2 + 1\right] \\ \varphi = \frac{4\,A\,C - B^2}{4\,A^2} \end{gathered} \tag{2.63}$$

Finally eq. (2.63) is ready to be integrated leading to the solution

$$t + \varepsilon = \frac{\sqrt{\varphi}}{A\,\varphi}\arctan\left(\frac{u + B/2A}{\sqrt{\varphi}}\right) \tag{2.64}$$

where ε is a constant of integration to be computed using the condition that the initial velocity is zero, i.e. $u(0) = 0$. Eq. (2.64) can be manipulated to express the velocity u as a function of time

$$u(t) = -\tfrac{B}{2A} + \sqrt{\varphi}\tan\left[A\sqrt{\varphi}(t + \varepsilon)\right] \tag{2.65}$$

Note that the quantity φ is always negative when the flow exists. Accordingly, by invoking the trigonometric complex identity $\tanh(x) = -i\tan(i\,x)$, where i is the imaginary unit, one can rewrite eq. (2.65) as

$$\begin{gathered} u(t) = -\tfrac{B}{2A} + \sqrt{|\varphi|}\tanh\left[\tfrac{(t+\varepsilon)}{T}\right] \\ \varepsilon = -\frac{1}{A\sqrt{|\varphi|}}\operatorname{atanh}\left(\frac{B}{2A\sqrt{|\varphi|}}\right) \\ T = \frac{2}{\sqrt{|B^2 - 4AC|}} \end{gathered} \tag{2.66}$$

where T is the characteristic time of the flow, which, as observed above, measures how quickly the flow reaches the asymptotical value. The obtained results provide some important conclusions useful for the use of FLO-2D. Considering that the asymptotic velocity can be written as

$$u_\infty = \left(B - \sqrt{B^2 - 4AC}\right)\frac{1}{2A} \tag{2.67}$$

One can conclude that

- The role of K and α_1 that appear in η (see eq. 2.54) are indistinguishable and can be considered as a single parameter, therefore reducing the number of degrees of freedom of the O'Brien parametrization.
- The asymptotic velocity larger than zero if and only if

$$\sin\vartheta - \frac{\tau_y}{\gamma_m \bar{h}} > 0 \tag{2.68}$$

  This limiting condition provides an important information for debris flow arrest together with a limit of the possible values that can be given to α_2 and β_2, something that is not mentioned in any of the FLO-2D manuals.

The following parameters are used to set up the simulation, using $\gamma_w = 9\,810\ N/m^3$ as the specific weight of the water and $\gamma_{matrix} = 26\,500\ N/m^3$ as the specific weight of the granular part of the flow. The other parameters are a variation on the rheological set called "Aspen pit 1" suggested by O'Brien (1993).

- $\bar{h} = 3\ m$
- $\vartheta = 40°$
- $\alpha_1 = 3.6 \cdot 10^{-3}\ Pa \cdot s$
- $\alpha_2 = 1.81 \cdot 10^{-2}\ N/m^2$
- $\beta_1 = 22.1$
- $\beta_2 = 25.7$
- $C_v = 0.43$
- $\gamma_m = 16\,987\ N/m^3 = \gamma_{matrix} \cdot C_v + \gamma_w \cdot (1 - C_v)$
- $n = 0.033\ s/m^{1/3}$
- $K = 2285$
- $L\ (domain\ length) = 2\,000\ m$
- $\Delta x\ (average\ cell\ spacing) = 1\ m$
- $h_{cutoff} = 10^{-5}\ m$

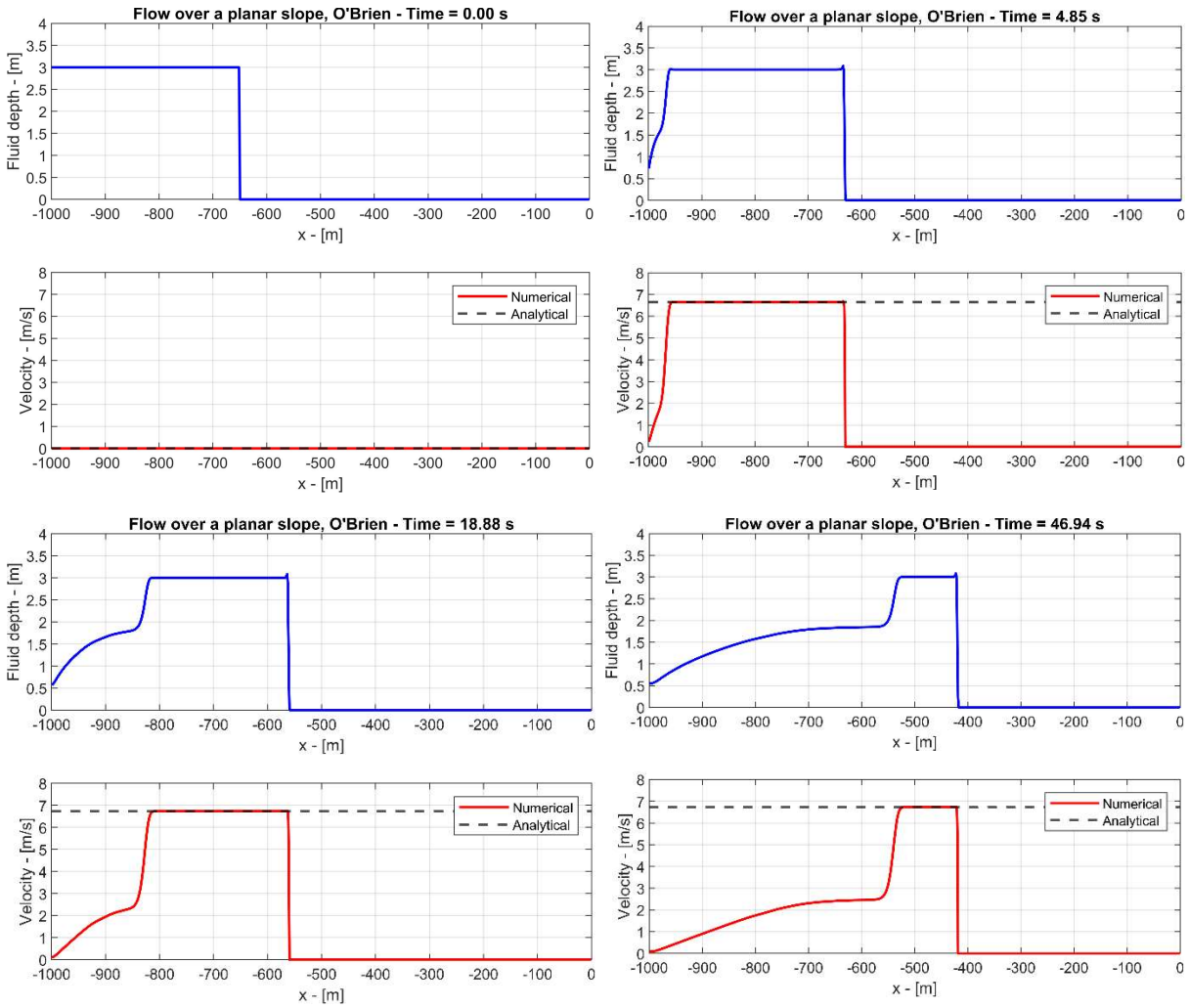

Figure 2.12 Snapshots of the numerical simulation at different time instants. The analytical solution (depicted with a dashed black line) represents the transient uniform velocity which the flow reaches where the fluid depth is constant. Using the data reported in this test case the flow reaches the asymptotic velocity of about 6.81 m/s in $t = 2T = 4.42\ s$, where $T = 2.21\ s$ as stated by the characteristic time of eq. (2.66)

Figure 2.12 shows the solution computed by DEBRA at different time steps. The good agreement between the analytical velocity and the computed one highlights the reliability of the implemented framework. Note that in correspondence of the wet/dry discontinuity a small tip in the fluid depth arises which appears to be stable in time and is caused by the rapid change in the conserved variables near the discontinuity. Although beyond the scope of this thesis, in the author's opinion, the presented solution suggests a direction for a systematic discussion of the comparative behaviour of the Voellmy's case and of the O'Brien case, as a function of the selected parameters set. Figure 2.13 reports a contour plot of eq. (68) which is a representation of the 3D surface of the function $u(C_v, h)$ with all the other parameters being fixed. Interestingly, the contour lines depicted in white highlight the path along which the terminal velocity is constant while C_v and h vary. Similarly to the Voellmy case, this behaviour stresses the property that there are multiple choices of C_v and h that are characterized by the same terminal velocity.

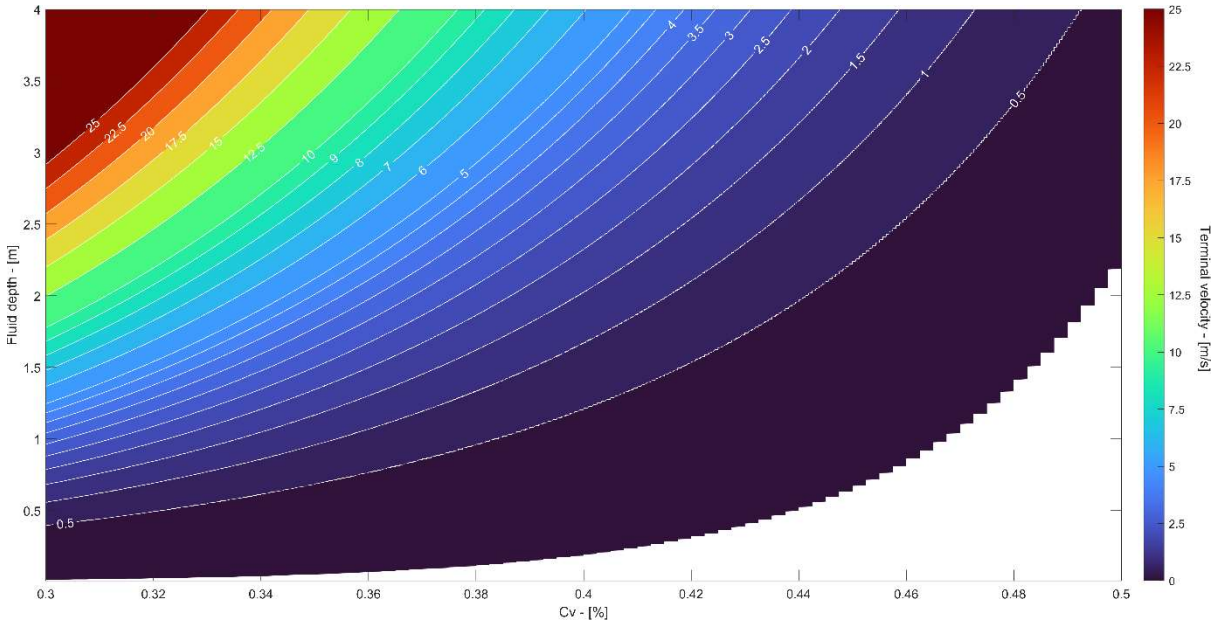

Figure 2.13 Contour plot of the terminal velocity reported in eq. (2.67) as a function of the O'Brien rheological parameters C_v and h. The other parameters present inside the O'Brien formulation are fixed and identical to the ones used to perform the numerical simulation with DEBRA, with the exception of $\vartheta = 10°$, modified for graphical purposes.

2.4.3 Multiplane test case

The following test case is a fully 2D scenario in which an initially stationary idealized block of debris mixture is free to flow along a valley whose surface is characterized by the intersection of four converging planes with slopes ranging between 10° and 45°. This scenario aims to replicate the propagation of a debris flow which is suddenly triggered along a hypothetical slope and afterwards channelized into the drainage network (see Figure 2.14 for a 3D representation). In order to compare the results provided by DEBRA with the ones provided by RAMMS software the friction law of Voellmy has been used to model the behaviour of the granular material.

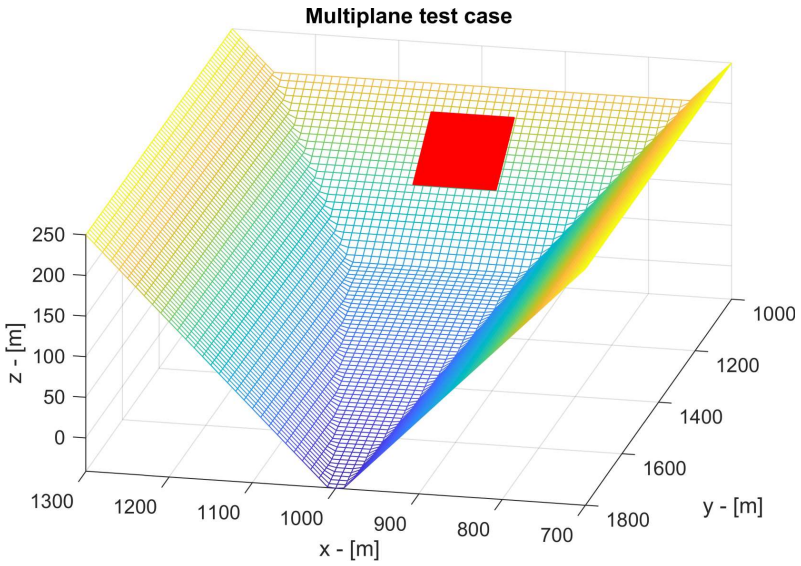

Figure 2.14 3D representation of the idealized valley made by the intersection of four planes. The red square (10 000 m^2) highlights the triggering region where the fluid is initially at rest.

The following data have been used for the described problem

- Domain length $\begin{cases} 700\ m \leq x \leq 1300\ m \\ 1\,000\ m \leq y \leq 1\,800\ m \end{cases}$

- Elevation data $z(x, y)$

$$\pi_1 = (y - 1\,000\ m) - 50\ m, \quad \pi_2 = (y - 1\,000\ m) - 50\ m$$
$$\pi_3 = -(x - 1\,000\ m) \cdot \tan(30°) + 200\ m, \quad \pi_4 = -(x - 1000\ m) \cdot \tan(10°) + 100\ m \qquad (2.69)$$
$$z(x, y) = \max[\pi_1(x), \pi_2(x), \pi_3(y), \pi_4(y)]$$

- Release area $\begin{cases} 950\ m \leq x \leq 1\,050\ m \\ 1\,050\ m \leq y \leq 1\,150\ m \end{cases}$
- $\bar{h} = 5\ m$
- $\mu = 0.18$
- $\xi = 500\ m/s^2$
- $\Delta x_{DEBRA}\ (average\ cell\ spacing) = 2.5\ m$
- $\Delta x_{RAMMS} = 2.5\ m$
- $t_{end}\ (simulation\ time) = 53\ s$
- $h_{cutoff} = 10^{-5}\ m$

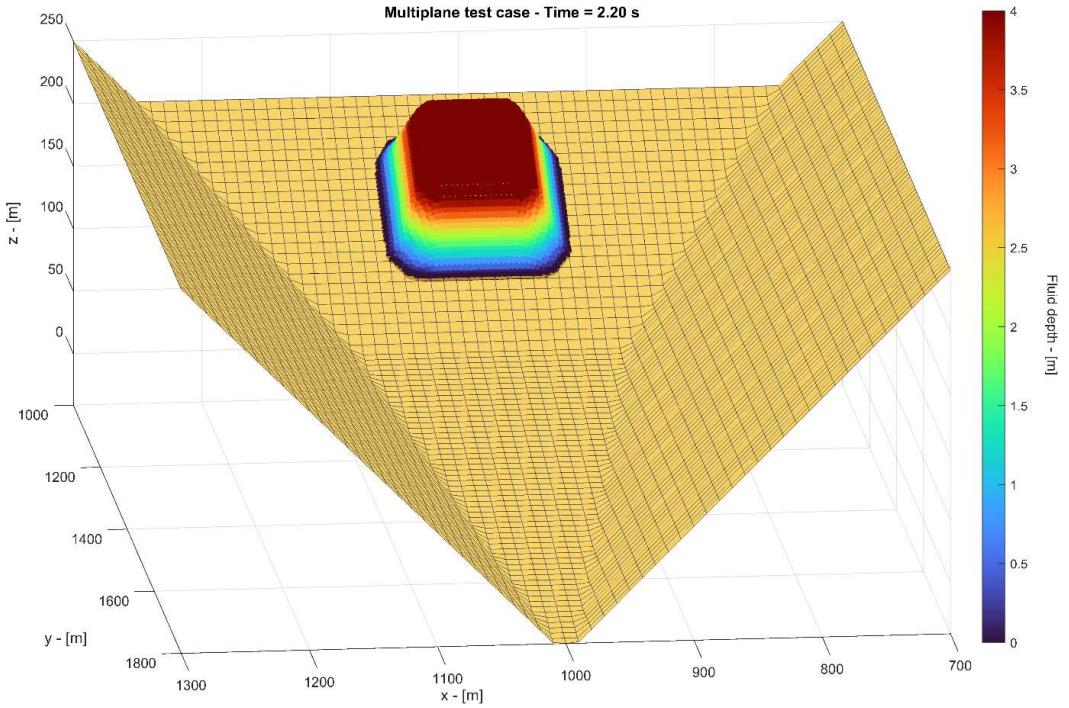
Multiplane test case - Time = 2.20 s
z - [m]
250
200
150
100
50
0
y - [m]
1000
1200
1400
1600
1800
x - [m]
1300
1200
1100
1000
900
800
700
Fluid depth - [m]
4
3.5
3
2.5
2
1.5
1
0.5
0

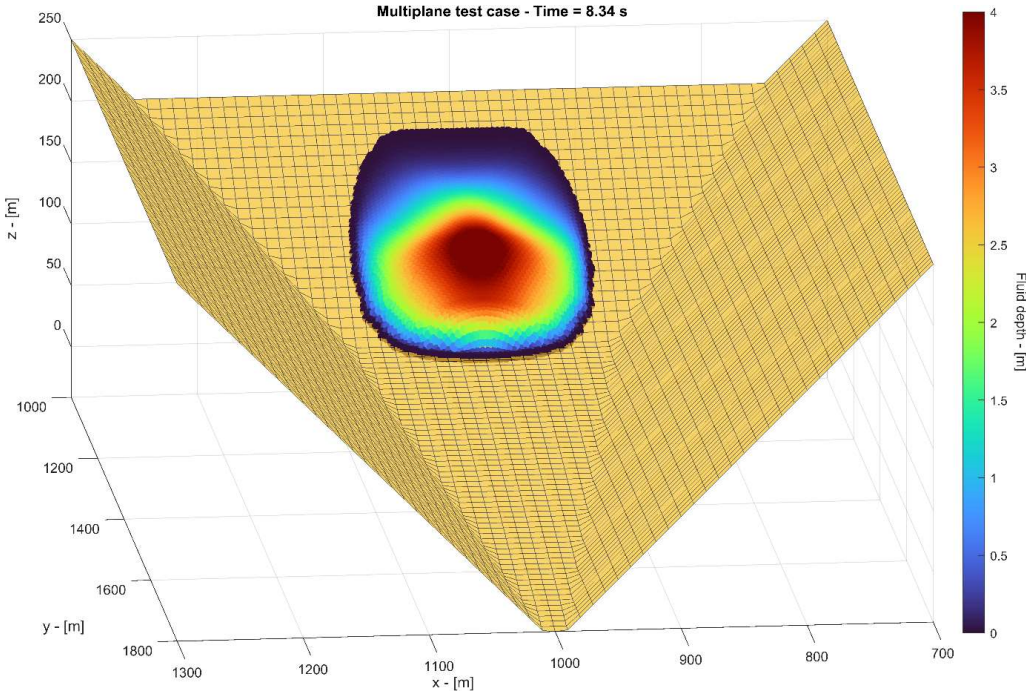
Multiplane test case - Time = 8.34 s
z - [m]
250
200
150
100
50
0
y - [m]
1000
1200
1400
1600
1800
x - [m]
1300
1200
1100
1000
900
800
700
Fluid depth - [m]
4
3.5
3
2.5
2
1.5
1
0.5
0

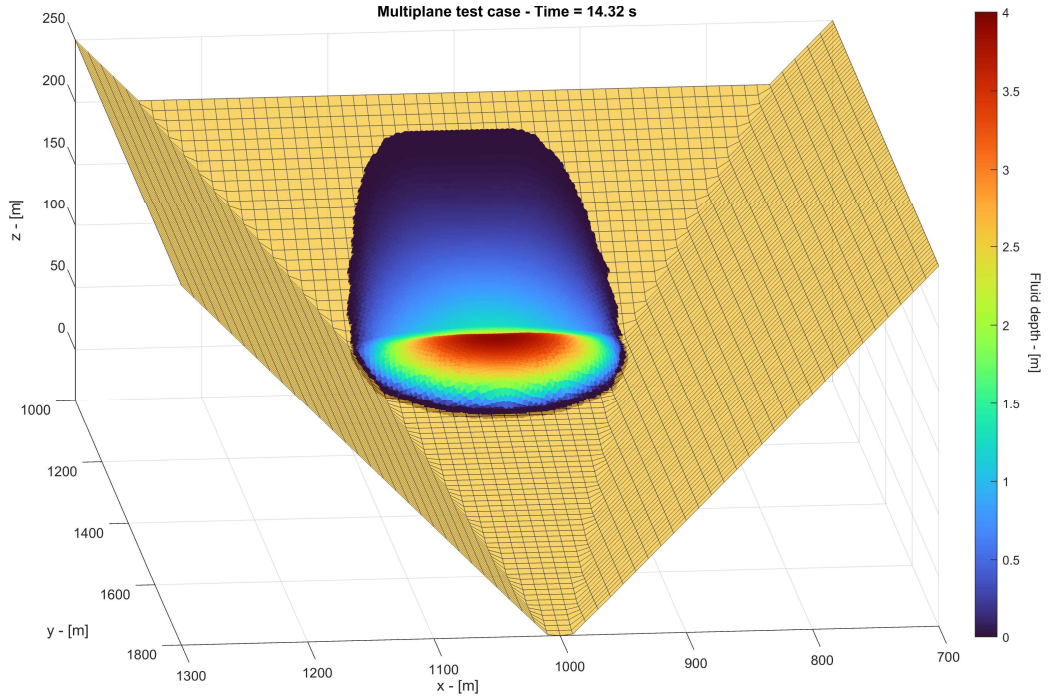
Multiplane test case - Time = 14.32 s
z - [m]
250
200
150
100
50
0
y - [m]
1000
1200
1400
1600
1800
x - [m]
1300
1200
1100
1000
900
800
700
Fluid depth - [m]
4
3.5
3
2.5
2
1.5
1
0.5
0

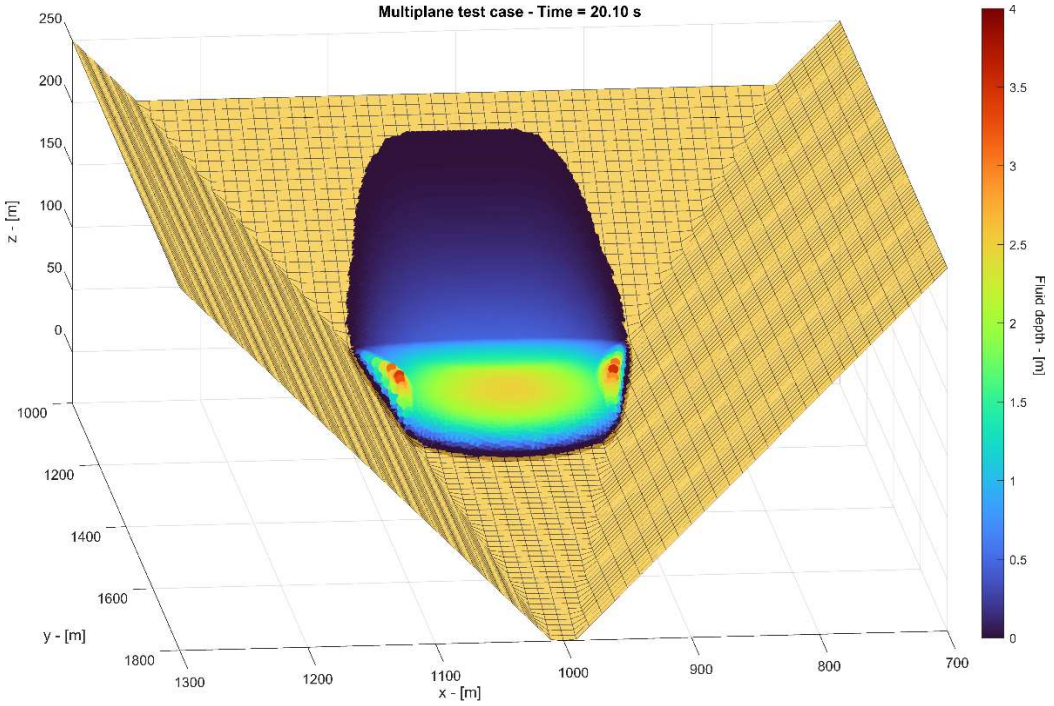
Multiplane test case - Time = 20.10 s
z - [m]
250
200
150
100
50
0
y - [m]
1000
1200
1400
1600
1800
x - [m]
1300
1200
1100
1000
900
800
700
Fluid depth - [m]
4
3.5
3
2.5
2
1.5
1
0.5
0

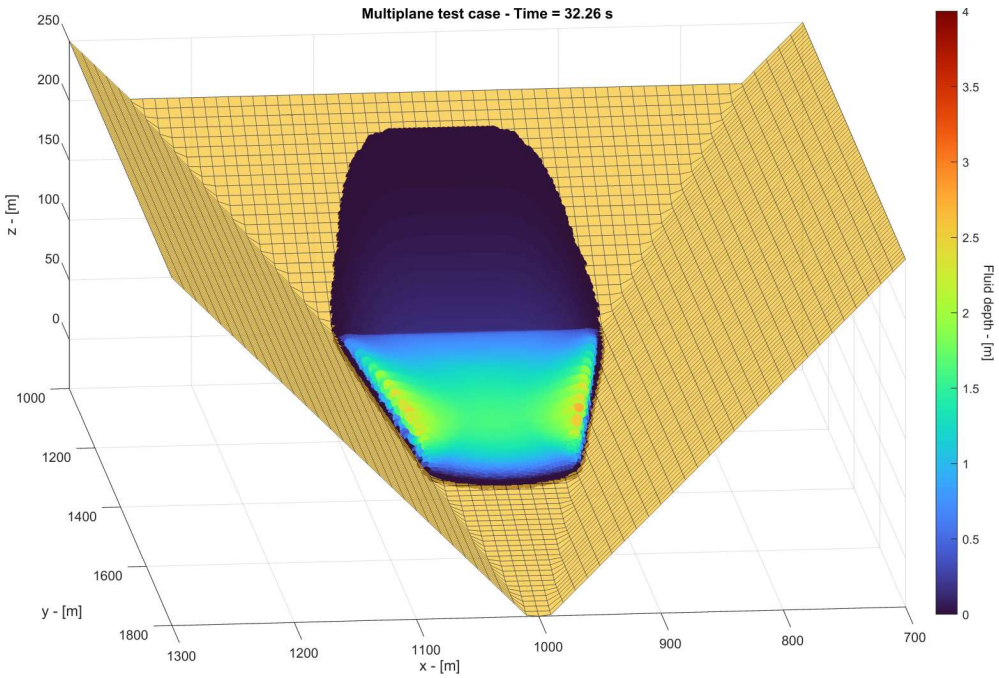

Figure 2.15 Snapshots of the results provided by DEBRA at different time steps, the vertical scale of the fluid has been enlarged for graphical reasons.

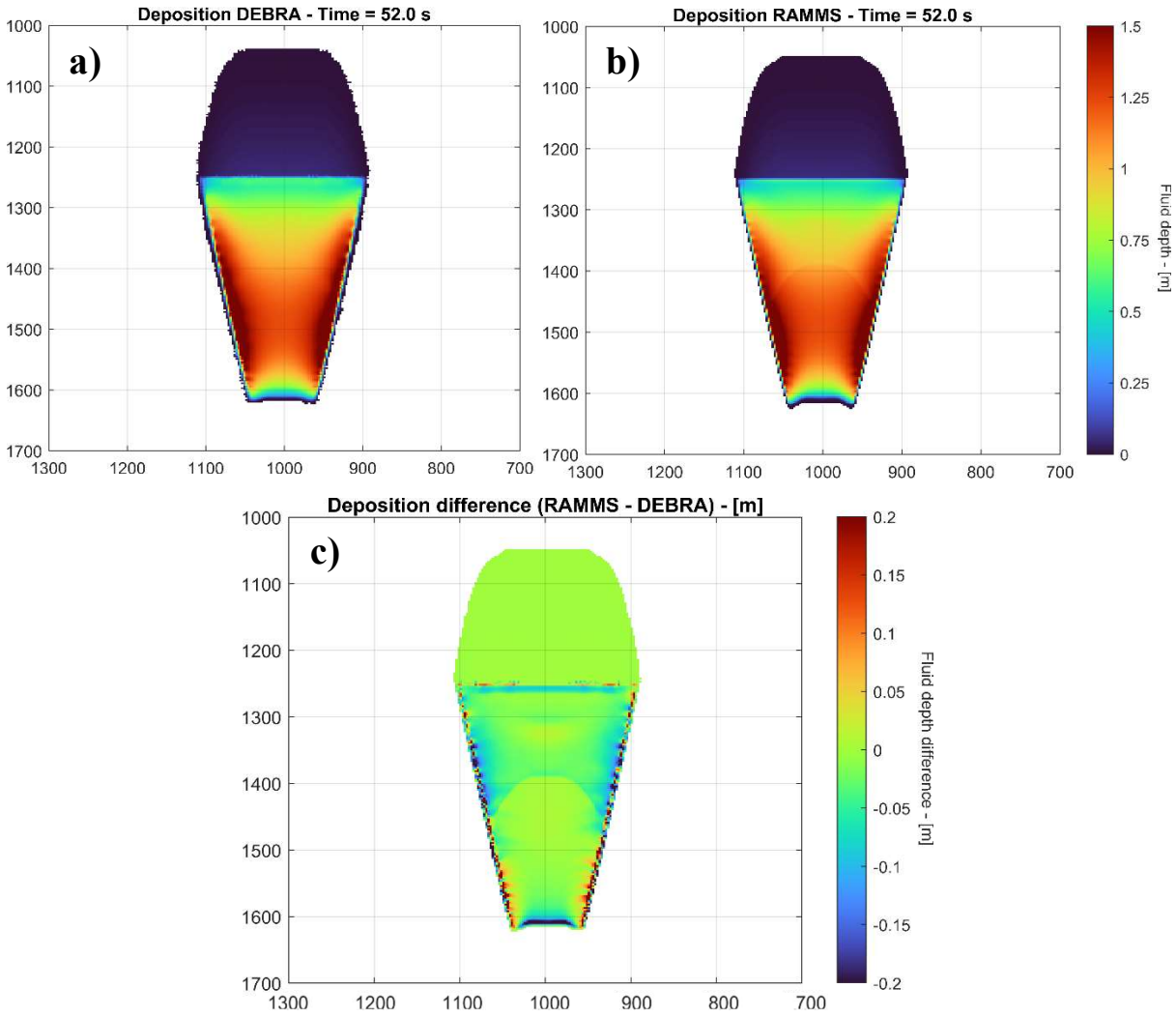

Figure 2.16 a) Deposition map using DEBRA software after 20 s. b) Deposition map using RAMMS software after 20 s. c) Difference between the computed deposition map of RAMMS and DEBRA.

In Figures 2.15 the snapshots of the fluid depth computed by DEBRA are reported, describing the motion of the debris flow, having a volume of 50 000 m^3, as it propagates downstream. After the complete stop, which occurs after about 53 s as obtained by implementing the stopping criteria provided by RAMMS, it is possible to assess the differences between the two solvers (see Figure 2.16). Although some discrepancies can be observed near the discontinuous change in bed slope, likely caused by the different kind of space discretization adopted (structured mesh used by RAMMS and unstructured used by DEBRA), these are nevertheless very limited (around 0.1 m of difference). It can be noticed that DEBRA has a tendency to homogeneously deposit along the channel (see the blue pattern in the wider portion of the bottom channel and the red pattern in the narrow portion of the channel) while RAMMS predicts that most material deposits near the portion in which the debris flow stops (between the 1 500 m and the 1 600 m mark). Finally both models predict the runout consistently occurring about the 1 600 m mark. Computationally both models are able to finish the simulation in under a minute.

2.4.4 Niardo event

As a final comparative test case, a real debris flow occurred in Valle Camonica is considered. On the 27th of July 2022 the town of Niardo located in Valle Camonica (see Figure 2.17) has experienced an extreme rainfall event (maximum rainfall intensity of around 250 mm/h, see Figure 2.18) in an area where the official 200 years return period rainfall is about 63 mm/h. This downpour triggered a debris flow caused by multiple soil slips located in the catchment of Re and Cobello stream (see Figure 2.19).

Figure 2.17 Study area location with an enlarged view of Northern Italy.

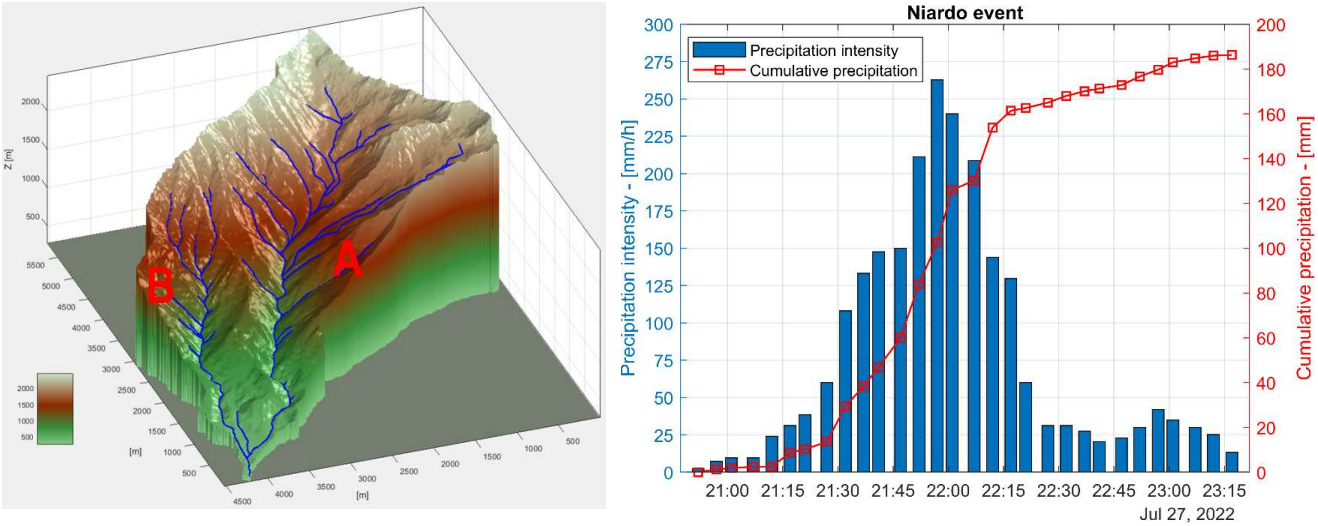

Figure 2.18 (Left) Visualization of the catchment of Re stream (A) and Cobello stream (B). (Right) Precipitation data recorded by an amatorial meteo station present in Niardo (https://www.meteopassione.com/webcam/niardo).

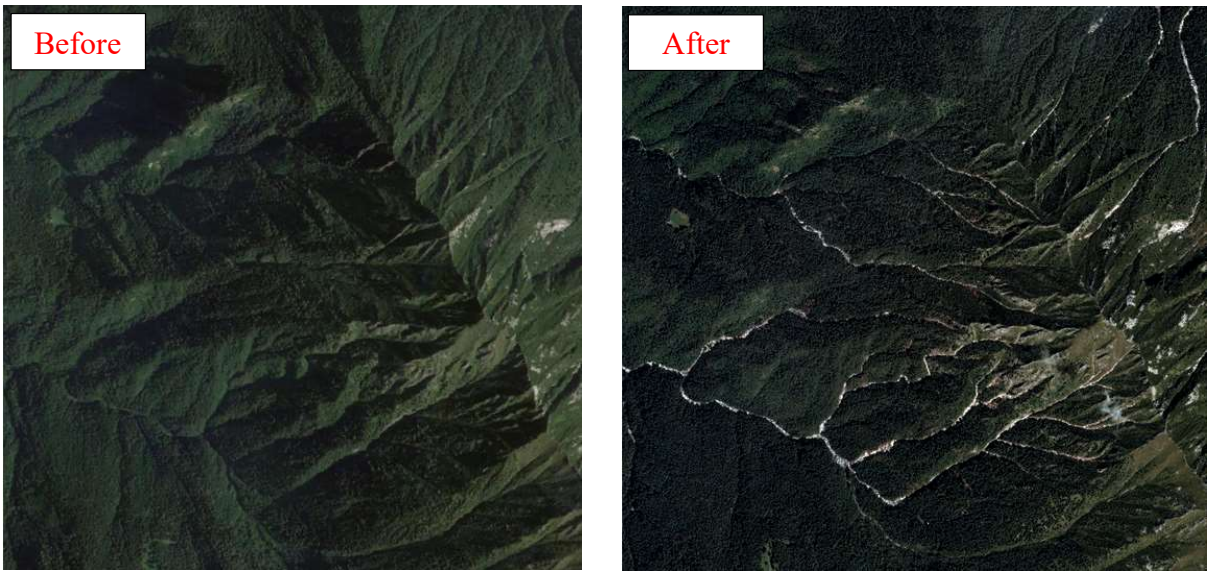

Figure 2.19 A comparative view of the change in morphology of the catchments of Re (south) and Cobello (North), aerial view taken from Google Earth before the event and immediately afterwards. There are more than 40 unstable source areas that contributed to the debris flow that damaged the town of Niardo.

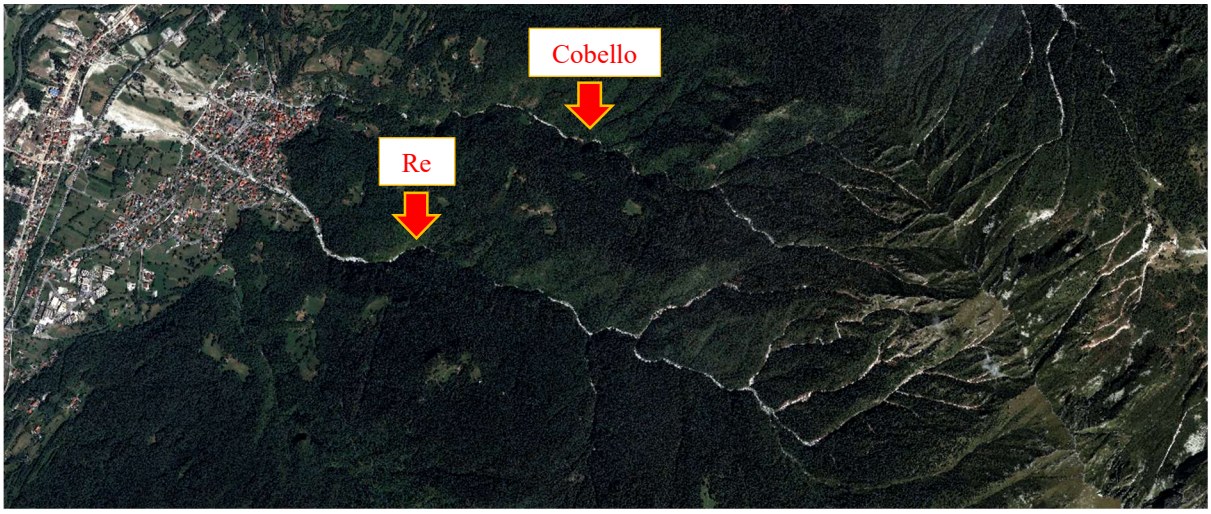

Figure 2.20 Aerial view of Niardo after the event where the path of the debris flow is evident, image taken from Google Earth.

The reported event can be used to assess the performances of the numerical models RAMMS and DEBRA (considering the Voellmy's frictional law) on a real topography. As it can be noticed from Figure 2.20, two distinct debris flows have occurred in Niardo which originated from the catchments of Re and Cobello stream. While the timing of the events is unknown, it is evident from Figure 2.20 that the deposition by the overflow of Re stream is much severe with respect to the one caused by the overflow of Cobello stream. For this reason the debris flow caused by Re stream only will be numerically investigated. Due to the many uncertainties intrinsic to any debris flow which occurs in ungauged catchments, the correct representation of the flow by numerical models is difficult and often requires many steps to calibrate all parameters involved in the available numerical model. With reference to Niardo, it is known from local witnesses that the propagation of the debris flow (from when the Re stream overflowed and caused major damages) did not outlast half an hour. Furthermore depositional height in several areas of the domain impacted by the debris flow allowed the estimation of the solid volume of the event to be in the order of $60\ 000\ m^3$. Since no information is available on the debris flow hydrograph at the apex of the alluvial fan of the Re catchment and considering that the purpose of this test is mostly comparative, two idealized boundary condition will be used to replicate the event. First an idealized block of debris flow will be released in the upper portion of the catchment of Re stream, allowing the flow to propagate both inside and outside the channel bed. RAMMS software allows two kinds of initial conditions: block release (which is used in the following section) and input hydrograph. The latter seems more suitable for this application but, due to the poorly documented manual and lack of implementation details, it was not possible to reach an agreement between RAMMS and DEBRA. Furthermore, the specification of a planimetric area instead of a cross section in the domain for the region in which the hydrograph enters is not well motivated and documented in the manual. Therefore, in the following section a block release has been used as initial condition where a rigorous comparison is possible since the starting configuration is the same in both models. Lastly, a hydrograph boundary condition will be used to replicate the Niardo event using DEBRA only. In all simulations the railway bridge (see Figure 2.21, location A) is treated as a solid wall from the beginning as a simple and straightforward way to model the bridge obstruction during the event. In RAMMS it not possible to dynamically change the domain during a simulation, therefore the easiest way to model the flow interaction was to treat it as a solid wall from the start. To avoid differences in the two models also in DEBRA the same approach to model the railway bridge is adopted.

Figure 2.21 Helicopter view of Niardo the day after the debris flow event. From the image it is possible to assess the critical points in which the Re stream overflowed, which are located in correspondence of the railway bridge (downstream, A) and the highway bridge (upstream, B).

2.4.4.1 Block release

The initial condition of a block release was initially used to provide a comparative test case. It aims to replicate the sudden loss of stability of a soil block located in the steep portions of the catchment. Unfortunately no data about the soil depth is available at a reasonable resolution in the areas in which the soil instability occurred. Therefore in this application a fictitious uniform channel tilted 30° is attached to the DTM of the town of Niardo on which the block of debris material is suddenly released.

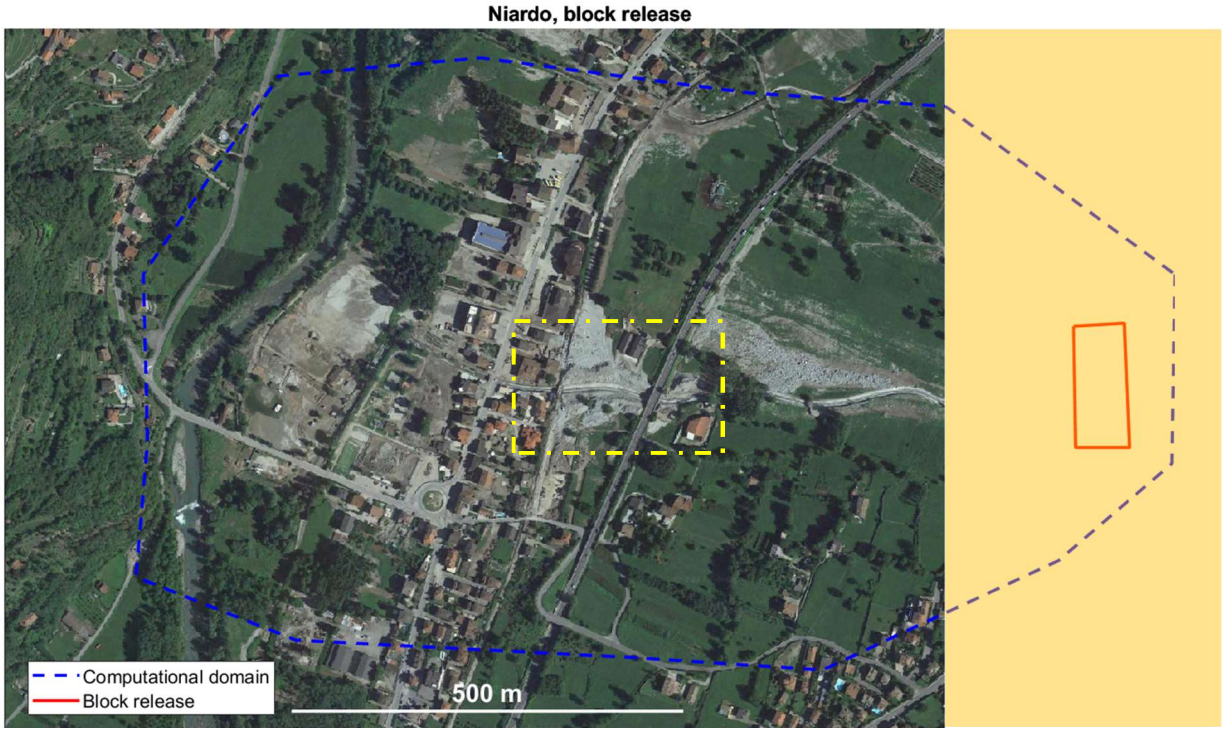

Figure 2.22 Domain schematics for the Niardo block release test case. The dashed blue line highlights the domain extension while the solid red line indicates the position of the block release depicted in orange. Lastly the yellow-dashed line is the position of the enlargement displayed in Figure 2.23.

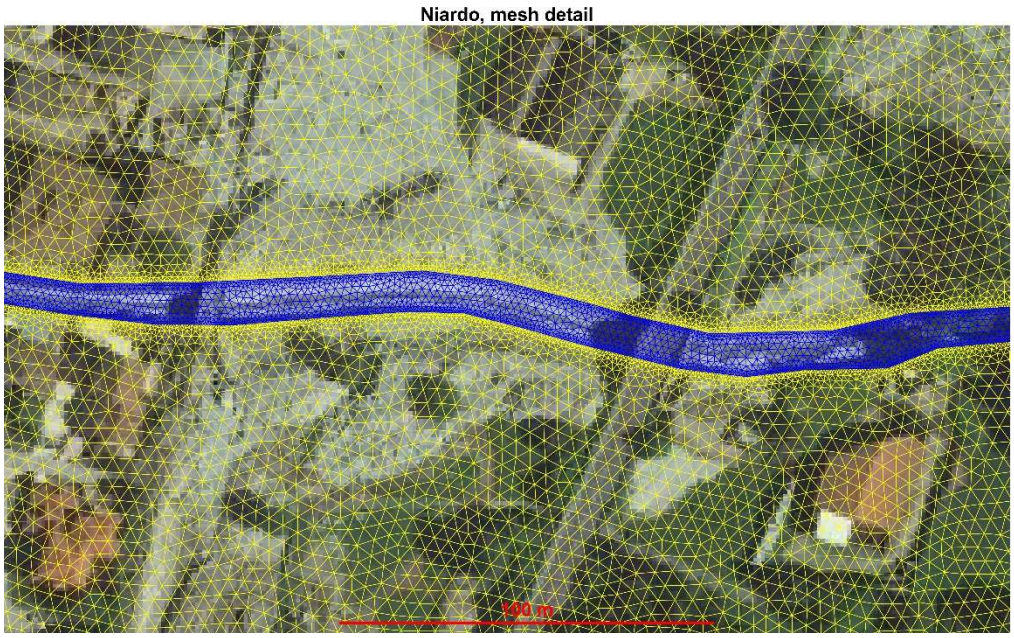

Figure 2.23 Zoom on the computational mesh adopted in DEBRA. To closely follow the channel geometry, two break lines are introduced to provide a mesh refinement inside the channel (mesh size 0.5 m) with respect to the outside floodplain (mesh size 2 m).

The following initial conditions and parameters are used for the setup of the simulation

- $\Delta x_{DEBRA}(mesh\ size) = \begin{cases} 0.5\ m\ (inside\ the\ channel\ bed) \\ 2\ m\ (outside\ the\ channel\ bed) \end{cases}$
- $\Delta x_{RAMMS}(mesh\ size) = 1.5\ m\ (everywhere)$
- $A_R(release\ area) = 10\ 000\ m^2$
- $\bar{h}\ (release\ height) = 5\ m$
- $\mu = 0.05$
- $\xi = 1000\ m/s^2$
- $t_{end}(simulation\ time) = 500\ s$
- $h_{cutoff} = 10^{-5}\ m$

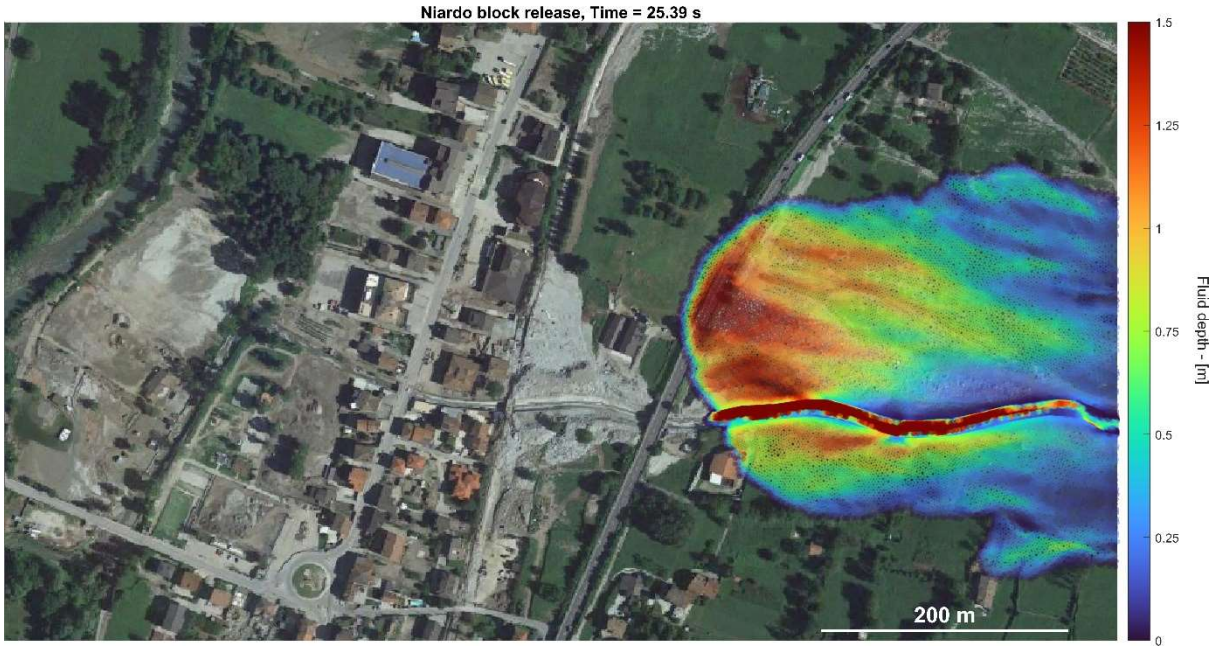
Niardo block release, Time = 25.39 s
200 m
Fluid depth - [m]
1.5
1.25
1
0.75
0.5
0.25
0

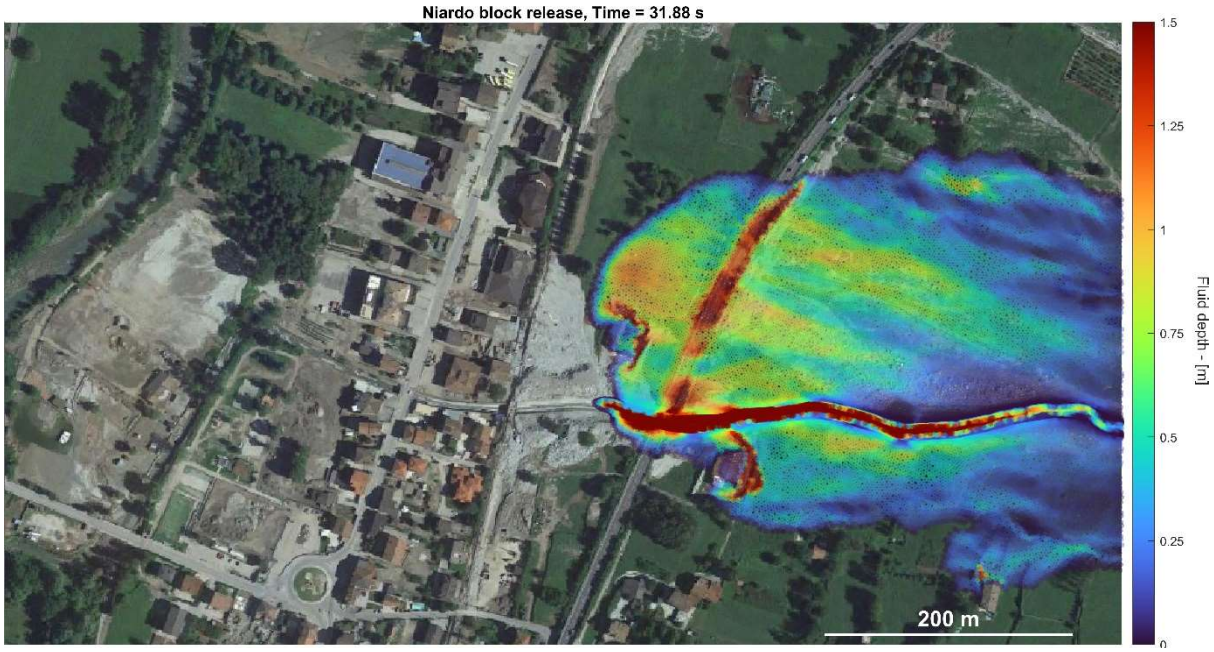
Niardo block release, Time = 31.88 s
200 m
Fluid depth - [m]
1.5
1.25
1
0.75
0.5
0.25
0

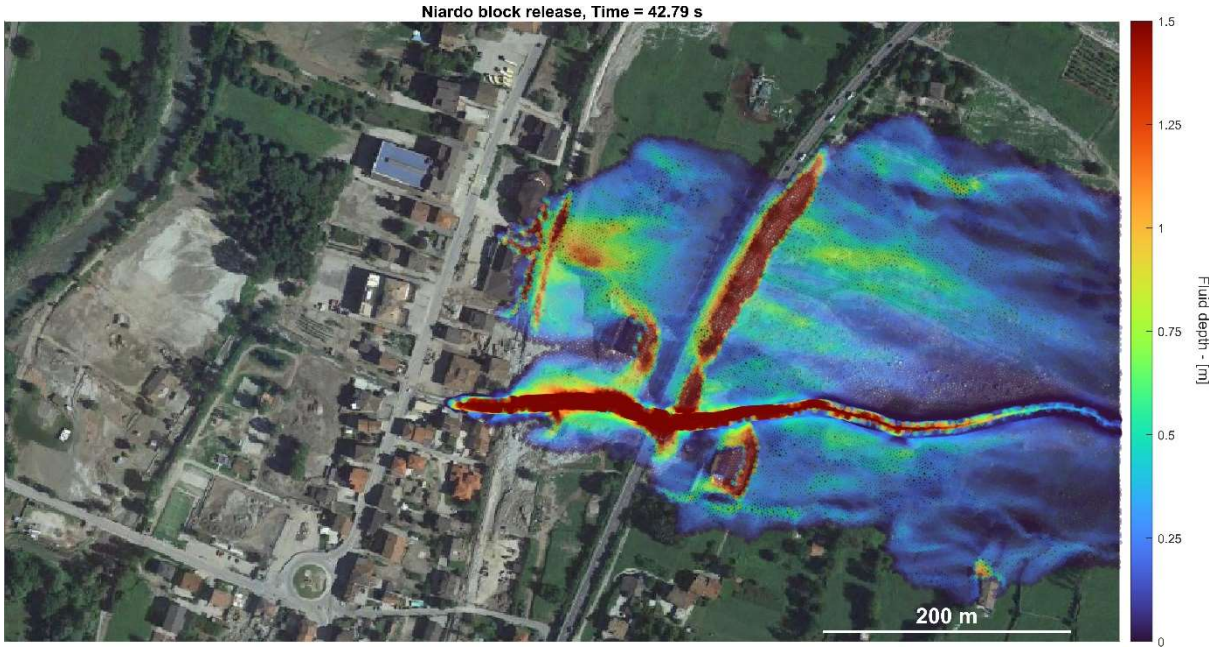
Niardo block release, Time = 42.79 s
200 m
1.5
1.25
1
0.75
0.5
0.25
0
Fluid depth - [m]

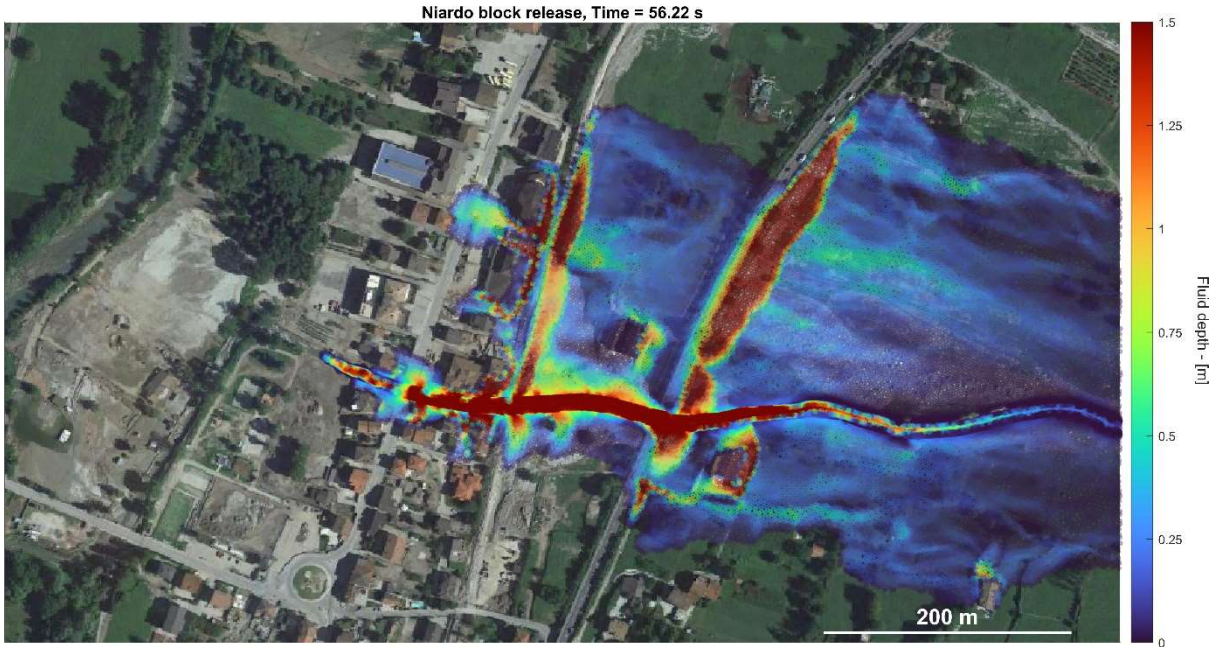
Niardo block release, Time = 56.22 s
200 m
1.5
1.25
1
0.75
0.5
0.25
0
Fluid depth - [m]

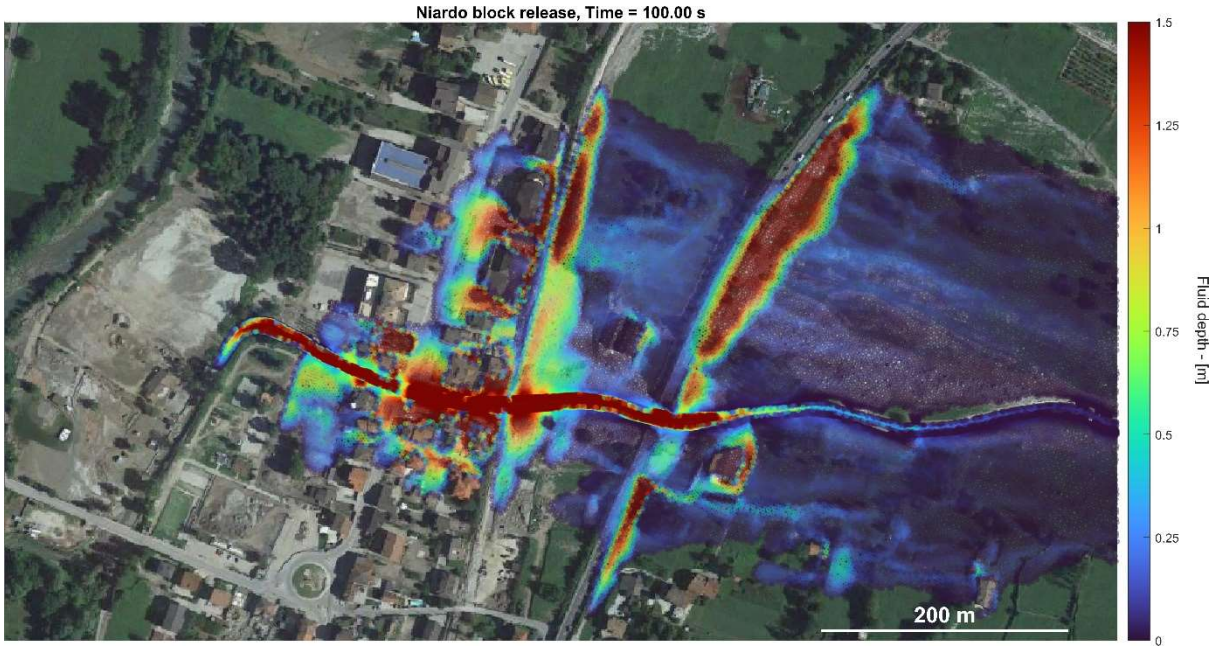

Figure 2.24 Snapshots of the numerical solution computed by DEBRA. Looking at the different images it is possible to observe how the presence of the structures on the topography, i.e. houses, highways and roads, strongly influences the propagation of the flow through the town of Niardo. The maximum depositional height can be observed near the highway and inside the river channel of Re stream, reaching up to 5 m.

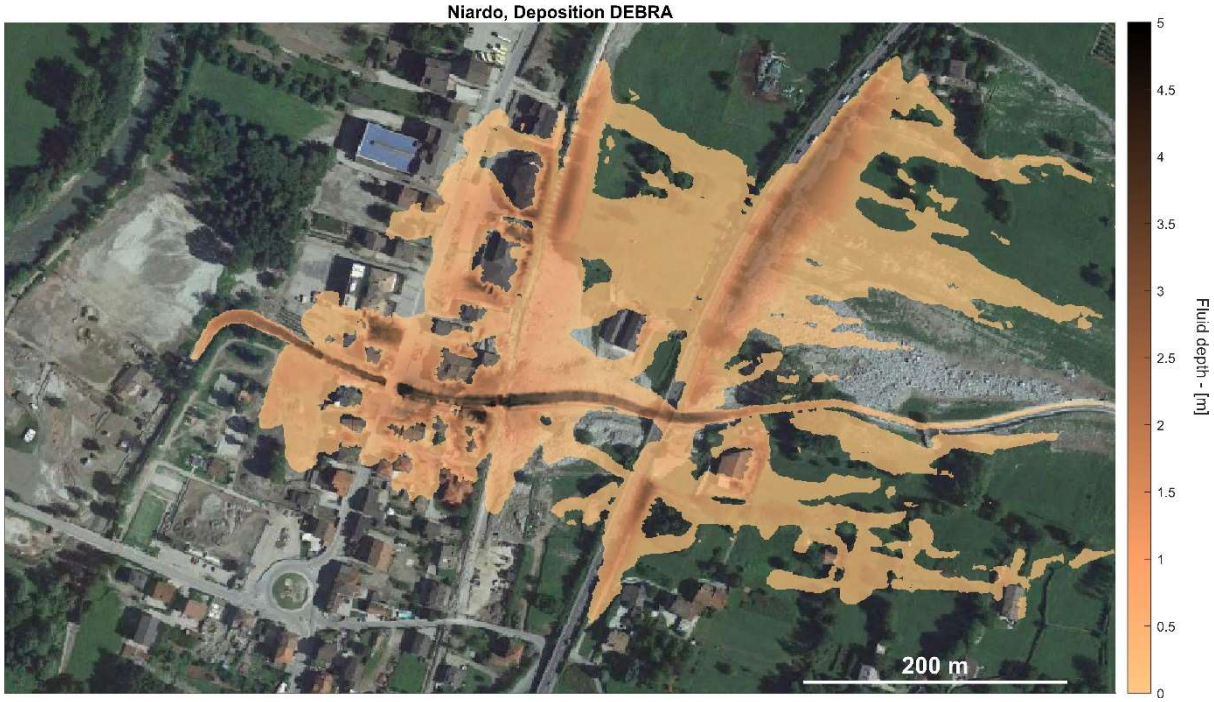

Figure 2.25 Deposition pattern of DEBRA at the end of the simulation.

Figure 2.26 Deposition pattern of RAMMS at the end of the simulation.

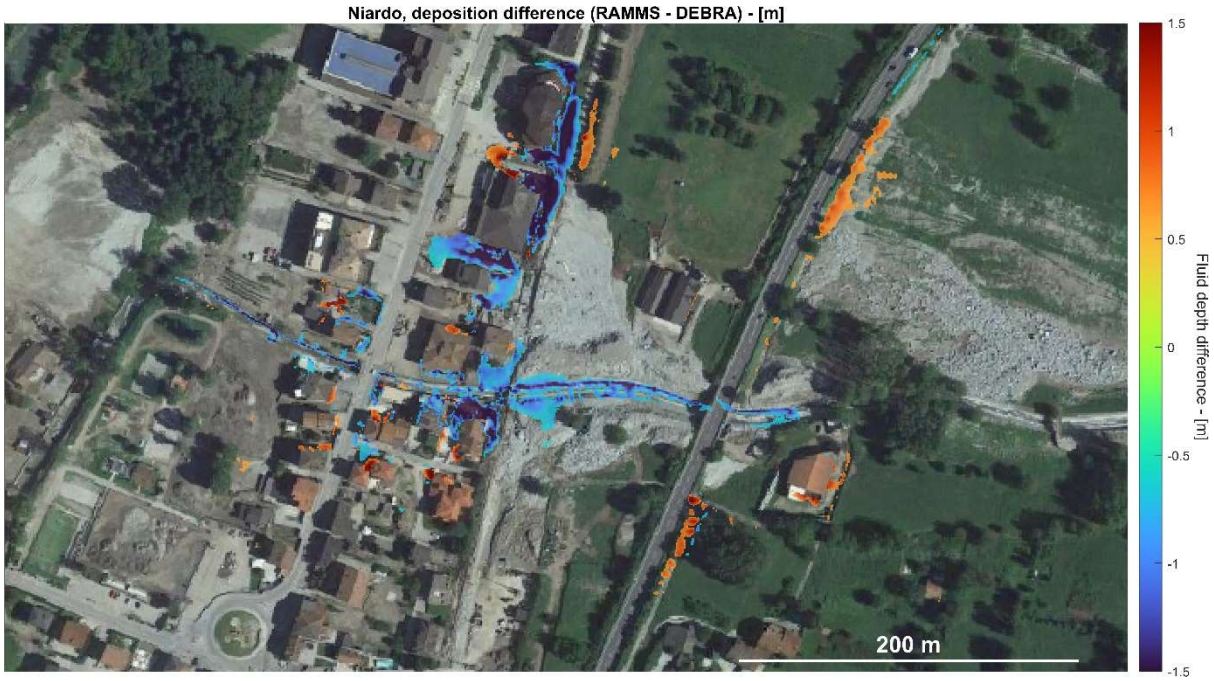

Figure 2.27 Deposition difference between RAMMS and DEBRA at the end of the simulation. For a clearer picture differences in absolute value less than 0.3 m are not displayed.

In Figure 2.24 it is possible to visualize several simulation snapshots provided by DEBRA at different time steps. It is clear how the bathymetry strongly influences the path of the flow, in particular the railway bridge, acting as a dam to the flow and causing deposition. Having overcome the railway bridge, the flow continued to propagate across one of the main roads of Niardo, eventually stopping after a 90° turn, following the morphology of the area. Laterally, the flow expands and deposits near the highway which passes through Niardo. Using the same initial conditions and parameters, the same simulation is performed also using RAMMS

allowing a direct comparison of the depositional height at the end of the simulation. In Figures 2.25 and 2.26 the deposition maps are displayed. Even though the general trend is the same in both maps, there are some inconsistencies which need to be underlined and addressed. Figure 2.27 helps to better visualize this issue, where the difference between the deposition computed by RAMMS and the deposition computed by DEBRA is displayed. To enhance the quality of the map, every difference (in absolute value) less than $0.3\ m$ is not depicted. The maximum differences across the whole map are around $2\ m$ near the channel of Re stream, which can be explained by the different kind of mesh and discretization adopted. In DEBRA the channel is modelled with a higher accuracy with respect to RAMMS, thanks to the adoption of the unstructured mesh. This leads to a higher deposition in DEBRA, thus the blue/light blue colour inside the channel. Other differences can be found near the houses in the northern part of Niardo where RAMMS predicts much lower depositional height. Finally it is worth noting that both models agree on the maximum propagation extend in all directions, in particular the 90° bend where the match is very good, although the debris flow in DEBRA is more homogeneously distributed. A qualitative comparison between both depositional maps of the numerical models and the observed map reveals that the behaviour of the occurred debris flow was in fact very different but this is not relevant considering the comparative role of the present numerical test on a real bathymetry to assess the potential differences between the two mathematical and numerical models. First the deposited material extended much less in the area upstream the railway bridge, just barely touching the house located between the railway and the highway. Therefore the simulation with the block release initial condition with the described parameters seems unsuitable to replicate the debris flow that effectively occurred in Niardo. It is evident from the observed deposition that the flow, initially, was entirely channelled inside the Re stream.

2.4.4.2 Solid discharge boundary condition

Another possible way to simulate a debris flow is the imposition of a solid discharge hydrograph at a given inlet, aiming to reproduce an event with similar characteristics to a flood, i.e. starting from a channel. In flood related applications, fixing a discharge boundary condition requires the knowledge of the kind of flow being modelled, i.e. supercritical or subcritical, depending on local flow characteristics. Using this knowledge, it is customary to introduce a stage discharge curve from which, for each assigned discharge value, it is possible to compute a uniform fluid depth. Although the identification of a stage discharge relationship in presence of granular flow is difficult to estimate, simply by using the relation provided by Hergarten & Robl (2015), one obtains a $u(h)$, i.e. the terminal or uniform velocity as a function of the fluid depth, which can be used to obtain the discharge. Inverting eq. (2.58) leads to

$$\bar{h} = \left(\frac{Q}{L\sqrt{\xi \sin\vartheta - \mu \cos\vartheta}} \right)^{2/3} \tag{2.70}$$

where $\bar{h}$ is the fluid depth measured normally with respect to the bottom bed, Q is the discharge, L is the channel width while μ and ξ are the Voellmy's friction law parameters.

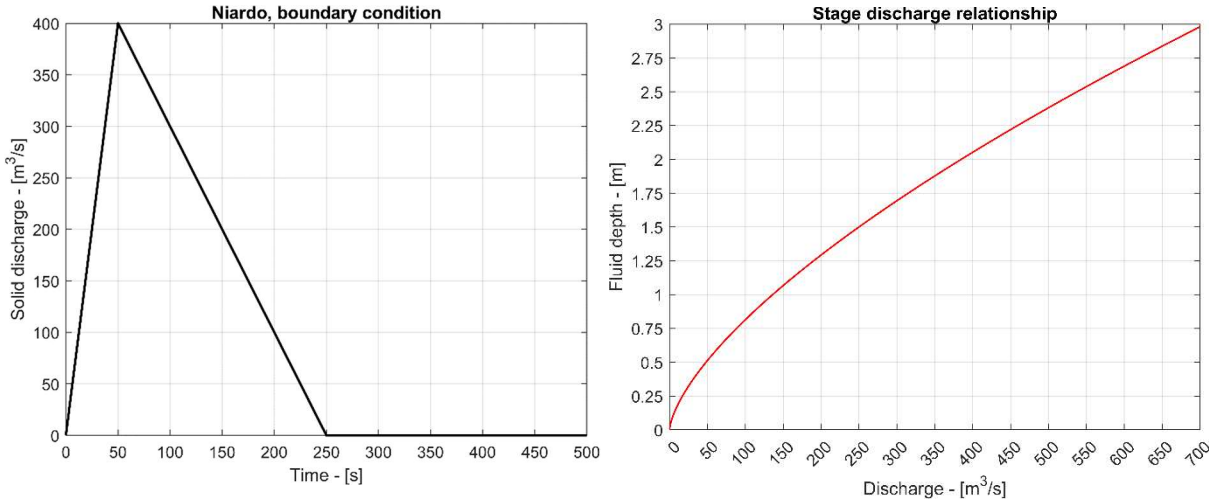

Figure 2.28 (Left) Solid discharge hydrograph used to simulate the event of Niardo. Following local testimonies, the event has been assumed to be very quick, reaching the peak discharge in 50 s, for a total volume of 50 000 m^3 of sediments. (Right) Stage discharge relationship for the assumed cross section in Niardo, obtained using eq. (2.70) using $\vartheta = 30°, L = 10\ m$, $\mu = 0.15$ and $\xi = 500\ m/s^2$.

DEBRA uses the curve reported in Figure 2.28 (right) to dynamically assign a fluid depth for the incoming discharge. At each time step, if the flow is in supercritical regime, both fluid depth and flow velocity are imposed while only the water depth is imposed if the regime is subcritical. The inlet slope ϑ is a parameter which influences the regime in which the flow enters in the domain, in this application, an average slope of the channel has been considered. The chosen Voellmy's rheological parameters used to model the hydrograph and the debris flow are the ones which best reproduced the observed depositional pattern in Niardo.

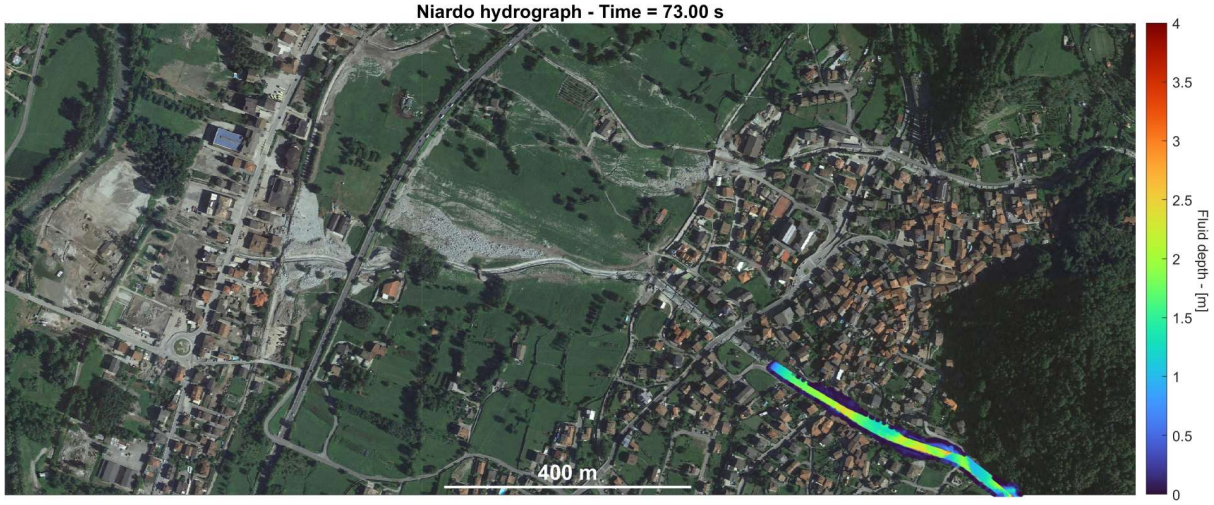

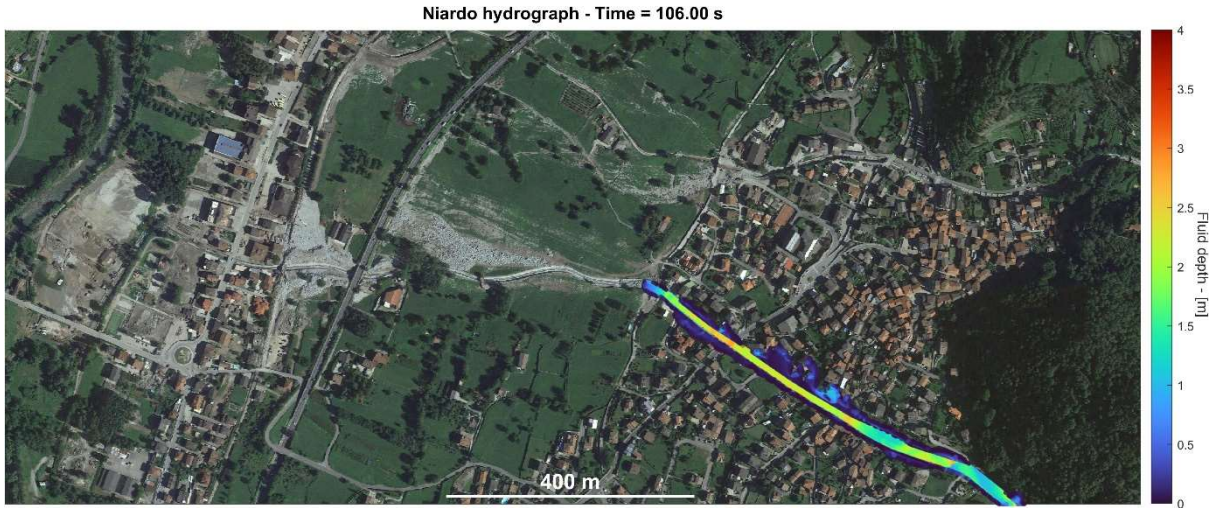
Niardo hydrograph - Time = 106.00 s
400 m
Fluid depth - [m]
0
0.5
1
1.5
2
2.5
3
3.5
4

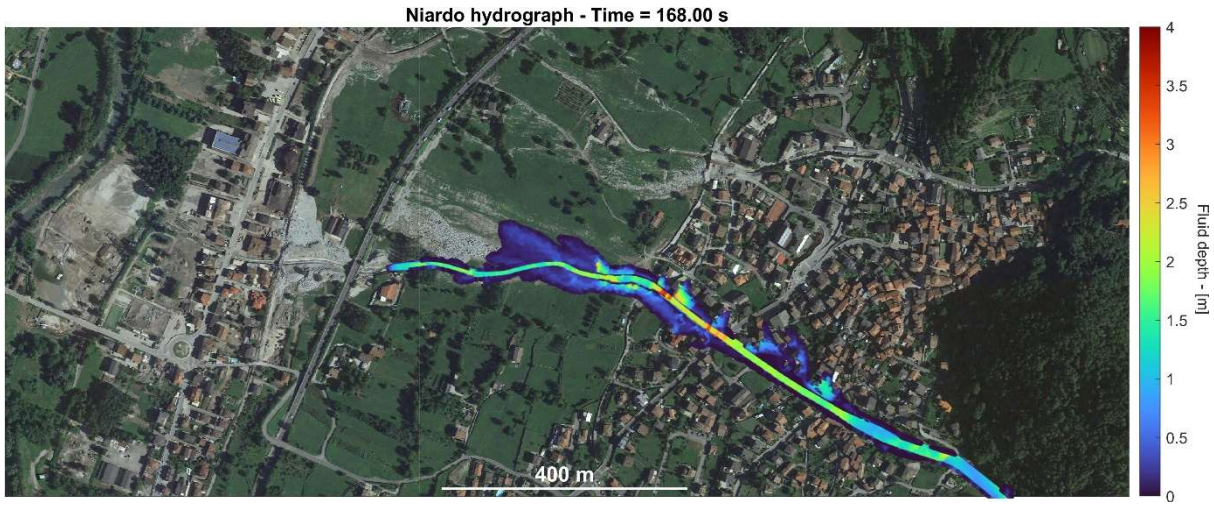
Niardo hydrograph - Time = 168.00 s
400 m
Fluid depth - [m]
0
0.5
1
1.5
2
2.5
3
3.5
4

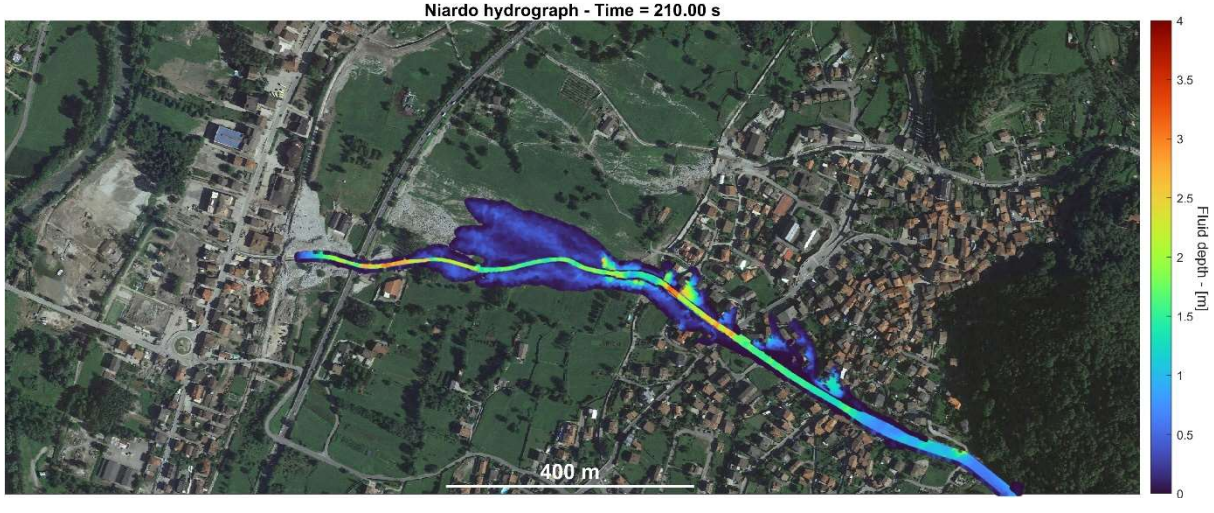
Niardo hydrograph - Time = 210.00 s
400 m
Fluid depth - [m]
0
0.5
1
1.5
2
2.5
3
3.5
4

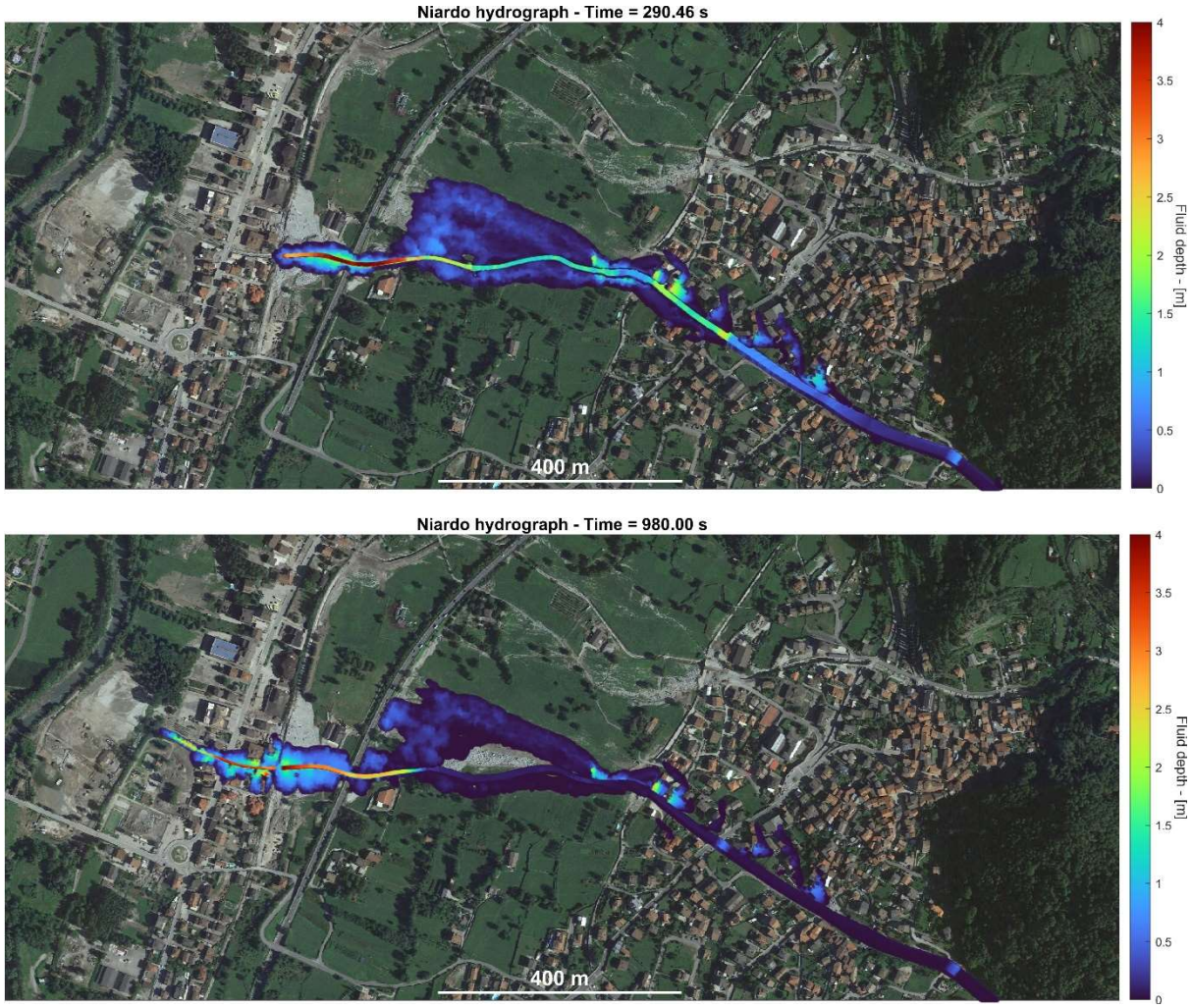

Figure 2.29 Series of simulation snapshots computed by DEBRA. Thanks to the hydrograph boundary condition, now the flow propagates entirely through the channel. The presence of the obstructed bridge allows to better capture the deposition pattern near the railway.

In Figure 2.29 it is possible to see the propagation of the debris flow using the hydrograph boundary condition computed by DEBRA. According to the stopping criteria described previously, the debris flow stops its propagation after around 980 s. The deposition pattern is now much more similar to the observed one in Niardo after the event. It was observed that the channel portion between the railway and the highway was filled completely by debris after the event. The channel is around 5 m deep, and DEBRA predicts a deposition in that area of around 4.5 m. Furthermore, from Figure 2.29, it is possible to notice how the observed deposition pattern and the output of DEBRA are similar in the area located downstream the historical part of Niardo. Still, in the historical part of Niardo, DEBRA predicts that some flooding occurred while in reality it was observed that the debris flow did not overflow. The reason behind this inconsistency, in the author's opinion, can be attributed either to the poor quality of the digital elevation model present in that area, which may reduce its conveyance and lead to overflow, or an incorrect estimate of the incoming hydrograph or its shape. Unfortunately, the absence of information about the event complicates the modelling process.

2.5 References

Ata, R., Pavan, S. Khelladi, S., Toro, E. F. (2013). A Weighted Averaged Flux (WAF) scheme applied to shallow water equations for real-life applications, Advances in Water Resources, 62, 10.1016/j.advwatres.2013.09.019.

Bonomelli, R., Farina, G., Pilotti, M., Molinari, D., Ballio, F. (2023) Historical comparison of the damage caused by the propagation of a dam break wave in a pre-alpine valley, Journal of Hydrology: Regional Studies, 48, 101467, 10.1016/j.ejrh.2023.101467.

Christen, M., Kowalski, J., Bartelt, P. (2010). RAMMS: Numerical simulation of dense snow avalanches in three-dimensional terrain. Cold Regions Science and Technology, 63, 1-14, 10.1016/j.coldregions.2010.04.005.

FLO-2D Software: Hydrologic and Hydraulic Modeling Software. FLO2D Software. http://www.flo-2d.com/

Frank, F., McArdell, B. W., Oggier, N., Baer, P., Christen, M., Vieli, A. (2017). Debris-flow modeling at Meretschibach and Bondasca catchments, Switzerland: sensitivity testing of field-data-based entrainment model, Nat. Hazards Earth Syst. Sci., 17, 801–815, 10.5194/nhess-17-801-2017.

Hergarten, S., Robl, J. (2015). Modelling rapid mass movements using the shallow water equations in cartesian coordinates. Nat. Hazards Earth Syst. Sci. 2015, 15. 671-685, 10.5194/nhess-15-671-2015.

Hou, J. Simons, F. Mahgoub, M., Hinkelmann, R. (2013). A robust well-balanced model on unstructured grids for shallow water flows with etting and drying over complex topography, Computer Methods in applied Mechanics and Engineering, 257, 126-149, doi.org/10.1016/j.cma.2013.01.015.

Iverson, R. M. (1997). The physics of debris flows. Reviews of Geophysics 35, 245-296.

Leonardi, A., Cabrera, M., Wittel, F. K., Kaitna, R., Mendoza, M., Wu, W., Herrmann, H. J., (2015). Granular-front formation in free-surface flow of concentrated suspensions. Physical Review E, 92, 052204, 10.1103/PhysRevE.92.052204.

Leer, B. (1979). Towards the ultimate conservative difference scheme. V. A. second-order sequel to Godunov's method, Journal of Computational Physics, 32, 1, 10.1016/0021-9991(79)90145-1.

LeVeque, R. (2002). Finite Volume Methods for Hyperbolic Problems (Cambridge Texts in Applied Mathematics). Cambridge University Press. doi:10.1017/CBO9780511791253.

Loukili, Y., Soulaimani, A. (2007). Numerical tracking of shallow water waves by the unstructured finite volume WAF approximation, Internal Journal of Computational Methods in Engineering Science and Mechanics,75-88, 10.1080/15502280601149577.

Mangeney, A., Heinrich, P., Roche, R. (2000). Analytical solution for testing debris avalanche numerical models. Pure and Applied Geophysics, 157, 1081-1096, 10.1007/s000240050018.

Maranzoni, A., Tomirotti, M. (2022). New formulation of the two dimensional steep-slope shallow water equations. Part I: Theory and analysis. Advances in Water Resources, 166, 104255, doi.org/10.1016/j.advwatres.2022.104255.

Maranzoni, A., Tomirotti, M. (2023). New formulation of the two dimensional steep-slope shallow water equations. Part II: Numerical modeling, validation and application. Advances in Water Resources, 177, 104403, doi.org/10.1016/j.advwatres.2023.104403.

Medina, V., Bateman, A., Hurlimann, M. (2008). A 2D finite volume model for debris flow and its application to events occurred in the Eastern Pyrenees. International Journal of Sediment Research, 23, 4, S1001-6279(09)60006-8.

O'Brien, J. S., Julien, P. Y. (1988). Laboratory analysis of mudflow properties. Journal of Hydraulic Engineering, 114, 8.

O'Brien, J. S., Julien, P. Y., Fullerton, W. T. (1993). Two dimensional water flood and mudflow simulation, Journal of Hydraulic Engineering, 119, 2.

Pudasaini, S. P., Mergili, M. (2019). A multi-phase mass flow model. Journal of Geophysical Research: Earth Surface, 124, 2920–2942, doi.org/10.1029/2019JF005204.

Rosatti, G., Begnudelli, L. (2012). Two-dimensional simulation of debris flows over mobile bed: Enhancing the TRENT2D model by using a well-balanced Generalized Roe-type solver, Computers & Fluids, 71, 179-195, 10.1016/j.compfluid.2012.10.006.

Stoker, J. J. (1957). Water Waves: The Mathematical Theory with Applications. John Wiley & Sons, 10.1002/9781118033159

Takahashi, T. (1978). Mechanical characteristics of debris flow, Journal of Hydraulic Division, ASCE 104 (8), 1153-1169, 10.1061/JYCEAJ.00050.

Takahashi, T. (2014). Debris Flow Mechanics, Prediction and Countermeasures, 2nd edition, CRC Press Taylor & Francis Group.

Toro, E. F. (2001). Shock-Capturing Methods for Free-Surface Shallow Flows, John Wiley & Sons LTD.

Toro, E. F. (2009). Riemann Solvers and Numerical Methods for Fluid Dynamics: A Practical Introduction. Springer Berlin, Heidelberg 10.1007/b79761.

Toro, E. F. (2019). The HLLC Riemann solver. Shock Waves, 29:1065-1082, 10.1007/s00193-019-00912-4.

Trujillo-Vela, M. G., Ramos-Cañon, A. M., Escobar-Vargas, A. E., Galindo-Torres, S. A. (2022). An overview of debris-flow mathematical modelling, Earth-Science Reviews, 232, 104135, 10.1016/j.earscirev.2022.104135.

US Army Corps of Engineers (2008). HEC-RAS Hydraulic Reference Manual, Hydrologic Engineers Center.

Voellmy, A. (1955). Über die Zerstörungskraft von Lawinen. Schweizerische Bauzeitung, Jahrg. 73, Ht. 12, p. 159-62; Ht. 15, p. 212-17; Ht. 17, p. 246-49; Ht. 19, p. 280–85.

Wu, Y. H., Liu, K. F, Chen, Y. C. (2013). Comparison between FLO-2D and Debris-2D on the application of assessment of granular debris flow hazards with case study. Journal of Mountain Science, 10, 293-304, 10.1007/s11629-013-2511-1.

Yoon, T. H., Kang, S. K. (2004). Finite volume model for two-dimensional shallow water flows on unstructured grids, Journal of Hydraulic Engineering, 130, 7, 10.1061/(ASCE)0733-9429(2004)130:7(678).

Conclusions

The fundamental building blocks of an integrated early warning system for debris flows have been described in the previous chapters. In the first one an integrated hydrologic slope stability model for debris flow inception has been presented. The slope stability model is a variation of the Janbu's method, aiming to improve the described limitations of the IS model. The novel methodology has been validated on simple slopes using the output of a complete equilibrium analysis as ground truth. In all the reported simple cases, the proposed Janbu's method was able to improve the prediction of the unstable areas of the IS model, performing similarly to a complete equilibrium method. The hydrological component of the model has been also discussed and a simple application on a series of conceptualized slopes is presented. Finally, using a well-known study case and dataset located in Coos Bay, Oregon, it was possible to assess the performances of the stability model without incurring in calibration of parameters or data uncertainty, which is an issue which greatly influences the results in any application. This contribution presents an application of the slope stability analysis having fixed the input data and validating it against a known dataset, choosing not to use the mentioned hydrological model to ensure clarity and reproducibility of the results. Further work will address a full-scale application of the proposed coupled methodology (hydrological + slope stability model). The complete application to a case study requires extensive calibration and in-situ measurements which would lead to further discussion. The second chapter focuses instead on the propagation of the debris flow, introducing the finite volume numerical scheme DEBRA (Debris-flow Evolution and Behaviour for Risk Assessment). DEBRA solves the monophasic SSSWE, based on a recently introduced formulation of the SWE on steep terrains (Maranzoni & Tomirotti, 2022). The code works on unstructured grids allowing the user to select multiple friction laws to simulate the evolution of flows which ranges from water to granular material. The numerical scheme has been presented and applied to a selection of test cases both analytical and taken from a recently occurred event. The new formulation solves and improves some limitations intrinsically present inside a standard SWE model, extending the range of applications in which the governing equations are strictly valid. Despite the new advantages of the new SSSWE formulation, further studies must be carried out to shed light on how to rigorously enforce the well balanced property, i.e. also called the C-property, which is the ability possessed by the scheme to preserve the equilibrium state of the flow on uneven terrains in absence of motion. Physically this corresponds to the lake at rest situation, in which the hydrostatic fluxes balance exactly the source term given by the bathymetry. This situation, although less common in debris flows with respect to flood propagation, is very difficult to model numerically and requires special treatment. Existing methodologies often rely either on hydrostatic reconstruction (Audusse & Bristeau, 2005), or in considering the bed slope source term directly inside the fluxes, thus introducing the water elevation as a new variable (Liang & Marche, 2009). Both methodologies preserve the C-property of the underlying numerical scheme and are straightforward to implement on any type of grid. Since the SSSWE are a relatively new formulation, a way to adapt existing methodologies to handle this numerical issue still remains a challenge due to the discontinuous coefficients ϑ_x and ϑ_y present inside the hydrostatic pressure term. Further studies must be carried out in order to develop a method which works also in presence of discontinuous coefficients between the states. Numerical tests confirm that also RAMMS does not satisfy the C-property when challenged using the classical tests available in literature. Modelling the flow of debris flows requires inevitably to consider

entrainment and deposition of the granular material along the path of the flow. Considering the event occurred in Niardo, it is evident from the reported pictures that the flow eroded the channel during the propagation, thus incorporating part of the bed into the flow. Multiple approaches are possible to deal with this phenomenon ranging in complexity, from the static approach suggested by Medina et al. (2008), where a static equilibrium is assumed with the terrain during the flow, or a dynamic approach, where the eroded new material is accelerated to the mean velocity of the flow, in which the quantity of new incorporated mass depends on the availability of momentum (Medina et al., 2008). The introduction of an unstructured grid is an important upgrade which, at the expense of a major complexity, enables on one hand the possibility to follow any structures present along the flow, i.e. houses, roads and existing channels, by the introduction of appropriate break lines, on the other hand ensures a directional isotropy of the grid by construction. DEBRA has been compared with the commercial software RAMMS yielding similar results in simple situations and improving on an analytical case where DEBRA does not show the unphysical oscillatory pattern shown by RAMMS. On the test case of Niardo, using the block release, it is possible to notice some discrepancies between the models, even though the initial conditions and parameters are the same. The reason behind these differences can be attributed, as already stated above, in the kind of mesh adopted, in the different formulation of the governing equations which are solved at each time step and to the reasons that lead to the oscillatory behaviour present inside RAMMS discussed previously. Computational times are another important issue to be tackled, since the Matlab environment clearly offers many advantages in terms of data handling and visualization, avoiding the user to explicitly deal with memory allocation for instance, with the downside of higher computational times in performing numerical tasks. Accordingly, future developments will focus on porting the whole source code into a compiled language for maximum efficiency in terms of computational times.

3.1 Future works

This thesis introduced some novel techniques used to model the inception and propagation of debris flows. Despite being complete, this thesis described the fundamental building blocks of an innovative physically based early warning system for debris flows in mountain regions. The idea is to create a so-called digital twin of a particular catchment (consider for instance the catchment of Re stream, near Niardo) which is able to respond to an external forcing, i.e. rainfall, similarly to the real catchment. To obtain this kind of response some calibration is required which, if the catchment has some gauging station of physically relevant quantities (rainfall, water level, ecc…), can be done using past observations during regular rainfall events. The outflowing discharge history therefore can be used to calibrate the hydrological response of the catchment, similarly, to model the soil stability response of the catchment, one can use the knowledge that during past events no unstable areas have been detected, thus allowing the calibration of the geotechnical parameters that characterize the catchment. Having now a model which behaves similarly to the real one, it is possible to let it run continuously using rainfall forecast as a forcing, in order to detect much in advance if a certain event may cause soil slips inside the catchment. If this is detected then an initial warning can be issued, alerting authorities. Afterwards, if the danger persists, a debris flow model can be used to predict the propagation of the flow in the catchment and whether urbanized areas are at risk of being impacted by the debris flow. Using this modelling chain would in principle extend the warning time sufficiently and reliably by several hours, according to the quality of the rainfall forecast, contrary to currently used methods.

3.2 References

Audusse, E., Bristeau, M. O. (2005). A well-balanced positivity preserving “second-order” scheme for shallow water flows on unstructured meshes. Journal of Computational Physics, 206, 1, 10.1016/j.jcp.2004.12.016.

Liang, Q., Marche, F. (2009). Numerical resolution of well-balanced shallow water equations with complex source terms. Advances in Water Resources, 32, 873-884, 10.1016/j.advwatres.2009.02.010.

Maranzoni, A., Tomirotti, M. (2022). New formulation of the two dimensional steep-slope shallow water equations. Part I: Theory and analysis. Advances in Water Resources, 166, 104255, doi.org/10.1016/j.advwatres.2022.104255.

Medina, V., Bateman, A., Hurlimann, M. (2008). A 2D finite volume model for debris flow and its application to events occurred in the Eastern Pyrenees. International Journal of Sediment Research, 23, 4, S1001-6279(09)60006-8.

Appendix A

Equivalence of the Janbu method and the IS model for a single slice slope

The Janbu method and the IS model furnish the same safety factor if the slope under investigation is made just by one slice. To prove this consider a slope made just by one slice and write eq. (1.15) setting $n = 1$:

$$FS = \frac{\{c'\, a + [N(FS) - u\, a + k_0 h(\gamma_s h - \gamma_w r)\Delta x \cos^2\beta] \tan\phi' + 2c'_r h\Delta x\} \cos\beta}{N(FS)\sin\beta} \tag{A1}$$

Inserting the expression of $N(FS)$ reported in eq. (1.12) into eq. (A1), after some algebra and using the shorthand $M = c'a - ua\tan\phi' + 2c'_r h\Delta x + k_0(\gamma_s h - \gamma_w r)\, h\, \Delta x \cos^2\beta \tan\phi'$, one obtains:

$$\frac{FS\,(M + G\tan\phi'\cos\beta) - G\,FS^2\sin\beta}{\sin\beta\,(G\,FS - M\sin\beta)} = 0 \tag{A2}$$

which can be reduced to the following equation provided that the denominator does not vanish:

$$M + G\tan\phi'\cos\beta - G\,FS\sin\beta = 0 \tag{A3}$$

by retrieving the safety factor FS:

$$FS = \frac{M + G\tan\phi'\cos\beta}{G\sin\beta} \tag{A4}$$

which is the safety factor of the IS model reported in eq. (1.5) using $G = \gamma_s\, h\, a\cos\beta$, $u = \gamma_w r\cos^2\beta$ and neglecting all lateral contributions.

Appendix B

Monotonicity proof

The proposed Janbu method involves the resolution of the following equation for each block along the slope:

$$FS = \frac{\sum_{i=1}^{n}\{c'\,a_i + [N_i(FS) - u_i\,a_i + k_0(\gamma_s h_i - \gamma_w r_i)h\Delta x\cos^2\beta_i]\tan\phi' + 2c'_r h_i \Delta x\}\cos\beta_i}{\sum_{i=1}^{n} N_i(FS)\sin\beta_i} \tag{B1}$$

This computation can be avoided if one is interested if one wishes only to assess whether the slope is stable ($FS > 1$) or unstable ($FS < 1$). In the present proof each quantity that can vary along the slope is indicated by the pedex i, while constant quantities for the whole slope are unmarked, e.g. ϕ' and c'. The safety factor for any portion of the slope is assumed to be stricktly positive and the base inclination angle is supposed to vary only between $0° < \beta_i < 90°$. By carrying all terms to the right side of the equation:

$$Q(FS) = \frac{\sum_{i=1}^{n}\{c'\,a_i + [N_i(FS) - u_i\,a_i + k_0(\gamma_s h_i^2 - \gamma_w r_i^2)\Delta x\cos^2\beta_i]\tan\phi' + 2c'_r h_i \Delta x\}\cos\beta_i}{\sum_{i=1}^{n} N_i(FS)\sin\beta_i} - FS = 0 \tag{B2}$$

One can say that if the function in eq. (B2) is monotonically decreasing in the interval $[0, +\infty]$ then the quantity $Q(1)$ contains the information about the location of the desired root of eq. (B1). In particular if $Q(1) > 1$ then $FS > 1$, on the other hand, if $Q(1) < 1$ then $FS < 1$. To prove the monotonicity of function (B2), it is sufficient to prove that $Q'(FS) < 0$ in the interval $[0, +\infty]$. First let us recall the expression of the quantity $N_i(FS)$ where the term $M_i = c'a_i - u_i a_i \tan\phi' + 2c'_r h_i\,\Delta x + k_0 h_i(\gamma_s h_i - \gamma_w r_i)\Delta x\cos^2\beta_i \tan\phi'$ is used as a shorthand:

$$N_i(FS) = \frac{G_i \cdot FS - M_i \sin\beta_i}{FS\cos\beta_i + \tan\phi'\sin\beta_i} \tag{B3}$$

By inspection of $N_i(FS)$ one can say that $N_i(FS) > 0$ if $FS > M_i \sin\beta_i\,/G_i$ thus giving a lower bound for the safety factor since the force vector N_i cannot be lower than zero in the present applications. Inserting the expression for N_i reported in eq. (B3) into eq. (B2), one can obtain the following expression after some algebra:

$$Q(FS) = \frac{\sum_{i=1}^{n}\left[\frac{FS\cos\beta_i\,(G_i\tan\phi' + M_i\cos\beta_i)}{FS\cos\beta_i + \tan\phi'\sin\beta_i}\right]}{\sum_{i=1}^{n}\left[\frac{\sin\beta_i(G_i FS - M_i\sin\beta_i)}{FS\cos\beta_i + \tan\phi'\sin\beta_i}\right]} - FS = 0 \tag{B4}$$

which is equivalent to:

$$Q(FS) = \sum_{i=1}^{n} \left[\frac{\cos\beta_i \, (G_i \tan\phi' + M_i \cos\beta_i)}{FS \cos\beta_i + \tan\phi' \sin\beta_i} \right] - \sum_{i=1}^{n} \left[\frac{\sin\beta_i (G_i FS - M_i \sin\beta_i)}{FS \cos\beta_i + \tan\phi' \sin\beta_i} \right] = 0 \qquad \text{(B5)}$$

Differentiating eq. (B5) with respect to FS leads to the equation:

$$Q'(FS) = \sum_{i=1}^{n} \left[-\frac{\cos^2\beta_i \, (G_i \tan\phi' + M_i \cos\beta_i)}{(FS \cos\beta_i + \tan\phi' \sin\beta_i)^2} \right] - \sum_{i=1}^{n} \left[\frac{G_i \sin\beta_i \, (FS \cos\beta_i + \tan'\phi \sin\beta_i) - \sin\beta_i \cos\beta_i \, (G_i FS - M_i \sin\beta_i)}{(FS \cos\beta_i + \tan\phi' \sin\beta_i)^2} \right] \qquad \text{(B6)}$$

Both denominators in eq. (B6) are positive and different from zero in the present application, so by setting $Q'(FS) < 0$ one can say:

$$Q'(FS) = \sum_{i=1}^{n} [-\cos^2\beta_i (G_i \tan\phi' + M_i \cos\beta_i) - G_i \sin\beta_i \, (FS \cos\beta_i + \tan\phi' \sin\beta_i) + \sin\beta_i \cos\beta_i \, (G_i FS - M_i \sin\beta_i)] < 0 \qquad \text{(B7)}$$

If the quantity in eq. (B7) is satisfied slice by slice, i.e. for every index i, then it is true for the sum and therefore for the whole slope. By rearranging the terms inside the summation sign in eq. (B7):

$$-G_i \tan\phi' \cos^2\beta_i - M_i \cos^3\beta_i - G_i \tan\phi' \sin^2\beta_i - M_i \sin^2\beta_i \cos\beta_i < 0 \qquad \text{(B8)}$$

Eq. (B8) is always satisfied provided that $M_i > 0$, which means:

$$c' a_i + 2c'_r h_i \, \Delta x + k_0 \gamma_s h_i^2 \Delta x \cos^2\beta_i \tan\phi' > u_i a_i \tan\phi' + k_0 \gamma_w r_i^2 \Delta x \cos^2\beta_i \tan\phi' \qquad \text{(B9)}$$

The term $k_0 h_i (\gamma_s h_i - \gamma_w r_i) \Delta x \cos^2\beta_i \tan\phi'$ is either positive or equal to zero in the present application, however $M_i < 0$ can still occur, in that scenario the following relation must hold:

$$M_i \cos^3\beta_i + M_i \sin^2\beta_i \cos\beta_i < G_i \tan\phi' \qquad \text{(B9)}$$

which is equivalent to:

$$\frac{G_i \tan\phi'}{M_i \cos\beta_i} > 1 \qquad \text{(B10)}$$

By replacing $G_i = \gamma_s h_i a_i \cos\beta_i$ and $M_i = u_i a_i \tan\phi' = \gamma_w r_i a_i \cos^2\beta_i \tan\phi'$, meaning that no cohesion term is present (neither basal or lateral) together with completely saturated soil ($r_i = h_i$ and $\gamma_s = \gamma_{sat}$), without loss of generality one can say:

$$\gamma_{sat} > \gamma_w \cos^2 \beta_i \tag{B11}$$

which is always true provided that $\gamma_{sat} > \gamma_w$.

Appendix C

Approximate solution for the Janbu method

A possible alternative to solve the full Janbu equation by means of an iterative Newton Raphson method is to use an explicit estimate for the location of the root of eq. (15) in chapter 1. Starting from eq. (B5) reported below for clarity:

$$Q(FS) = \sum_{i=1}^{n} \left[\frac{\cos\beta_i \, (G_i \tan\phi' + M_i \cos\beta_i)}{FS\cos\beta_i + \tan\phi' \sin\beta_i} \right] - \sum_{i=1}^{n} \left[\frac{\sin\beta_i (G_i FS - M_i \sin\beta_i)}{FS\cos\beta_i + \tan\phi' \sin\beta_i} \right] = 0 \qquad \text{(C1)}$$

where $M_i = c' a_i - u_i a_i \tan\phi' + 2c'_r h_i \, \Delta x + k_0(\gamma_s h_i^2 - \gamma_w r_i^2)\Delta x \cos^2\beta_i \tan\phi'$. It is possible to rewrite the denominators as:

$$Q(FS) = \sum_{i=1}^{n} \left[\frac{(G_i \tan\phi' + M_i \cos\beta_i)}{FS + \tan\phi' \tan\beta_i} \right] - \sum_{i=1}^{n} \left[\frac{\tan\beta_i (G_i FS - M_i \sin\beta_i)}{FS + \tan\phi' \tan\beta_i} \right] = 0 \qquad \text{(C2)}$$

One can notice that the denominators in both terms are exactly the same, and if β_i varies very little along the slope considered, or varies very smoothly, one can say that $\tan\beta_i \approx \tan\tilde{\beta}$ only in the denominator term, where $\tilde{\beta}$ is a constant quantity along the slope, therefore the following step is valid:

$$Q(FS) = \frac{1}{FS + \tan\phi' \tan\tilde{\beta}} \left\{ \sum_{i=1}^{n} [G_i \tan\phi' + M_i \cos\beta_i] - \sum_{i=1}^{n} [\tan\beta_i (G_i FS - M_i \sin\beta_i)] \right\} = 0 \qquad \text{(C3)}$$

Simplifying the common term leads to:

$$Q(FS) = \sum_{i=1}^{n} [G_i \tan\phi' + M_i \cos\beta_i] - \sum_{i=1}^{n} [\tan\beta_i (G_i FS - M_i \sin\beta_i)] = 0 \qquad \text{(C4)}$$

Eq. (C4) can be rearranged to give a simple explicit estimate for the safety factor FS:

$$FS = \frac{\sum_{i=1}^{n} [G_i \tan\phi' + M_i \cos\beta_i + M_i \sin\beta_i \tan\beta_i]}{\sum_{i=1}^{n} [G_i \tan\beta_i]} \qquad \text{(C5)}$$

Appendix D

Validation test cases for DEBRA using the classical SWE formulation

D.1 Stoker dam break problem

The dam break problem over a wet bed, also called Stoker problem (1957), allows the validation of the shock-capturing capabilities of the proposed scheme. The domain is 100 m long and 10 m wide, discretized using 57 916 triangles having a maximum edge length of 0.2 m. The CFL condition is fixed at 0.9 during the simulation. Figure D1.1 shows a comparison of the analytical solution provided by Stoker and the computed numerical solution at different times. Initial conditions are defined by water depths of 10 m and 5 m respectively upstream and downstream.

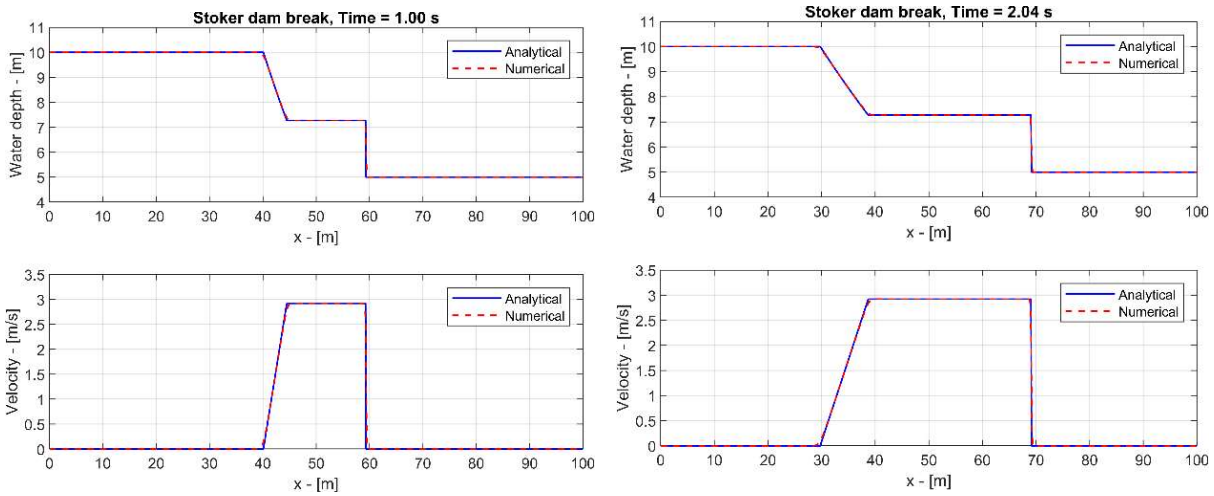

Figure D1.1 Comparison between the analytical and the numerical solution of the Stoker dam break case. Cross sections of the 2D numerical domain are extracted at $y = 2.5\ m$. The initial discontinuity in the water depth is located at $x = 50\ m$.

D.2 Ritter dam break problem

The dam break problem over a dry bed, also called Ritter problem (1892), assesses the capabilities of the numerical scheme to handle wet/dry frontiers that may develop in flood propagation analysis. The same numerical domain and mesh has been adopted with respect to

the previous case. As customary in any explicit numerical scheme, a cutoff threshold to distinguish between wet and dry cells is set to $10^{-10}\ m$ for this test case.

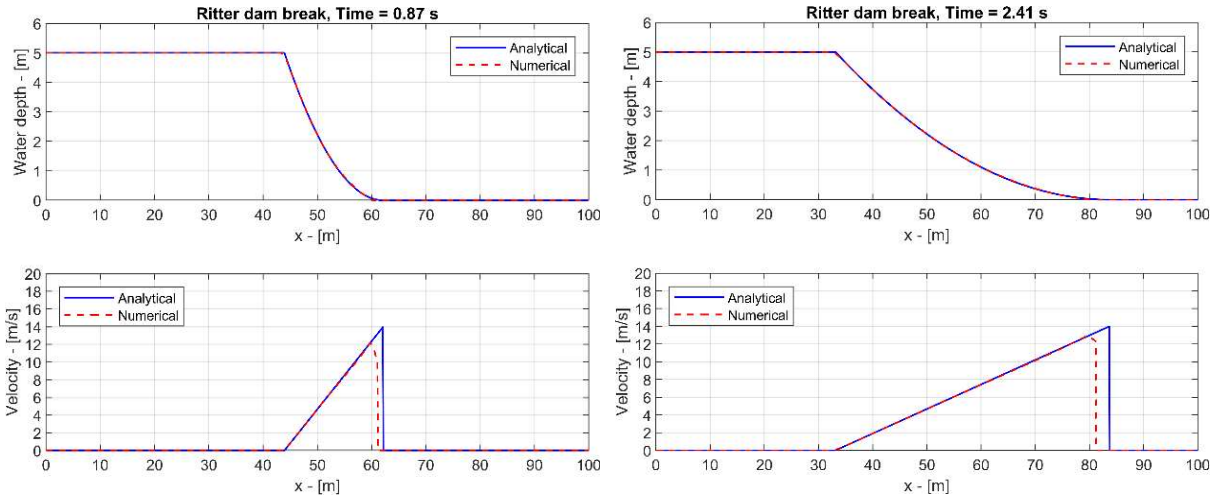

Figure D2.1. Comparison between the analytical and the numerical solution of the Ritter dam break case. Cross sections of the 2D numerical domain are extracted at $y = 2.5\ m$. The initial discontinuity in the water depth is located at $x = 50\ m$.

D.3 Radially symmetrical paraboloid

The two-dimensional case presented here is a radially symmetrical oscillating paraboloid, also presented in Delestre et al. (2016). Thacker (1981) and Sampson (2006) proposed an analytical solution which is periodic in time (without damping, i.e. no friction) with moving wet/dry transitions. A hump of water oscillates expanding towards the edges of the boundary and then contracting into the center. The topography is a paraboloid of revolution defined by:

$$z(r) = -h_0\left(1 - \frac{r^2}{a^2}\right) \tag{D3.1}$$

$$r = \sqrt{(x-2)^2 + (y-2)^2}$$

Which is valid inside the domain defined by (x, y) in $[0; L] \times [0; L]$, where h_0 is the water depth at the central point of the domain in correspondence of a zero elevation and a is the distance from the central point to the zero elevation of the shoreline. The analytical solution is given by:

$$h_a(r,t) = h_0\left[\frac{\sqrt{1-A^2}}{1-A\cos(\omega t)} - 1 - \frac{r^2}{a^2}\left(\frac{1-A^2}{(1-A\cos(\omega t))^2} - 1\right)\right] - b(r)$$

$$u_a(x,y,t) = \frac{1}{1-A\cos(\omega t)}\left[\frac{1}{2}\omega(x-2)A\sin(\omega t)\right] \qquad \text{(D3.2)}$$

$$v_a(x,y,t) = \frac{1}{1-A\cos(\omega t)}\left[\frac{1}{2}\omega(y-2)A\sin(\omega t)\right]$$

Where the frequency ω is defined as $\omega = \sqrt{8gh_0/a}$, r_0 is the distance from the central point to the point where the shoreline is initially located (see figure D3.1) and $A = (a^2 - r_0^2)/(a^2 + r_0^2)$. In this application it has been selected $a = 1\,m$, $r_0 = 0.8\,m$, $h_0 = 0.1\,m$, $L = 4\,m$. The initial condition is given by the analytical solution at $t = 0$.

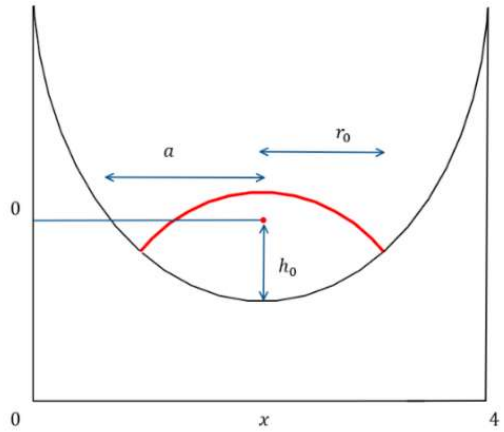

Figure D3.1 Notation used for the radially symmetrical paraboloid.

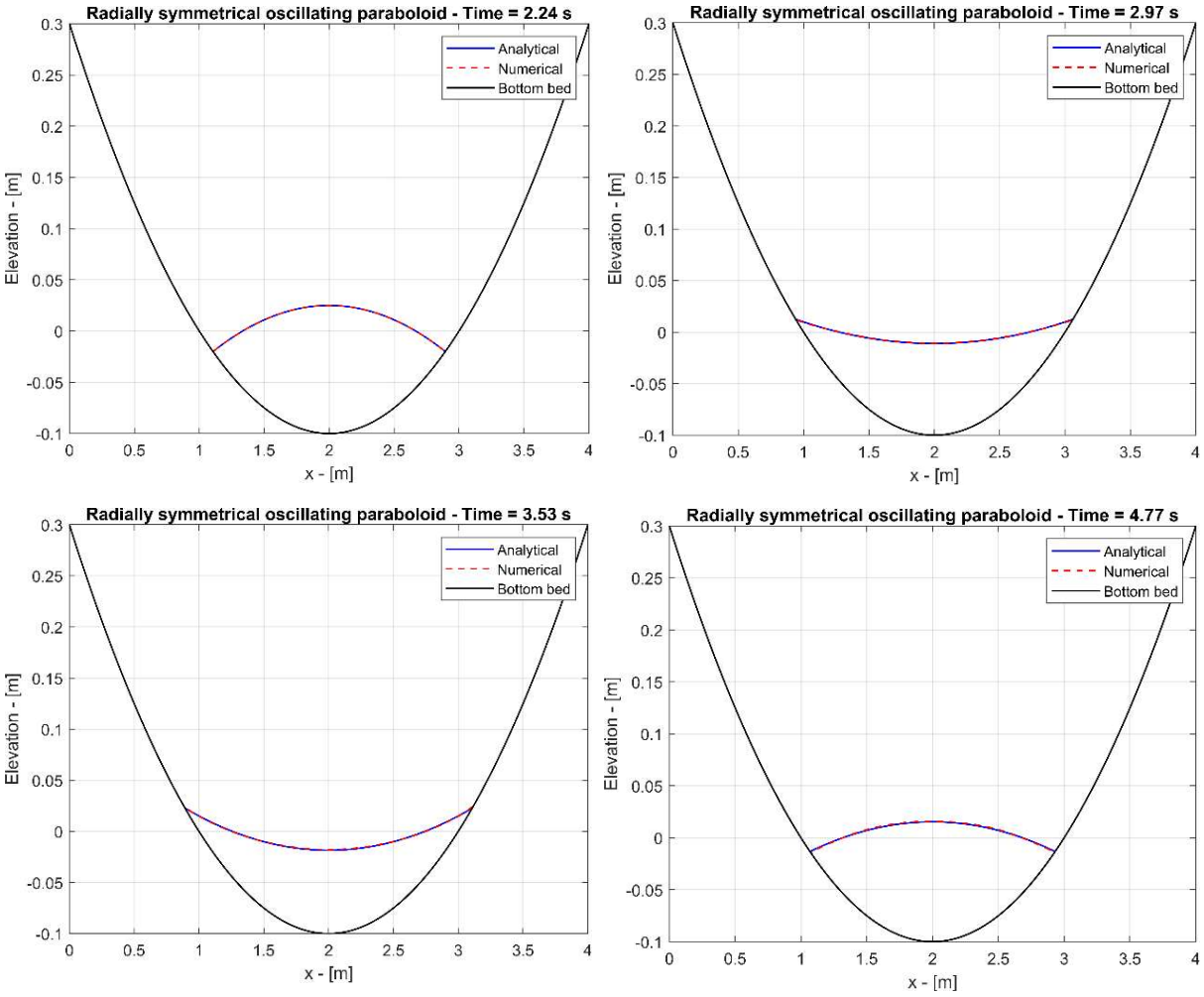

Figure D3.2. Comparison between the analytical and the numerical solution of the Thacker test case at different times. The motion is characterized by a period of 2.24 seconds.

D.4 Malpasset dam break

The last example chosen to test the capabilities of the proposed numerical scheme is the well-known Malpasset dam break. The Malpasset dam is located on the Reyran River, north of Frejus on the French Riviera. A report by Goutal (1990) contains the topography of the floodplain and the storage level of the reservoir at the moment of the collapse. The propagation of the dam break flow has been modelled using 32 676 cells as shown in Figure D4.1, while the Manning coefficient is set to $0.033\ s/m^{1/3}$ as reported by many authors (e.g. Zhao et al. 2019). The boundaries of the domain are all solid walls with the exception of the downstream one near the sea which is transmissive. Experimental work was carried out by Electricité de France to measure maximum water level at the gauge points and the police points, allowing the validation of the numerical scheme.

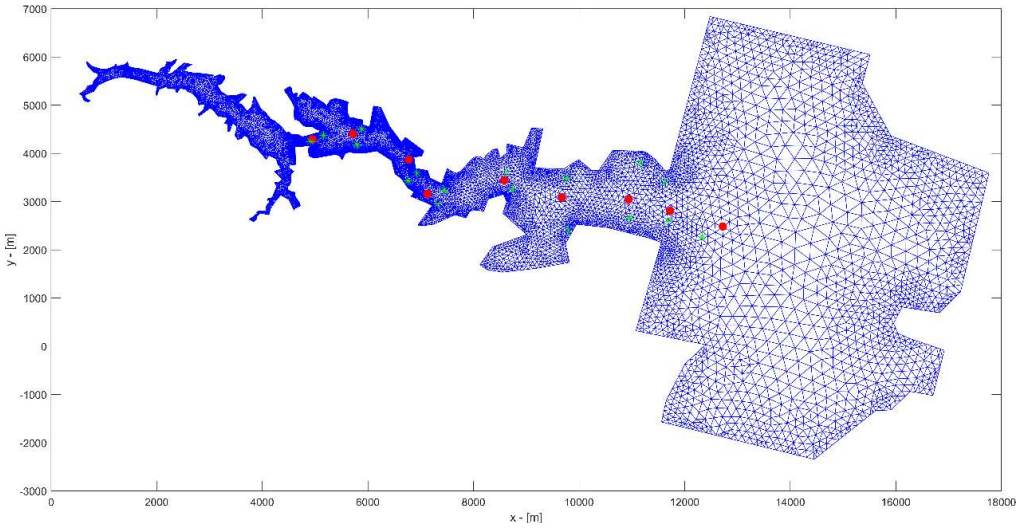

Figure D4.1. Visualization of the computational mesh, the red dots indicate the location of the points surveyed by the police while the green marks highlight the position of the gauge points in the laboratory experiment.

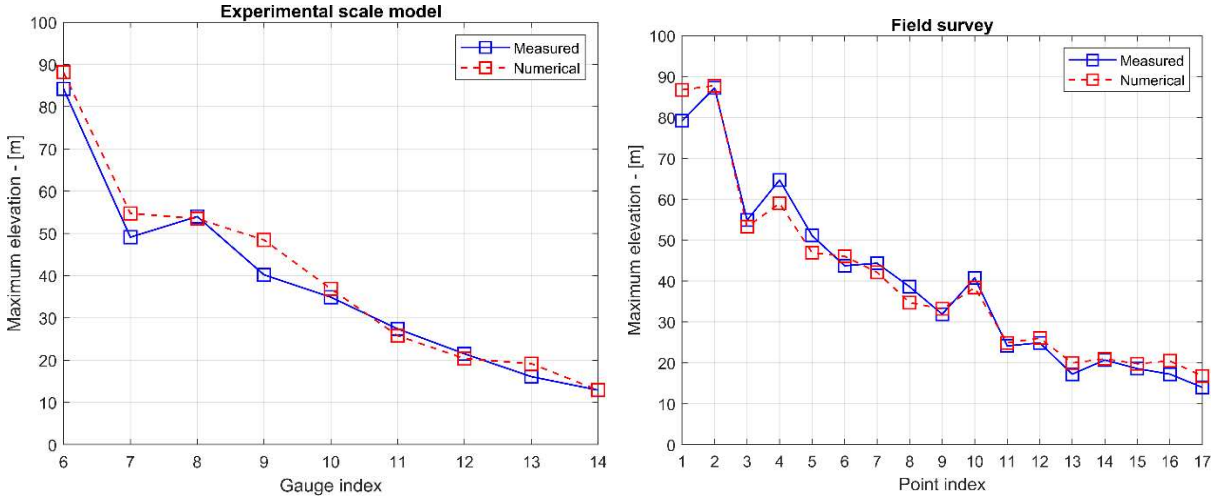

Figure D4.2. (Left) Maximum water levels at experiment gauges. (Right) Maximum water levels at survey points.

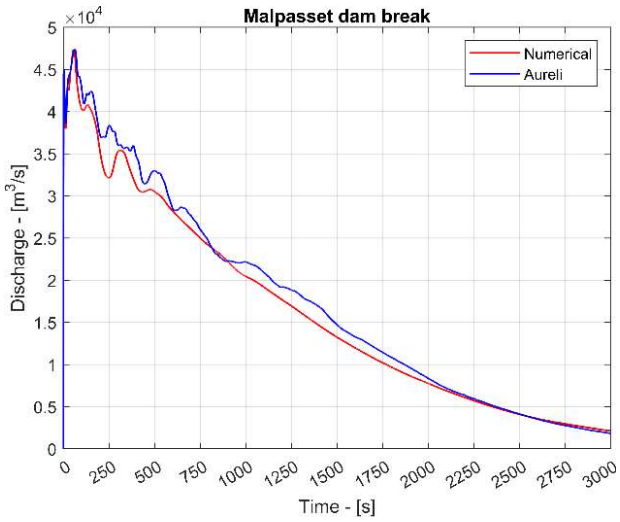

Figure D4.3. Comparison of the dam break discharge at the location of the dam between the proposed numerical scheme (in red) and the numerical scheme showed in Aureli et al. 2014 (in blue).

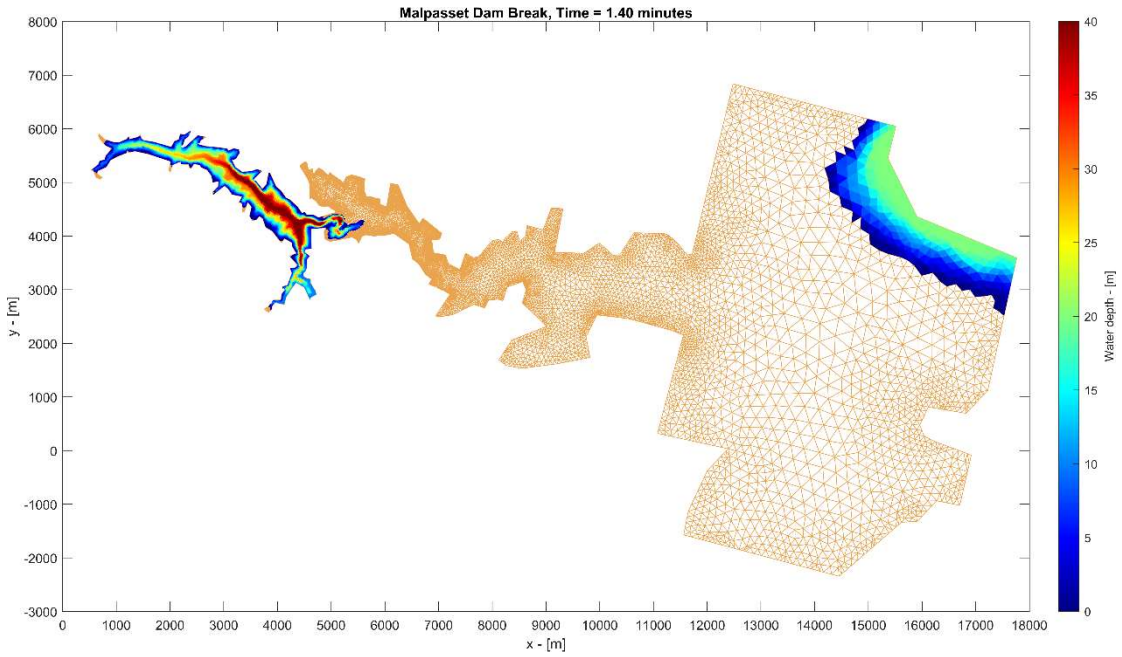

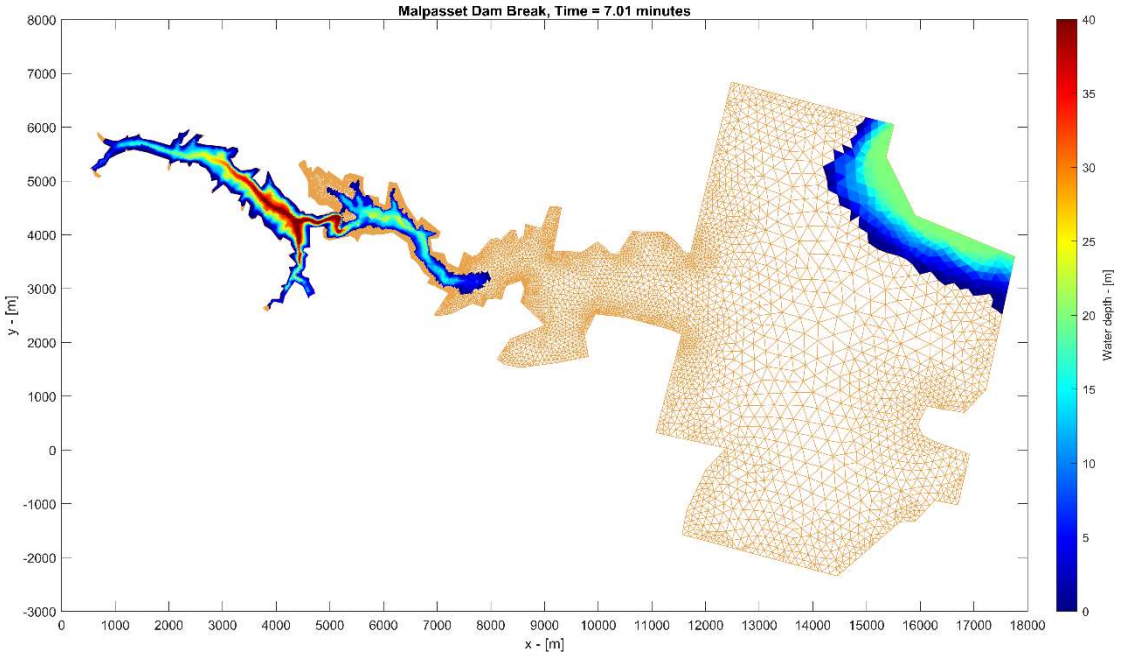
Malpasset Dam Break, Time = 7.01 minutes
y - [m]
x - [m]
Water depth - [m]

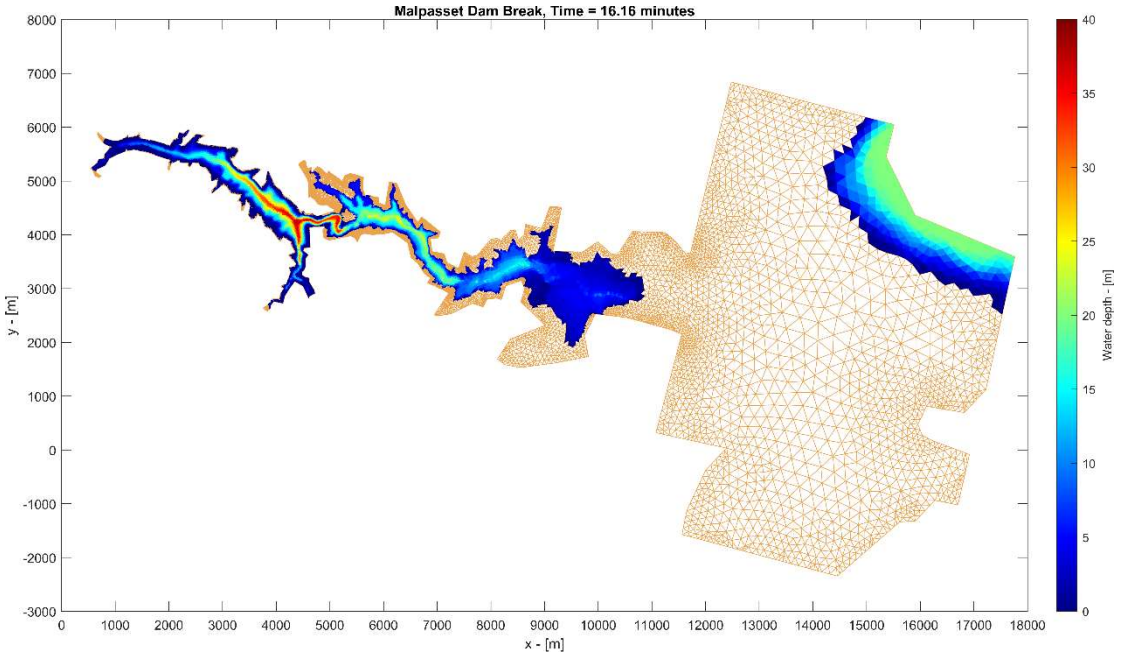
Malpasset Dam Break, Time = 16.16 minutes
y - [m]
x - [m]
Water depth - [m]

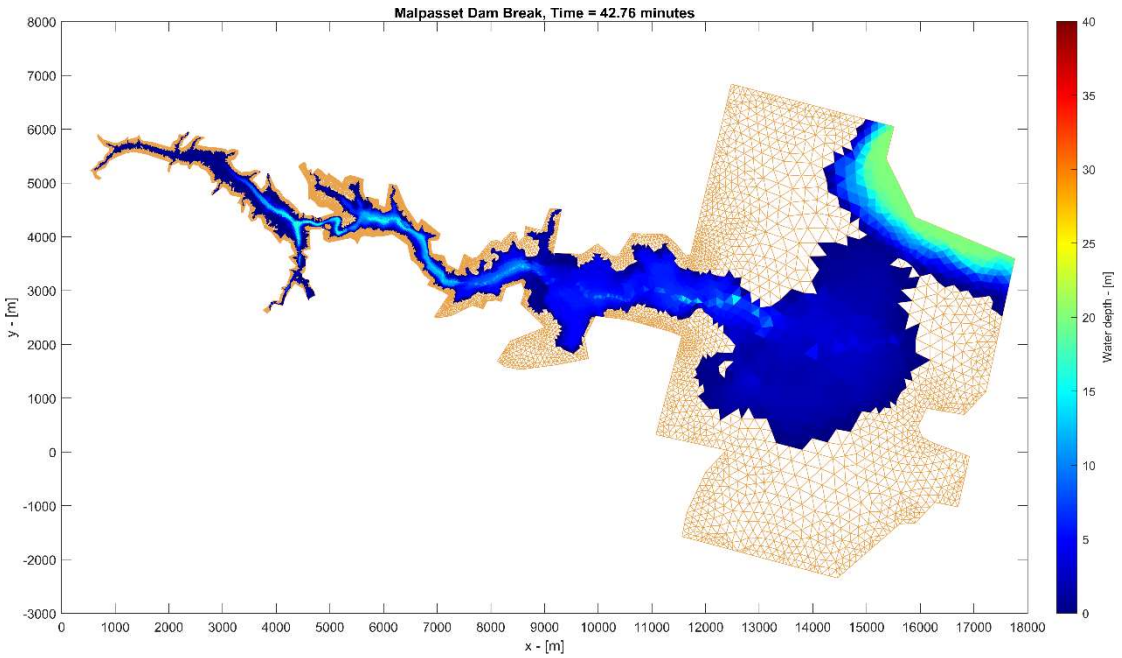

Figure D4.4. Predicted water depth map at various time steps after the collapse of the Malpasset dam.

D.5 References

Aureli, F., Maranzoni, A., Mignosa, P. (2014). A semi-analytical method for predicting the outflow hydrograph due to dam-break in natural valleys, Advances in Water Resources, Volume 63, p 38-44.

Delestre, O., Lucas, C., Ksinant, P. A., Darboux, F., Laguerre, C., James, F. & Cordier, S. (2016). SWASHES: a compilation of shallow water analytic solutions for hydraulic and environmental studies. International Journal for Numerical Methods in Fluids, 2013, 72 (3), pp.269-300.

Goutal N. (1990). The Malpasset dam failure. An overview and test case definition in: Proceedings of CADAM Zaragoza meeting, pp. 1-7.

Ritter, A. (1892). Die Fortpflanzung der Wasserwellen. Zeitschrift des Vereines Deuscher Ingeniure, 36(33):947-954.

Sampson, J., Easton, A. & Singh, M. (2006), Moving boundary shallow water flow above parabolic bottom topography, Proceedings of the 7th biennial engineering mathematics and applications conference, EMAC-2005, volume 47 of ANZIAM Journal, pp C373-C387, Australian Mathematical Society.

Stoker, J. J. (1957). Water waves: the mathematical theory with applications, volume 4 of pure and applied mathematics, Interscience Publishers, New York, USA.

Thacker, W. C. (1981). Some exact solutions to the nonlinear shallow water wave equations, Journal of hydrology, 348 (1-2): 1-12.

Zhao, J., Özgen-Xia, I., Liang, D., Wang, T. & Hinkelmann, R. (2019). An improved multislope MUSCL scheme for solving shallow water equations on unstructured grids, Computers & Mathematics with Applications, Volume 77, Issue 2, p 576-596.